POLITECNICO
MILANO 1863

SCUOLA DI INGEGNERIA INDUSTRIALE
E DELL'INFORMAZIONE

A Multi-Fidelity approach to Deep Kernel Learning of dynamical systems from high-dimensional data sources

Tesi di Laurea Magistrale in
Mathematical Engineering - Statistical Learning

Author: **Federico Lancellotti**

Student ID: 10685832
Advisor: Prof. Andrea Manzoni
Co-advisors: Dr. Nicolò Botteghi
Academic Year: 2023-24

Abstract

In the framework of data-driven discovery of low dimensional dynamical systems, high-fidelity data can limit significantly the number of configurations considered and rapidly increase the computational cost. On the other hand, low-fidelity data is computationally less expensive and still useful to capture some qualitative features but fails to display the entirety of the details.

The present work proposes a generalization of the Stochastic Variational Deep Kernel Learning method, to consider multiple sources of not labeled high dimensional data, at different levels of fidelity, and learn in an unsupervised data-driven way a low dimensional dynamical system. This dimensionality reduction leverages on the estimation of the intrinsic dimension of the system, to recover a possible configuration of state variables for the problem.

The method is evaluated on a variety of cases, from the most simple motion of a pendulum to a more challenging PDE problem, all measured with high-dimensional RGB videos. In the pendulum environment, low-fidelity data can either be low-resolution images or partial reconstructions of the motion, while for the PDE problems we consider videos of numerical solutions on grids of different precision.

Results show that the method can effectively replace a considerable amount of high-fidelity data with the less expensive counterpart, while drastically improving the efficiency in terms of data volume and training time and maintaining a comparable level of accuracy.

Keywords: multi-fidelity, deep kernel learning, dynamical systems, low-dimensional systems, data-driven, PDE, reaction-diffusion, diffusion-advection, high-dimensional data, videos

Abstract in lingua italiana

Nell'ambito della scoperta data-driven di sistemi dinamici a bassa dimensionalità, i dati ad alta fedeltà possono limitare significativamente il numero di configurazioni considerate e aumentare rapidamente il costo computazionale. D'altra parte, i dati a bassa fedeltà sono meno costosi dal punto di vista computazionale e comunque utili a rappresentare alcune caratteristiche qualitative, ma non riescono a catturare l'intera complessità del sistema.

Questo lavoro propone una generalizzazione del metodo Stochastic Variational Deep Kernel Learning, per considerare più fonti di dati ad alta dimensionalità non etichettati, a diversi livelli di fedeltà, e apprendere tramite soli dati non etichettati un sistema dinamico a bassa dimensionalità. Questa riduzione della dimensionalità si appoggia sulla stima della dimensione intrinseca del sistema, per recuperare una possibile configurazione delle variabili di stato del problema.

Il metodo è valutato su una serie di casi, dal più semplice moto di un pendolo a più impegnativo problemi di EDP, tutti misurati con video RGB ad alta dimensionalità. Nel caso del pendolo, i dati a bassa fedeltà possono essere immagini a bassa risoluzione o ricostruzioni parziali del moto, mentre per i problemi PDE si considerano video di soluzioni numeriche su griglie di diversa finezza.

I risultati dimostrano che il metodo può sostituire efficacemente una notevole quantità di dati ad alta fedeltà con la controparte meno costosa, migliorando drasticamente l'efficienza in termini di volume di dati e di tempo di addestramento e mantenendo un livello di accuratezza comparabile.

Parole chiave: multi-fidelity, deep kernel learning, sistemi dinamici, sistemi a bassa dimensionalità, data-driven, EDP, reazione-diffusione, diffusione-trasporto, dati ad alta dimensionalità, video

Contents

Introduction

Data-driven discovery is at the heart of many modern methods we use to model, predict and control dynamical systems. Complex systems, such as in finance, robotics, climate, epidemiology, are not amenable to the traditional physical principles derivation, and researchers are turning to data-driven approaches for the most pressing scientific and engineering problems. The governing laws are often difficult to unveil, since these systems typically show nonlinear behaviours. On the other hand, high-dimensional measurements are able to capture the dominant underlying patterns that should be characterized and modeled for the eventual goal of sensing, prediction, estimation and control [5].

The recent achievements in Machine Learning and Deep Learning, combined with the availability of large amounts of data and computational resources, laid the foundations for new paradigms for the analysis and understanding of dynamical systems [4].

Though data are often high-dimensional, the behaviour exhibited by many of these complex systems can be effectively captured by a reduced number of latent state variables, that can describe their intrinsic low-dimensional nature. The process of mapping high-dimensional measurements into a low-dimensional latent space is often referred to as Model Order Reduction [38]. This task is traditionally tackled by the Singular Value Decomposition [5] and more recently approached via a specific type of neural network (NN) called Autoencoder (AE), which is able to learn a nonlinear map between the high-dimensional data space and a low-dimensional state space.

Examples in which this strategy is adopted include Gaussian process surrogate modelling [15], Dynamics Mode Decomposition [42][34], sparse identification of latent dynamics (SINDy) [6], manifold learning [25] in combination with SINDy for latent coordinate discovery [8], and in combination with NN-based surrogate models for latent representation learning towards control [46][3].

In particular, the construction of efficient surrogate models is crucial for producing model proxies which can cheaply and accurately characterise a partial differential equations system. Indeed, computational costs can easily become prohibitive when parameterised time-dependent systems of PDEs are solved with detailed full-order models in a multi-

query context [10], such as in uncertainty quantification [7], optimal control [30][44], and parameter estimation [12].

Reduced-order models (ROMs) have been developed to construct low-dimensional representations of high-dimensional systems for a significant reduction in computational costs with controlled accuracy [39][2]. Intrusive ROM techniques explicitly incorporate full-order governing equations at the reduced level and often yield reliable and physically meaningful solutions. On the other hand, non-intrusive approaches learn reduced-order systems primarily from solution data, including from numerical or experimental data, hence being more flexible, general and relevant [10].

However, the applicability and reliability of many numerical methods may collapse when the collection of high-fidelity (HF) data for model reduction is very time-consuming to produce or expensive to obtain. When time or budget restrictions prohibit the generation of additional data, the amount of available samples may be too limited to provide satisfactory model results. In addition, it is increasingly common to encounter scenarios where a wealth of data sources are readily available, easily accessible, and/or cheaply computable, albeit not perfectly accurate. For this reason, multi-fidelity (MF) methods are often employed to incorporate information from other sources, which are ideally well-correlated with the HF data, but can be obtained at a lower cost. By leveraging correlations between different datasets, MF methods often enable strong generalisation performance when compared to models based solely on a small amount of HF data [16].

Traditional MF regression schemes, also known as co-kriging [21][1], proved suitable for many different applications, including geostatistics [19], solving PDEs [40][20], uncertainty quantification, inference and optimitazion [33]. More recently, NNs based architectures were proposed to overcome some of the drawbacks related to the curse of dimensionality and consider nonlinear correlations between datasets of different fidelity levels [16], also in the case of time-dependent problems [10].

Moreover, most data-driven methods for modelling physical phenomena still rely on the assumption that the relevant state variables are already known. Despite the computing power at our disposal and the recent theoretical and technical novelties in artificial intelligence, the quest of identifying the hidden state variables has resisted automation and is still an open field of research [4][9].

Whether we aim to identify the hidden state variables or learn the entire system evolution from data, inferring complex dynamics from a variety of sources of information with different degrees of fidelity and accuracy is not effortless, as the identification, understanding and quantification of various uncertainties is often required. When data-driven meth-

ods consider stochasticity and uncertainties quantification, Variational Autoencoders [22] (VAEs) are often considered for learning low-dimensional states as probabilistic distributions. Samples from these distributions can be used for the construction of latent state models via Gaussian models [11].

With the present work, we introduce a MF generalisation of the framework proposed by Botteghi et al. in [4], namely a data-driven strategy for dimensionality reduction, latent-state model learning and uncertainty quantification, based on a variety of high-dimensional measurements of different degrees of accuracy, generated by unknown dynamical systems.

In particular, we introduce an ensemble of sub-models, each associated with a level of fidelity and composed of a Deep Kernel Learning (DKL) [47][32] encoder, which combines the highly expressive NN with a kernel-based probabilistic model of Gaussian process (GP) [41] to reduce the dimensionality and quantify the uncertainty simultaneously, followed by a DKL latent-state forward model that predicts the system dynamics with quantifiable modelling uncertainty, and an NN-based decoder designed to enable reconstruction. Each sub-model produces an estimate of how many state variables the observed system is likely to have, and latent representations of both the state and the dynamics of the system. The estimate of the intrinsic dimensionality is used to bound the latent state space dimension for the sub-models at higher levels of fidelity, while the low-fidelity latent representations are adopted as additional sources of information to correct the system dynamics learnt on a reduced volume of HF data.

The major advantage of the proposed method lies in its substantial generality, both in terms of the nature of the complex systems it can learn and the simplicity of the data sources it can adopt. Indeed, deep kernels display a better expressive power with respect to traditional Gaussian process regression (GPR) kernels, employing a remarkable scalability to high-dimensional inputs and nonlinear behaviours. To the best of our knowledge, this is the first attempt at considering the most ordinary of high-dimensional data sources, RGB videos, in a MF context, overcoming the need of the numerical solution, often not available in real applications. The proposed strategy is tested on a variety of cases, from the simple motion of a pendulum to a more challenging PDE problem. We believe that the hereby achieved results in efficiency, accuracy and generality are extremely relevant also in view of data-driven physical modeling of more complex dynamical systems.

In the following chapters, the details of the proposed framework are presented, along with the main numerical results. Chapter 1 collects the key prerequisites of our model, namely GPR, DKL and MF schemes, while the theoretical details of the architecture are

described in Chapter 2. The model performances are presented in Chapters 3 and 4, on data from low-dimensional dynamical systems and PDE discretisation, respectively. In particular, the method is tested on its ability to reconstruct the frame, to predict the system dynamics one-step forward in time and to extrapolate in time. Finally, in Chapter 5 we summarise the achieved results, highlighting both strengths and issues of the proposed framework, concluding with possible future expansions of our work.

1 | Preliminaries

Consider a number of high-dimensional measurements of a dynamical system of the form $\dot{\mathbf{s}} = \mathcal{F}(\mathbf{s})$, where $\mathbf{s}$ is the state vector and it is a function of time. The data is obtained from a variety of sources, not necessarily exhibiting the same degree of fidelity to the real system. Our goal is (i) to learn a meaningful representation of the unknown states and a surrogate model for $\mathcal{F}$, overcoming both the high-dimensional nature of the available measurements and the nonlinearities displayed by the system, and (ii) to leverage not only the high fidelity data, but also the less accurate sources. To achieve such goal, in Chapter 2 we propose a comprehensive framework, that is built on a number of components.

In the following, we introduce GPR [41], also known as *kriging*, a non-parametric regression technique that models the prior knowledge about a computational model with a GP [27], and that we use for data-driven surrogate modeling and uncertainty quantification (UQ). To deal with high-dimensional data, we additionally introduce DKL [47], that combines the nonlinear representational power of NNs with the reliable uncertainty estimates of GPs [27]. In particular, DKL will be employed in the architecture of both the AE and the dynamical model discussed in Chapter 2, that compose the main building blocks of our framework. Then, we present the major intuitions and ideas behind MF methods, with the aim at leveraging the correlation between data sources of different fidelities, i.e. the inputs of our model. Finally, we discuss the Levina-Bickel algorithm to estimate the intrinsic dimension of a dynamical system, that we will use as hyperparameter of our model.

1.1. Gaussian Process Regression

A GP is a collection of random variables, any finite number of which have a joint Gaussian distribution [41]. A GP is completely specified by its mean function and covariance function. Let $\mathbf{x} \in \mathbb{R}^n$, we define the mean function $m(\mathbf{x})$ and the covariance/kernel

function $k(\mathbf{x}, \mathbf{x}')$ of a real process $Z(\mathbf{x})$ as

$$\begin{aligned} m(\mathbf{x}) &= E[Z(\mathbf{x})]\,, \\ k(\mathbf{x}, \mathbf{x}') &= \mathbb{E}[(Z(\mathbf{x}) - m(\mathbf{x}))(Z(\mathbf{x}') - m(\mathbf{x}'))]\,, \end{aligned} \tag{1.1}$$

and we will write the GP as

$$Z(\mathbf{x}) \sim \mathcal{GP}(m(\mathbf{x}), k(\mathbf{x}, \mathbf{x}'))\,. \tag{1.2}$$

In regression, we consider the training data inputs $\mathcal{X} = (\mathbf{x}^{(1)}, \mathbf{x}^{(2)}, ..., \mathbf{x}^{(N)}), \mathbf{x}^{(i)} \in \mathbb{R}^n$, and the corresponding training targets $\mathcal{Y} = (G(\mathbf{x}^{(1)}), G(\mathbf{x}^{(2)}), ..., G(\mathbf{x}^{(N)}))$. Assume that the prior knowledge of a computational model $G(\mathbf{x})$ can be modelled by a GP $Z(\mathbf{x}) \sim \mathcal{GP}(m, k)$, then any collection of function values $\mathbf{Z} = Z(\mathcal{X})$ has a joint Gaussian distribution

$$\mathbf{Z} = Z(\mathcal{X}) = [Z(\mathbf{x}_1), ..., Z(\mathbf{x}_n)]^\top \sim \mathcal{N}(\boldsymbol{\mu}, K_{\mathcal{X},\mathcal{X}})\,, \tag{1.3}$$

with mean vector $\boldsymbol{\mu}_i = m(\mathbf{x}_i)$ and covariance matrix $(K_{\mathcal{X},\mathcal{X}})_{i,j} = k(\mathbf{x}_i, \mathbf{x}_j)$, determined from the mean function and covariance kernel of the GP. We can parametrise the kernel function as

$$k(\mathbf{x}, \mathbf{x}') = \sigma_k^2 r(\mathbf{x}, \mathbf{x}'; \boldsymbol{\theta}) \tag{1.4}$$

where σ_k^2 and $\boldsymbol{\theta}$ have to be estimated [27], as we will see later.

To build up a GP model, the class of the correlation kernel $r(\mathbf{x}, \mathbf{x}'; \boldsymbol{\theta})$ needs to be set. In this regard, a popular choice of the kernel function is the automatic relevance determination (ARD) squared exponential (SE) kernel:

$$k(\mathbf{x}, \mathbf{x}') = \sigma_k^2 \exp\left(-\frac{1}{2}\sum_{j-1}^{d} \frac{(x_j - x_j')^2}{l_j^2}\right) \tag{1.5}$$

where $\{l_j\}_{(1 \le j \le d)}$ are the length-scales along each individual input direction.

Assuming additive Gaussian noise $G(\mathbf{x})|Z(\mathbf{x}) \sim \mathcal{N}(0, \sigma_\epsilon^2)$, the predictive distribution of the GP evaluated at N^* test data points $\mathcal{X}^*$ is

$$[Z(\mathcal{X}^*)|Z(\mathcal{X}) = \mathcal{Y}, \sigma^2, \boldsymbol{\theta}] \sim \mathcal{N}(\mathbb{E}[Z(\mathcal{X}^*)], C(Z(\mathcal{X}^*))) \tag{1.6}$$

where

$$\begin{aligned} \mu^* &= \boldsymbol{\mu}_{\mathcal{X}^*} + K_{\mathcal{X}^*,\mathcal{X}}(K_{\mathcal{X},\mathcal{X}} + \sigma I)^{-1}\mathcal{Y} \\ C(Z(\mathcal{X}^*)) &= K_{\mathcal{X}^*,\mathcal{X}^*} + K_{\mathcal{X}^*,\mathcal{X}}(K_{\mathcal{X},\mathcal{X}} + \sigma I)^{-1}K_{\mathcal{X},\mathcal{X}^*} \end{aligned} \tag{1.7}$$

$K_{\mathcal{X}^*,\mathcal{X}}$ is an $N^* \times N$ matrix of covariances between the GP evaluated at $\mathcal{X}^*$ and $\mathcal{X}$. $\boldsymbol{\mu}_{\mathcal{X}^*}$ is the $N^* \times 1$ mean vector, and $K_{\mathcal{X},\mathcal{X}}$ is the $N \times N$ covariance matrix evaluated at training inputs $\mathcal{X}$. All covariance matrices implicitly depend on the kernel hyperparameters $\boldsymbol{\theta}$ [47].

By maximising the marginal likelihood given the training targets $\mathcal{Y}$, namely the probability of observing the data conditioned only on the kernel hyperparameters, the optimal values of $(\boldsymbol{\theta}, \sigma_\epsilon)$ can be estimated in the following way:

$$\begin{aligned} (\hat{\boldsymbol{\theta}}, \hat{\sigma_\epsilon}) &= \arg\max_{\boldsymbol{\theta},\sigma_\epsilon} \log p(\mathcal{Y}|\mathcal{X};\boldsymbol{\theta}) = \\ &= \arg\max_{\boldsymbol{\theta},\sigma_\epsilon} \Big\{ -\mathcal{Y}^\top (K_{\mathcal{X},\mathcal{X}|\boldsymbol{\theta}} + \sigma_\epsilon^2 I)^{-1}\mathcal{Y} - \log|K_{\mathcal{X},\mathcal{X}|\boldsymbol{\theta}} + \sigma_\epsilon^2 I| \Big\} \end{aligned} \tag{1.8}$$

Optimising the GP hyperparameters σ and $\boldsymbol{\theta}$ requires to solve the linear system $(K_{\mathcal{X},\mathcal{X}} + \sigma_\epsilon^2 I)^{-1}\mathcal{Y}$ and computing the log determinant $\log|K_{\mathcal{X},\mathcal{X}|\boldsymbol{\theta}} + \sigma_\epsilon^2 I|$, which can be very expensive in the cases of high-dimensional inputs (e.g., images with thousands of pixels) or big datasets ($M \gg 1$) [4]. In this context, the standard approach is to compute the Cholesky decomposition of the $N \times N$ matrix $K_{\mathcal{X},\mathcal{X}}$, which requires $\mathcal{O}(N^3)$ operations and $\mathcal{O}(N^2)$ storage [47]. In the next section, we present an alternative solution, that improves the expressive power of traditional kernels by leveraging on neural networks to learn deep kernels.

1.2. Deep Kernel Learning

To mitigate the limited scalability of traditional GPs to high-dimensional inputs, often referred to as the curse of dimensionality, Deep Kernel Learning [47] (DKL) was developed. By exploiting the nonlinear expressive power of deep NNs, DKL is capable to learn compact data representations, while maintaining the probabilistic features of kernel-based GP models for UQ [4].

Starting from a base kernel $k(\mathbf{x}, \mathbf{x}'; \boldsymbol{\theta})$ with hyperparameters $\boldsymbol{\theta}$, we embed a deep NN, which represents a nonlinear mapping from the input $\mathbf{x}$ to the feature space, into the kernel function:

$$k(\mathbf{x}, \mathbf{x}'; \boldsymbol{\theta}) \to k(g(\mathbf{x}, \mathbf{w}), g(\mathbf{x}', \mathbf{w}); \boldsymbol{\theta}, \mathbf{w}) \ , \tag{1.9}$$

where $g(\mathbf{x}, \mathbf{w})$ is a non-linear mapping given by a deep architecture, such as a deep convolutional network, parametrised by weights $\mathbf{w}$. Unlike traditional kernels used in

GPR, the deep kernel encapsulates a better expressive power, since the deep learning transformation $g(\mathbf{x}, \mathbf{w})$ is capable of capturing non-stationary and hierarchical structures [47]. As for traditional GPs, different kernel functions can be chosen and both the GP hyperparameters and the NN parameters are jointly trained by maximising a marginal likelihood. Therefore, DKL still suffers from computational inefficiencies, disqualifying the method for very large ($M \gg 1$) datasets [4]. Additionally, stochastic gradient descent or other stochastic training strategies are not available for DKL models [13] if we choose non-Gaussian likelihoods, which cause the posterior to be intractable.

To overcome these limitations, Stochastic Variational Deep Kernel Learning [48] (SVDKL) was introduced. SVDKL utilises variational inference [41] to approximate the posterior distribution with the best fitting Gaussian to a set of inducing data points sampled from the posterior. Similar to the framework proposed by Botteghi et al. in [4], our model is built upon SVDKL for the same main reasons: kernel-based models as GPs offer better quantification of uncertainty [41] with respect to deterministic NNs, and it is computationally cheaper than Bayesian NNs when a deep NN architecture is integrated [23].

1.3. Multi-fidelity methods

So far, we have seen the advantages of GPR in terms of uncertainty quantification and data-driven surrogate modeling, and how to mitigate its main drawback by exploiting the remarkable expressive power of NNs with deep kernels. We now want to be able to consider a variety of data sources, which display different accuracy with respect to the true dynamical system, and exploit their correlation.

GPR with training data from different fidelity levels is known as co-kriging [21]. The core idea is to leverage a large amount of LF data during training, in a setting in which a limited number of HF samples are available. Since LF evaluations are cheap, either in terms of time or computational effort, the cost of training data preparation can be reduced by controlling the number of HF evaluation [16], which are often collected from detailed simulations or accurate sensors, hence more expensive to obtain.

Assuming a linear correlation between the different fidelity levels, we can employ the Linear Model for Coregionalisation [1] (LMC), that expresses the prior of a hierarchy of L fidelities as

$$Z_l(\mathbf{x}) = \sum_{i=0}^{L-1} a_{l,i} u_i(\mathbf{x}) \,, \quad l = 0, 1, ..., L-1, \tag{1.10}$$

namely, each level of solution $Z_l(\mathbf{x})$ can be written as a linear combination of L indepen-

dent GPs $u_i \sim \mathcal{GP}(0, k_i(\cdot,\cdot))$. The vector $\mathbf{a}_i = (a_{0,i}, ..., a_{L-1,i})^\top$, $0 \leq i \leq L-1$, collects the weights of the corresponding GP component u_i and the matrix-valued kernel of the MF GPR model assumes the form

$$K(\mathbf{x}, \mathbf{x}') = \sum_{i=0}^{L-1} \mathbf{a}_i \mathbf{a}_i^\top k_i(\mathbf{x}, \mathbf{x}') \,. \tag{1.11}$$

In the two-level case, by considering the special form $\mathbf{a}_0 = (1, 0)^\top$, $\mathbf{a}_1 = (\rho, 1)^\top$, we can retrieve the well-known autoregressive model AR(1)-cokriging [21] defining the prior of a LF solution Z_0 and a HF Z_1:

$$Z_0(\mathbf{x}) = u_0(\mathbf{x}) \,, \tag{1.12}$$

$$Z_1(\mathbf{x}) = \rho u_0(\mathbf{x}) + u_1(\mathbf{x}) \,. \tag{1.13}$$

Notice that LMC allows for much more general linear combinations, if the situation suggests a less strict hierarchical structure among the levels of fidelity. For instance, if we have two different LF sources of data that exhibit a comparable accuracy, and a single HF source, we can consider the following configuration:

$$Z_0(\mathbf{x}) = u_0(\mathbf{x}) \,, \tag{1.14}$$

$$Z_1(\mathbf{x}) = u_1(\mathbf{x}) \,, \tag{1.15}$$

$$Z_2(\mathbf{x}) = \rho_0 u_0(\mathbf{x}) + \rho_1 u_1(\mathbf{x}) + u_2(\mathbf{x}) \,. \tag{1.16}$$

in which $\mathbf{a}_0 = (1, 0, 0)^\top$, $\mathbf{a}_1 = (0, 1, 0)^\top$, $\mathbf{a}_2 = (\rho_0, \rho_1, 1)^\top$. In this case, the models Z_0 and Z_1, associated with the two LF levels, are independent, while the HF model Z_2 leverages on all the three GP components. We will exploit this notion later, to evaluate our strategy on a more general hierarchical configuration of data sources.

1.4. Levina-Bickel algorithm

As we will see later, our framework involves dimensionality reduction, performed by a specific type of NN called AE [13]. AEs are able to learn a nonlinear map between the high-dimensional data space and a low-dimensional state space, through a NN called encoder, and an inverse mapping through a decoder. Instead of fixing the latent state space hyperparameter, we prefer to automatically learn it by estimating the true system state space dimension via the Levina-Bickel algorithm [26]. In the following, we will refer to such estimate as the Intrinsic Dimensionality (ID).

The Levina-Bickel algorithm for ID estimation provides a maximum likelihood estimator (MLE) of the dimension ID from i.i.d. observations $\mathbf{z}_1, ..., \mathbf{z}_n$ in $\mathbb{R}^p$, where, in our framework, $\mathbf{z}_1, ..., \mathbf{z}_n$ are the latent vectors collected from the trained AE model.

The observations (latent vectors) represent an embedding of a lower-dimensional sample, i.e. $\mathbf{z}_i = g(\mathbf{s}_i)$, where $\mathbf{s}_i$ are sampled from an unknown smooth density f on $\mathbb{R}^{ID}$, with unknown $ID \leq p$, and g is a continuous and sufficiently smooth (but not necessarily globally smooth) mapping.

The key idea is to fix a point $\mathbf{z}$, assume $f(\mathbf{z}) \approx const$ in a small sphere $S_{\mathbf{z}}(R)$ of radius R around $\mathbf{z}$, and treat the observations as a homogeneous Poisson process in $S_{\mathbf{z}}(R)$. On the basis of this observation, the Levina–Bickel algorithm derives the local ID estimator near $\mathbf{z}$ as

$$ID_{L-B}(\mathbf{z}) = \frac{1}{k-2} \sum_{j=1}^{k-1} \log \frac{T_k(\mathbf{z})}{T_j(\mathbf{z})}, \tag{1.17}$$

where we are fixing the number of neighbors k rather than the radius of the sphere R, and $T_k(\mathbf{z})$ is the Euclidean distance between $\mathbf{z}$ and the its k-th nearest neighbor in $\mathbf{z}_1, ..., \mathbf{z}_n$.

The actual derivation from the likelihood equations divides by $k-1$, rather than $k-2$. However, we prefer this correction to the formulation, since it makes the estimator asymptotically unbiased [26].

For some applications, one may want to evaluate local dimension estimates at every data point, or average estimated dimensions within data clusters. However, we assume that all the data points come from the same "manifold", and therefore average over all observations.

The choice of k clearly affects the estimate and, in general, the sphere should be small and contain sufficiently many points, for the estimator to work well. We could, for instance, average over a range of values k, or implement more elaborate solutions to choose k automatically. In this work, we decide to simply fix $k = 20$.

Finally, the global ID estimator is calculated as

$$ID_{L-B} = \frac{1}{N} \sum_{i=1}^{N} \frac{1}{k-2} \sum_{j=1}^{k-1} \log \frac{T_k(\mathbf{z}_i)}{T_j(\mathbf{z}_i)}. \tag{1.18}$$

In the next chapter, we introduce a model that conjugates the concepts introduced so far, namely the availability of a variety of data sources in a MF fashion, with the flexibility and expressive power of SVDKL methods, to fully exploit high-dimensional measurements of nonlinear dynamical systems. We will later test it on a variety of cases, on its ability

to leverage multiple data sources in the task of learning the dynamics of an unknown dynamical system.

2 | Methods

Consider the following nonlinear dynamical system:

$$\frac{d}{dt}\mathbf{s}(t) = \mathcal{F}(\mathbf{s}(t)), \quad \mathbf{s}(t_0) = \mathbf{s}_0, \quad t \in [t_0, t_f], \tag{2.1}$$

where $\mathbf{s}(t) \in \mathcal{S} \subset \mathbb{R}^d$ is the state vector at time t, $\mathcal{F} : \mathcal{S} \to \mathcal{S}$ is a nonlinear function determining the evolution of the system given the current state $\mathbf{s}(t)$, $\mathbf{s}_0$ is the initial condition and t_0 and t_f are the initial and final time, respectively. While the state $\mathbf{s}(t)$ is not directly accessible in general and the function $\mathcal{F}$ is usually unknown, we can obtain information about the system indirectly through measurements from different sensor devices. Assuming a discretisation in time of the measurements, we indicate with $\mathbf{x}_l^{(t)}$ the measurement vector of fidelity level l, at the time-step t, and $\mathbf{x}_l^{(t+1)}$ the measurement (of the same fidelity level l) at time $t+1$.

Given L sets of N_l d_l-dimensional measurements $\mathbf{X}_l = (\mathbf{x}_l^1, ..., \mathbf{x}_l^{N_l}) \in \mathcal{X}_l \subset \mathbb{R}^{d_l} \times \cdots \times \mathbb{R}^{d_l}$, with $d_l \gg 1$ and l being the fidelity level, $0 \leq l \leq L$, we consider the problem of identifying a meaningful representation of the hidden states and a surrogate model for $\mathcal{F}$, exploiting not only data from detailed HF simulations, but also partial or less accurate measurements, in a MF fashion.

In practice, we will build L surrogate (sub-)models Z_l, each one trained on a specific set of measurements $\mathbf{X}_l$ and leveraging the knowledge on the system acquired by the previous less accurate models Z_i, $i < l$.

Each sub-model is composed of two components: a SVDKL AE, that maps each high-dimensional measurement to a distribution over the latent state space, and a SVDKL dynamical model, that learns the dynamics of the system using the latent state variables. The learnt latent representations of both the state and the dynamics are then used as inputs for the subsequent submodels, to bound the dimensionality of the latent space and correct its learning process.

Figure 2.1 shows a scheme of the model, considering two levels of fidelity, for ease of reading.

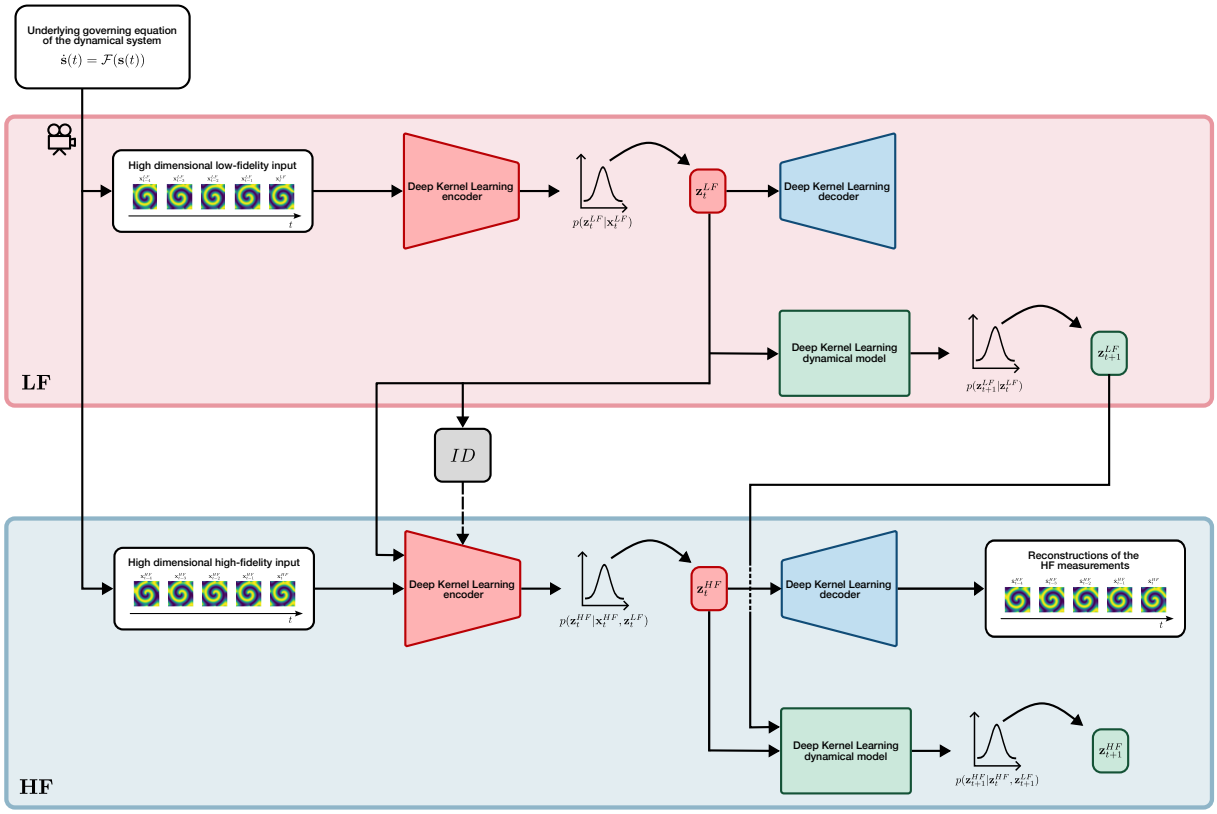

Figure 2.1: The model is composed of two main parts, receiving LF and HF inputs, respectively. Each part includes an AE and a dynamical model. The outputs of the LF sub-model, are used by the HF sub-model and to estimate ID.

The model architecture is described in detail in the following sections, considering an arbitrary number of levels. In particular, Section 2.1 introduces the SVDKL AE, to map the high-dimensional measurements into a low-dimensional space; Section 2.2 describes the SVDKL dynamical model, that learns the dynamics of the system. The loss function used during the training phase is presented in Sections 2.3 and 2.3.1, while a strategy for the estimation of the intrinsic dimensionality of the system is proposed in Section 2.4. Finally, a generalisation beyond the strict chain hierarchy of data sources is introduced in Section 2.5.

2.1. Learning the hidden state

We introduce a SVDKL encoder $E_l : \mathcal{X}_l \to \mathcal{L}_l$ that maps the high-dimensional measurements into distributions over a low-dimensional latent space $\mathcal{L}_l$, where l indicates the fidelity level. A latent state sample can be obtained as:

$$z_{i,l}^{(t)} = Z_i^{E_l}(\mathbf{x}_l^{(t)}) + \varepsilon_{E_l}\,, \quad \varepsilon_{E_l} \sim \mathcal{N}(0, \sigma_{E_l}^2)\,, \tag{2.2}$$

$$Z_i^{E_l}(\mathbf{x}_l^{(t)}) \sim \mathcal{GP}(\mu(g_{E_l}(\mathbf{x}_l^{(t)}; \mathbf{w}_{E_l})), k(g_{E_l}(\mathbf{x}_l^{(t)}; \mathbf{w}_{E_l}), g_{E_l}(\mathbf{x}_l^{(t')}; \mathbf{w}_{E_l}); \boldsymbol{\theta}_{E_l,i}))\,, \quad 1 \leq i \leq |\mathbf{z}_l| \tag{2.3}$$

where $z_{i,l}^{(t)}$ is the sample from the i^{th} GP with kernel k and mean μ, $g_{E_l}(\mathbf{x}_l^{(t)}; \mathbf{w}^{E_l})$ is the feature vector output of the NN part of the SVDKL encoder E_l, ε_{E_l} is an independently added noise and $|\mathbf{z}_l|$ indicates the dimension of $\mathbf{z}_l$ [4].

Since we have no access to the actual state values, the parameters $(\mathbf{w}_{E_l}, \boldsymbol{\theta}_{E_l}, \sigma_{E_l}^2)$ are optimised with a decoder $D_l : \mathcal{L}_l \times \mathcal{L}_{l-1} \to \mathcal{X}_l$ that reconstructs the measurements given the latent state samples corrected with the latent state representation at the previous fidelity level, namely the input of the decoder D_l is

$$\tilde{\mathbf{z}}_l = \mathbf{z}_l + \rho \mathbf{z}_{l-1}\,. \tag{2.4}$$

The reconstructions $\hat{\mathbf{x}}_l$ are also used to generate gradients for the encoder E_l. While the SVDKL encoder E_l learns $p(\mathbf{z}_l^{(t)}|\mathbf{x}_l^{(t)})$, the decoder D_l learns the inverse mapping $p(\hat{\mathbf{x}}_l^{(t)}|\tilde{\mathbf{z}}_l^{(t)})$ in which $\hat{\mathbf{x}}_l^{(t)}$ is the reconstruction of $\mathbf{x}_l^{(t)}$.

We can define the loss function as

$$\text{loss}_{E_l}(\mathbf{w}_{E_l}, \boldsymbol{\theta}_{E_l}, \sigma_{E_l}^2, \boldsymbol{\theta}_{D_l}) = \mathbb{E}_{\mathbf{x}_l^{(t)} \sim \mathbf{X}_l}[-\log p(\hat{\mathbf{x}}_l^{(t)}|\tilde{\mathbf{z}}_l^{(t)})]\,, \tag{2.5}$$

where $\hat{\mathbf{x}}_l^{(t)}|\tilde{\mathbf{z}}_l^{(t)} \sim \mathcal{N}(\mu_{\hat{\mathbf{x}}_l^{(t)}}, \Sigma_{\hat{\mathbf{x}}_l^{(t)}})$. By minimising the loss function with respect to the encoder and decoder parameters, we can obtain a compact representation of the measurements. While $|\mathbf{z}_0|$ is an hyperparameter to set, for the subsequent sub-models the dimension of the latent space is automatically obtained by estimating the intrinsic dimension of the system from the latent state representation of the previous level of fidelity, as we will discuss more in detail later.

2.2. Learning the latent dynamics

The second component of each sub-model is a surrogate model $F_l : \mathcal{L}_l \times \mathcal{L}_{l-1} \to \mathcal{L}_l$, still based on a SVDKL architecture, that aims to learn and predict the system evolution given the latent state variables sampled from $\mathcal{L}_l$ and the next latent state $\mathbf{z}_{l-1}^{(t+1)}$ sampled from $\mathcal{L}_{l-1}$, where l is the current fidelity level. The next latent states, at fidelity level l, $\mathbf{z}_l^{(t+1)}$ can be sampled with F_l:

$$z_{i,l}^{(t+1)} = Z_i^{F_l}(\mathbf{z}_l^{(t)}, \mathbf{z}_{l-1}^{(t+1)}) + \varepsilon_{F_l}\,, \quad \varepsilon_{F_l} \sim \mathcal{N}(0, \sigma_{F_l}^2)\,, \tag{2.6}$$

$$\begin{aligned} &Z_i^{F_l}(\mathbf{z}_l^{(t)}, \mathbf{z}_{l-1}^{(t+1)}) \sim \\ &\quad \mathcal{GP}(\mu(g_{F_l}(\mathbf{z}_l^{(t)}, \mathbf{z}_{l-1}^{(t+1)}; \mathbf{w}_{F_l})), k(g_{F_l}(\mathbf{z}_l^{(t)}, \mathbf{z}_{l-1}^{(t+1)}; \mathbf{w}_{F_l}), g_{F_l}(\mathbf{z}_l^{(t')}, \mathbf{z}_{l-1}^{(t'+1)}; \mathbf{w}_{F_l}); \boldsymbol{\theta}_{F_l,i}))\,, \\ &\qquad\qquad 1 \le i \le |\mathbf{z}_l| \end{aligned} \tag{2.7}$$

where $z_{i,l}^{(t+1)}$ is sampled from the i^{th} GP, $g_{F_l}(\mathbf{z}_l^{(t)}, \mathbf{z}_{l-1}^{(t+1)}; \mathbf{w}^{F_l})$ is the feature vector output of the NN part of the SVDKL dynamical model F_l, ε_{F_l} is an independently added noise and $|\mathbf{z}_l|$ indicates the dimension of $\mathbf{z}_l$.

Due to the unsupervised nature of our strategy, since we only have access to the sequence of measurements at different time-steps, the learning process of the dynamics employs the encoding of the measurement $\mathbf{x}_l^{(t+1)}$ through the SVDKL encoder E_l to the distribution $p(\mathbf{z}_l^{(t+1)}|\mathbf{x}_l^{(t+1)})$, and uses such a distribution as target for $p(\mathbf{z}_l^{(t+1)}|\mathbf{z}_l^{(t)}, \mathbf{z}_{l-1}^{(t+1)})$ produced by the dynamical model F_l. In particular, F_l is trained by minimising the Kullback-Leibler divergence between the distributions $p(\mathbf{z}_l^{(t+1)}|\mathbf{x}_l^{(t+1)})$ and $p(\mathbf{z}_l^{(t+1)}|\mathbf{z}_l^{(t)}, \mathbf{z}_{l-1}^{(t+1)})$. The loss is given by:

$$\text{loss}_{F_l}(\mathbf{w}_{F_l}, \boldsymbol{\theta}_{F_l}, \sigma_{F_l}^2) = \mathbb{E}_{\mathbf{x}_l^{(t)}, \mathbf{x}_l^{(t+1)} \sim \mathbf{X}_l}[\text{KL}[p(\mathbf{z}_l^{(t+1)}|\mathbf{x}_l^{(t+1)})||\; p(\mathbf{z}_l^{(t+1)}|\mathbf{z}_l^{(t)}, \mathbf{z}_{l-1}^{(t+1)}]]\,, \tag{2.8}$$

where $p(\mathbf{z}_l^{(t+1)}|\mathbf{z}_l^{(t)}, \mathbf{z}_{l-1}^{(t+1)})$ is obtained by feeding a sample from $p(\mathbf{z}_l^{(t)}|\mathbf{x}_l^{(t)})$ and from

$p(\mathbf{z}_{l-1}^{(t+1)}|\mathbf{z}_{l-1}^{(t)}, \mathbf{z}_{l-2}^{(t+1)})$ to F_l.

We also reintroduce the same loss function encountered in the SVDKL AE, by passing to the decoder D_l the latent state prediction $\mathbf{z}_l^{(t+1)}$, obtained from F_l, and minimising the error between the respective reconstruction $\hat{\mathbf{x}}_l^{(t+1)}$ and the one obtained from the SVDKL AE applied to $\mathbf{x}_l^{(t+1)}$:

$$\tilde{\text{loss}}_{F_l}(\mathbf{w}_{F_l}, \boldsymbol{\theta}_{F_l}, \sigma_{F_l}^2) = \mathbb{E}_{\mathbf{x}_l^{(t+1)} \sim \mathbf{X}_l}[-\log p(\hat{\mathbf{x}}_l^{(t+1)}|\mathbf{z}_l^{(t+1)}, \mathbf{z}_{l-1}^{(t+1)})]\,. \tag{2.9}$$

2.3. Training of the models

The two components E_l and F_l are jointly trained, allowing the gradients of the dynamical model F_l to flow through the encoder E_l as well. The overall loss function is given by:

$$\begin{aligned}&\text{loss}_l(\mathbf{w}_{E_l}, \boldsymbol{\theta}_{E_l}, \sigma_{E_l}^2, \boldsymbol{\theta}_{D_l}, \mathbf{w}_{F_l}, \boldsymbol{\theta}_{F_l}, \sigma_{F_l}^2) = \\ &\mathbb{E}_{\mathbf{x}_l^{(t)}, \mathbf{x}_l^{(t+1)} \sim \mathbf{X}_l}[-\log p(\hat{\mathbf{x}}_l^{(t)}|\mathbf{z}_l^{(t)}, \mathbf{z}_{l-1}^{(t)}) + \beta \text{KL}[p(\mathbf{z}_l^{(t+1)}|\mathbf{x}_l^{(t+1)})||p(\mathbf{z}_l^{(t+1)}|\mathbf{z}_l^{(t)}, \mathbf{z}_{l-1}^{(t+1)}]+ \\ &\qquad - \log p(\hat{\mathbf{x}}_l^{(t+1)}|\mathbf{z}_l^{(t+1)}, \mathbf{z}_{l-1}^{(t+1)})]\,,\end{aligned} \tag{2.10}$$

in which β is used to scale the contribution of the two loss terms.

Once the sub-model at fidelity level l is trained, it is evaluated on a portion of the training data $\mathbf{X}_l$ available also at level of fidelity $l+1$. The learnt latent representations of both the hidden state and the dynamics are used as additional inputs during the training of the sub-model $l+1$. In the particular case of the sub-model at level $l = 0$, null vectors are used as additional inputs, since no information has been learnt so far. The last sub-model $L-1$ is trained on the (few) measurements of highest accuracy, leveraging all the LF data.

2.3.1. Variational inference

Since the two SVDKL components exploit variational inference to approximate the aforementioned posterior distributions, we add two extra terms to the loss function, one for each SVDKL component, of the form

$$\text{loss}_{var}(\mathbf{w}, \boldsymbol{\theta}) = \text{KL}[p(\mathbf{v})||q(\mathbf{v})]\,, \tag{2.11}$$

where $p(\mathbf{v})$ is the posterior to be approximated over the inducing points $\mathbf{v}$, and $q(\mathbf{v})$ represents an approximating candidate distribution. The inducing points $\mathbf{v}$ are placed on

a grid, following the intuition in the original SVDKL work [48].

2.4. Intrinsic dimension of the system

In order to produce a meaningful representation of the hidden state variables of the system, we would want to retrieve a number of latent variables as close as possible to the dimension of the actual state space. Similarly to the work by Chen at al. [9], we employ the Levina-Bickel algorithm [26] to estimate the ID of the system.

The Levina-Bickel algorithm is applied to the latent representations of the states $\mathbf{z}_l^t$ and $\mathbf{z}_l^{t+1}$ obtained from the SVDKL AE and the latent forward dynamics learnt by the SVDKL dynamical model. Finally, a rounded average of the three estimates is considered as ID estimate at fidelity level l.

When constructing the sub-model at level $l+1$, the ID estimate at level l is employed as dimension of the latent space $|\mathbf{z}|$, restricting the new latent space to the desired dimension.

2.5. Beyond the chain hierarchy

So far, we have assumed a strict chain hierarchy among the levels of fidelity: the measurements $\mathbf{X}_l$ at level l are supposedly less accurate than the measurements $\mathbf{X}_{l+1}$. While this is convenient in some cases, in most of practical applications it often happens that different sensors produce similarly accurate but partial measurements, imposing a less rigid configuration of the sub-models.

To address these cases we can leverage on the generality of the LMC described in Chapter 1. If two different LF sensors exhibit a comparable degree of accuracy, we can separately train their respective models, Z_0 and Z_1, in the classical single-fidelity fashion. Then, we consider a linear combination of their respective latent state representations, $\mathbf{z} = \rho_0\mathbf{z}_0 + \rho_1\mathbf{z}_1$, as additional LF input for the HF model Z_2.

Following this simple intuition, we can easily generalise our framework and exploit much more complex hierarchical fidelity structures of measurements.

We conclude this chapter presenting Algorithm 2.1, that summarises the main steps of the model, considering two levels of fidelity. We use the notation $\mathbf{z}$ and $\mathbf{z}^{next}$ to indicate the latent representations obtained from the SVDKL AE applied on the measurements at times t and $t+1$, respectively; $\mathbf{z}^{fwd}$ indicates the latent representation obtained from the SVDKL dynamical model.

The algorithm can be easily generalised, with a slightly heavier notation, to the case of an arbitrary number of levels, not necessarily in a strict chain hierarchy.

Algorithm 2.1 Multi-Fidelity DKL Algorithm

for level = LF, HF **do**
  if level == LF **then**
    Initialise $\mathbf{z}_{LF}, \mathbf{z}_{LF}^{next}, \mathbf{z}_{LF}^{fwd} = \mathbf{0}$;
    Set latentDimension to an arbitrary value;
  else
    Initialise $\mathbf{z}_{LF} = \mathbf{z}$, $\mathbf{z}_{LF}^{next} = \mathbf{z}^{next}$, $\mathbf{z}_{LF}^{fwd} = \mathbf{z}^{fwd}$;
    Set latentDimension = ID;
  end if

  for epoch = 1, 2, ... **do**
    Encode $\mathbf{x} \rightarrow \mathbf{z}$, $\mathbf{x}^{next} \rightarrow \mathbf{z}^{next}$;
    Decode $\hat{\mathbf{x}} \leftarrow \mathbf{z} + \rho\mathbf{z}_{LF}$, $\hat{\mathbf{x}}^{next} \leftarrow \mathbf{z}^{next} + \rho\mathbf{z}_{LF}^{next}$;
    Estimate $\mathbf{z} + \rho\mathbf{z}_{LF}^{fwd} \rightarrow \mathbf{z}^{fwd}$;
    Decode $\hat{\mathbf{x}}^{fwd} \leftarrow \mathbf{z}^{fwd}$;
    Compute the $loss(\mathbf{x}, \hat{\mathbf{x}}, \hat{\mathbf{x}}^{next}, \hat{\mathbf{x}}^{fwd}, \mathbf{z}^{next}, \mathbf{z}^{fwd})$;
    Backward propagate the gradients;
  end for

  if level == LF **then**
    Compute ID = $\lceil \frac{1}{3}LB(\mathbf{z}) + \frac{1}{3}LB(\mathbf{z}^{next})) + \frac{1}{3}LB(\mathbf{z}^{fwd}))\rceil$;
  end if
end for

3 | Low-dimensional dynamical systems

In this chapter we evaluate the performance of our model on measurements from low-dimensional dynamical systems, assessing, in particular, the test cases of the simple pendulum and the acrobot. As input data we consider high-dimensional RGB images obtained through RGB cameras of different quality of resolution, with the system evolution simulated by the Gymnasium Python library [17].

After a brief presentation of the theoretical details of the problem and the model configuration, we discuss the Levina-Bickel estimate of the dynamical system ID, along with the behaviour of its hidden state variables.

The model is specifically tested for its ability to accurately reconstruct the input frame and predict the dynamics one-step forward in time, for a variety of configurations of initial conditions unseen during the training phase. Additionally, we show the model performances in extrapolating the dynamics in time.

3.1. Simple pendulum

To demonstrate the predictive capabilities of our framework, the first test-case we consider is the simple pendulum described by the following equation:

$$\ddot{\phi}(t) = -\frac{g}{l}\sin\phi(t)\,, \tag{3.1}$$

where ϕ is the angle of the pendulum, $\ddot{\phi}$ is the angular acceleration, l is the length, g is the gravitational acceleration. The starting state is a random angle and a random angular velocity, in particular

$$\phi(0) \sim \mathcal{U}([-\pi, \pi])\,, \tag{3.2a}$$

$$\dot{\phi}(0) \sim \mathcal{U}([-1, 1])\,. \tag{3.2b}$$

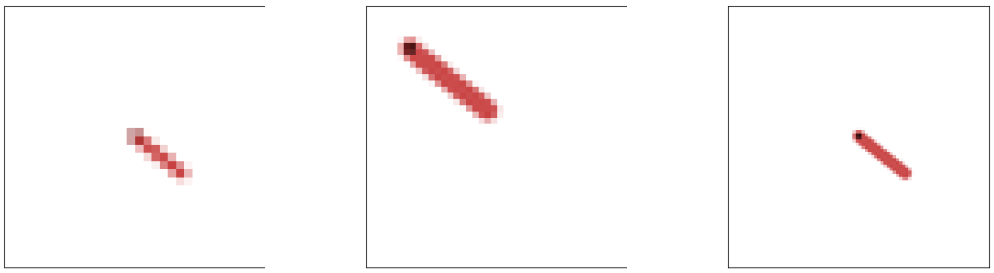

(a) Fidelity level 0 (b) Fidelity level 1 (c) Fidelity level 2

Figure 3.1: Samples from the simple pendulum dataset, at the same time instant t. (a) shows a low-resolution frame; (b) shows an high-resolution but cropped frame, to simulate partial measurements; (c) shows an high-resolution frame.

Our goal is to approximate the time-dependent state of the pendulum $x_1 = \phi, x_2 = \dot{\phi}$, considering a test set of new episodes, unseen during training.

We adopt three fidelity levels that differ in the resolution of the frame. In particular, the first fidelity level is composed of a number of (full) RGB images of size $l_0 \times l_0 \times 3$; the second level is composed of cropped RGB images of size $l_1 \times l_1 \times 3$, considering the bottom-right 60% portion of the image; the highest level of fidelity collects full RGB images of high resolution size $l_2 \times l_2 \times 3$, where $l_2 > l_0$.

Each dataset is composed of a number N^{level} of episodes, each composed of 200 consecutive frames, with $N^0 > N^1 > N^2$. The initial conditions are randomly initialised at the beginning of each episode.

Figure 3.1 shows three frames from the multi-fidelity datasets, at levels 0, 1 and 2, respectively. Table 3.1 lists the configuration parameters used for generating the dataset.

Parameters	**Level 0**	**Level 1**	**Level 2**
N	150	80	50
l	32	42	84
$portion$	1	0.6	1
N_{test}	3	3	3

Table 3.1: List of configuration parameters for the pendulum dataset.

3.1.1. ID and latent variables

Our framework is able to produce an efficient and reliable low-dimensional surrogate of the pendulum system. Indeed, the Levina-Bickel algorithm applied on the two LF latent representations estimates $ID = 3$, which is slightly larger than the true state space dimension (=2), but significantly lower than the initial latent space dimension (=20), allowing us to obtain a compact 3-dimensional latent state space for the HF model.

Figure 3.2 shows the three latent variables $\theta_1^2(t)$, $\theta_2^2(t)$ and $\theta_3^2(t)$ as functions of time, for each test episode. We can recognize some periodical patterns in all three variables, as expected. However, only the first two exhibit remarkably low uncertainty, while $\theta_3^2(t)$ displays a larger variance.

3.1.2. Reconstruction and one-step forward prediction

In this subsection we illustrate the effectiveness of the model in reconstructing the frames and predicting forward in time, on new and unseen measurements, generated using a different seed.

Figures 3.3 and 3.5 show the reconstruction of the frame $\mathbf{x}_t^{HF}$, produced by the SVDKL autoencoder, and the one-step forward prediction $\hat{\mathbf{x}}_{t+dt}^{HF}$, generated by the SVDKL dynamical model, with their respective absolute errors. In particular, they consider some frames from two testing episodes.

Visually, both the reconstructions and the predictions are consistent with the actual measurement, without blurring too much the shape of the pendulum. Indeed, the absolute errors are usually displaying a marginal inaccuracy near the border of the shape and the reconstruction MSE is consistently small ($< 3 \cdot 10^{-3}$), with some periodic fluctuations, as shown in Figures 3.4 and 3.6. With respect to the forward predictions, the MSE reaches larger maxima, up to $6 \cdot 10^{-3}$.

We notice that the model is unable to capture the full dynamics of the pendulum when the oscillations are wider. The forward prediction absolute errors at times $t = 182, 183, 184$, in Figure 3.5, show the pendulum stuck at a previous state in the evolution of the system, while the actual measurements captured a wider oscillation and a larger ϕ.

These inaccuracies coincide with the system states at the beginning and at the end of the oscillation, when the angle ϕ is larger and the angular velocity $\dot{\phi}$ is approaching zero, explaining the periodical behavior of the forward prediction MSE shown in Figure 4.26.

Overall, the model is able to capture most of the system dynamics and we may suppose

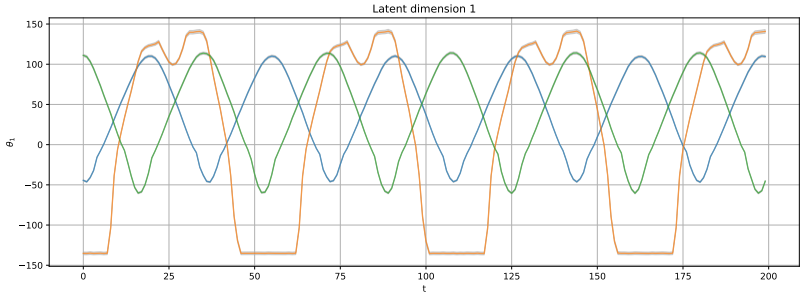

(a) $\theta_1^2(t)$

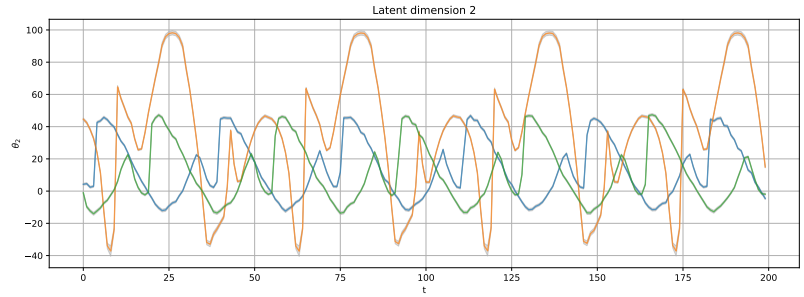

(b) $\theta_2^2(t)$

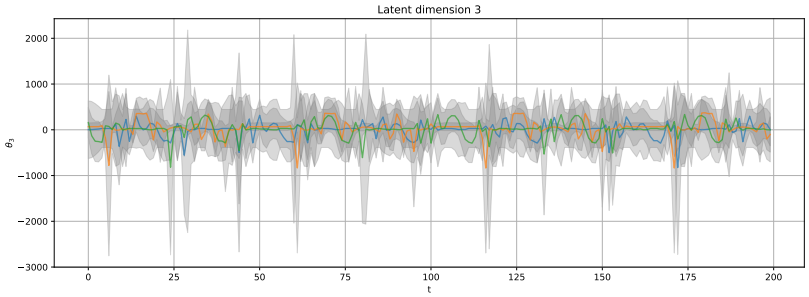

(c) $\theta_3^2(t)$

Figure 3.2: Latent variables of the fidelity level 2 autoencoder for the three test episodes, for the pendulum case. The uncertainty bands are given by $\pm$ two standard deviation in the predictive distribution. All three variables present some periodical patterns, but while $\theta_1^2(t)$ and $\theta_2^2(t)$ exhibit remarkably low uncertainty, $\theta_3^2(t)$ displays a larger variance.

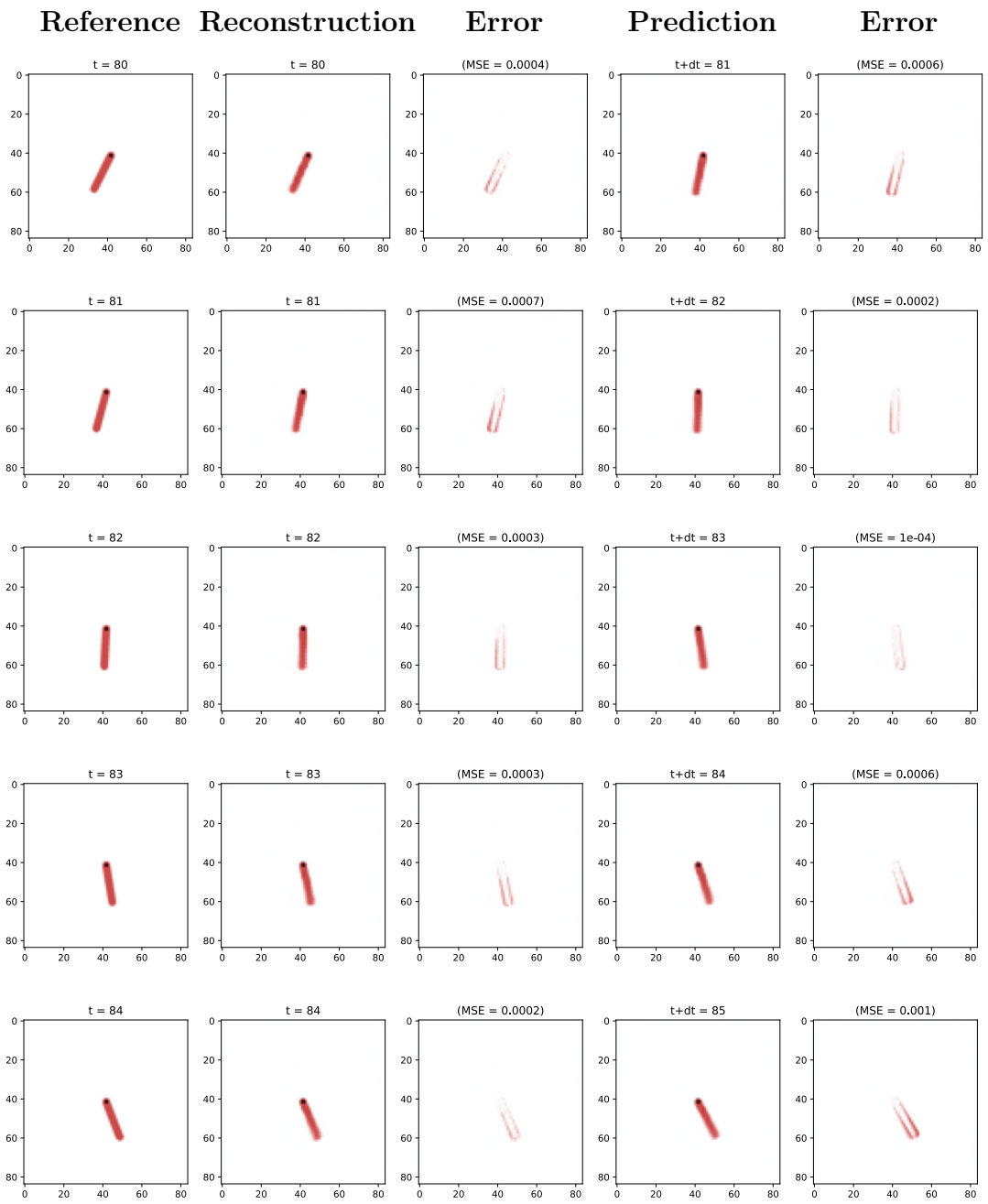

Figure 3.3: Reconstructions and predictions one-step forward in time, with respective absolute errors, of the first test episode, for the pendulum case. Both reconstruction and forward prediction are consistent and accurate during the full oscillation, when considering small angles ϕ.

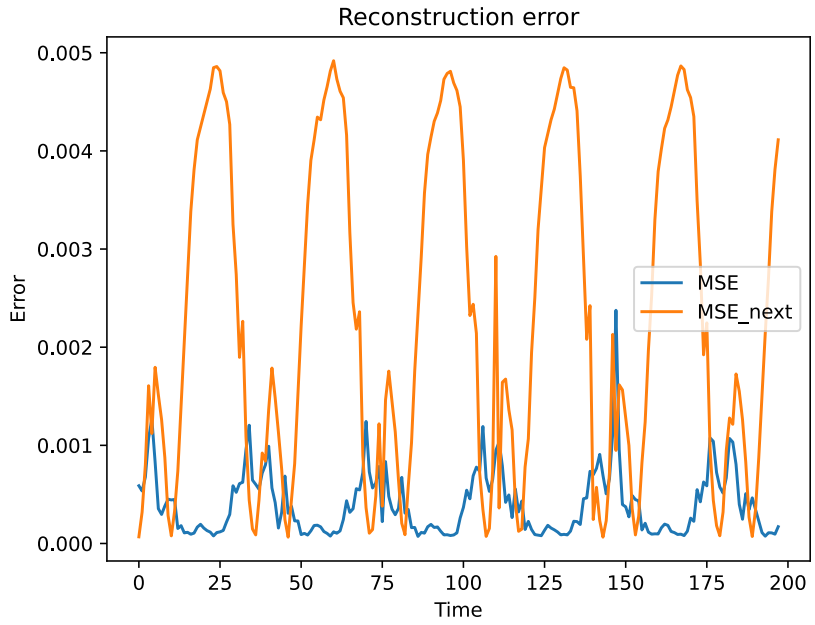

Figure 3.4: MSEs of the reconstruction and forward prediction of the first test episode, for the pendulum case, with respect to the relative true measurements, as function of time. Both MSE display a periodic behavior, while maintaining within acceptable values ($< 5 \cdot 10^{-3}$).

that training the model on measurements associated with larger initial values $\phi(0)$ $\dot{\phi}(0)$ would improve its predictive capabilities.

3.1.3. Extrapolation in time

If we iterate the one-step forward prediction, by feeding the predicted latent representation to the next iteration, we can extrapolate in time. Figure 3.7 shows some frames, obtained extrapolating in time from the first frame at $t = 0$.

Qualitatively speaking, the prediction remains consistent for a few iterations, only to degrade for the rest of the iterations. Degraded frames present a full, not blurred, shape of the pendulum, but stuck at a previous state of the evolution.

Figure 3.7 shows the first six consistent predictions, that capture the essence of the system dynamics with a full oscillation. However, the absolute error (right column of Figure 3.7) shows that the actual dynamics is slower and it is outpaced by the faster extrapolated one.

The extrapolation MSE, presented in Figure 3.8, is consistently very high, with the ex-

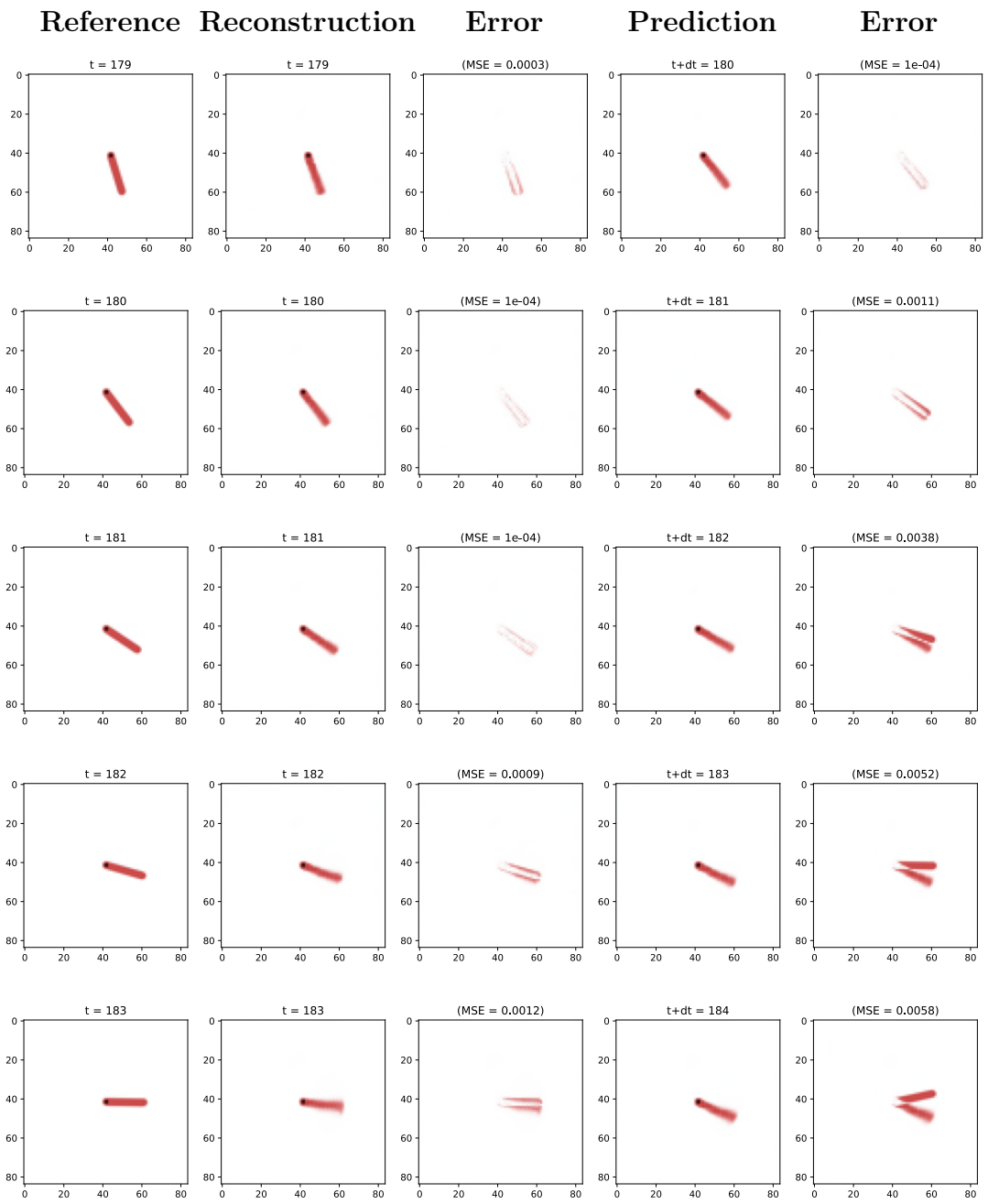

Figure 3.5: Reconstructions and predictions one-step forward in time, with respective absolute errors, of the second test episode, for the pendulum case. When considering wider oscillations, the model fails to predict forward in time the more extreme states, while retaining good reconstruction capabilities.

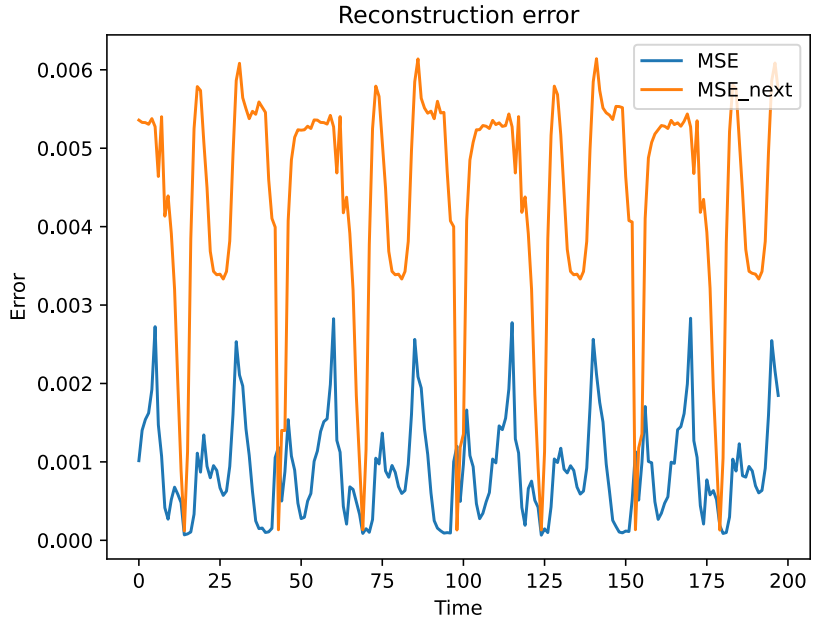

Figure 3.6: MSEs of the reconstruction and forward prediction of the second test episode, for the pendulum case, with respect to the relative true measurements, as function of time. Both MSE present a periodic behavior, with the forward prediction error reaching its maxima when the pendulum is in its most extreme phases of the oscillation.

ception of sporadic small values that coincide with the actual states close to the constant predicted one, mimicking a broken clock.

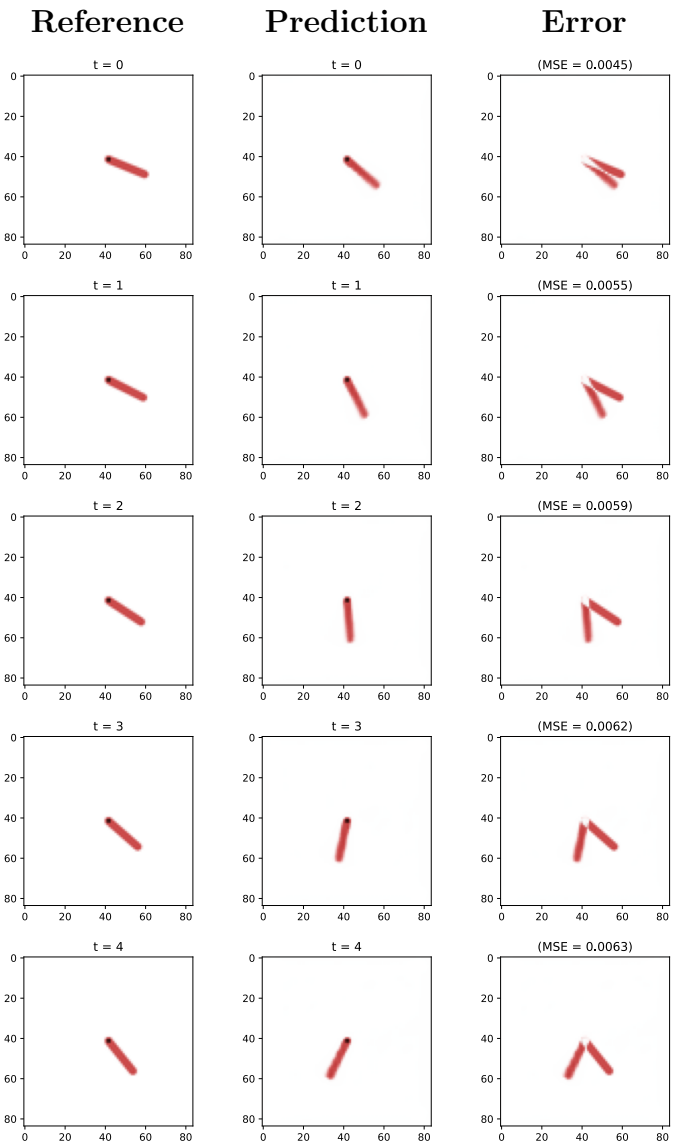

Figure 3.7: Extrapolation in time, for the pendulum case, for a few iterations, with the respective absolute error. While the oscillating dynamics is essentially captured, the extrapolated movement of the pendulum is faster than the measured $\dot{\phi}$.

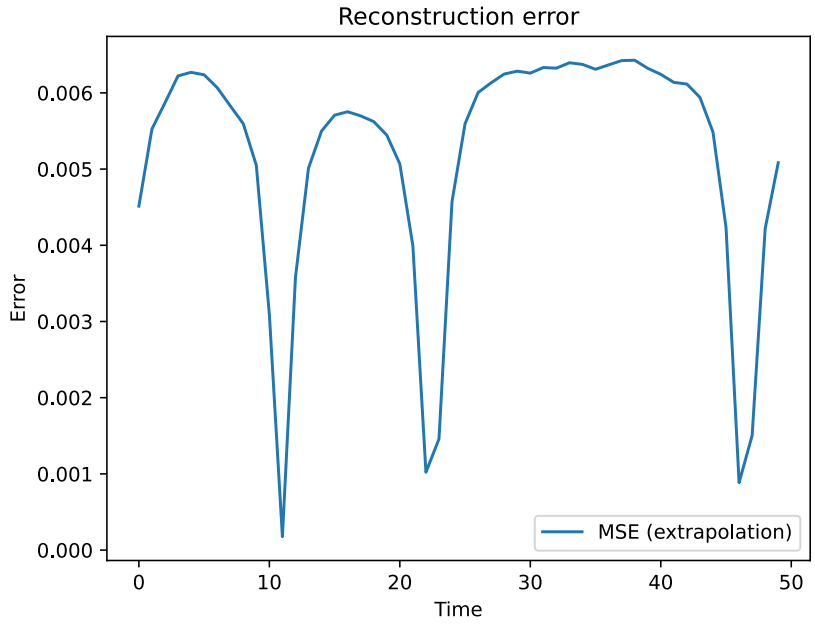

Figure 3.8: MSE of the extrapolation in time, for the pendulum case. The error is consistently high, with sporadic minima that coincide with the predicted constant state that the pendulum periodically returns to.

3.2. Acrobot

(a) Low fidelity sample (b) High fidelity sample

Figure 3.9: Samples from the acrobot dataset: (a) and (b) show two frames from the LF and HF data, respectively, at the same time instant t.

As second test-case we consider the acrobot, a planar two-link robotic arm in the vertical plane (working against gravity), with an actuator at the elbow, but no actuator at the shoulder. This low-dimensional dynamical system was first described by Murray and Hauser in [29].

Considering $\mathbf{q} = [\phi_1, \phi_2]^T$, where ϕ_1 is the shoulder joint angle and ϕ_2 is the elbow (relative) joint angle, the standard manipulator equation of the system is:

$$\mathbf{M}(\mathbf{q})\ddot{\mathbf{q}} + \mathbf{C}(\mathbf{q}, \dot{\mathbf{q}})\dot{\mathbf{q}} = \boldsymbol{\tau}_g(\mathbf{q}) + \mathbf{B}\mathbf{u} \,, \tag{3.3}$$

where

$$\mathbf{M}(\mathbf{q}) = \begin{bmatrix} I_1 + I_2 + m_2 l_1^2 + 2m_2 l_1 l_{c2} c_2 & I_2 + m_2 l_1 l_{c2} c_2 \\ I_2 + m_2 l_1 l_{c2} c_2 & I_2 \end{bmatrix}, \tag{3.4}$$

$$\mathbf{C}(\mathbf{q}, \dot{\mathbf{q}}) = \begin{bmatrix} -2m_2 l_1 l_{c2} s_2 \dot{q}_2 & -m_2 l_1 l_{c2} s_2 \dot{q}_2 \\ m_2 l_1 l_{c2} s_2 \dot{q}_1 & 0 \end{bmatrix}, \tag{3.5}$$

$$\boldsymbol{\tau}_g(\mathbf{q}) = \begin{bmatrix} -m_1 g l_{c1} s_1 - m_2 g (l_1 s_1 + l_{c2} s_{1+2}) \\ -m_2 g l_{c2} s_{1+2} \end{bmatrix}, \quad \mathbf{B} = \begin{bmatrix} 0 \\ 1 \end{bmatrix}, \tag{3.6}$$

and $\mathbf{M}$ is the inertia matrix, $\mathbf{C}$ captures Coriolis forces, τ_g is the gravity vector, the matrix $\mathbf{B}$ maps control inputs $\mathbf{u}$ into generalized forces [45]. In our case, we consider null control inputs $\mathbf{u}$, so the term $\mathbf{B}\mathbf{u}$ disappears. Additionally, we consider random initial conditions on the angles, with $\phi_1(0), \phi_2(0) \sim \mathcal{U}([-2, 2])$, and null initial velocities $\dot{\phi}_1(0) = \dot{\phi}_2(0) = 0$.

Our goal is to approximate the time-dependent state of the acrobot $\mathbf{x} = [\mathbf{q}, \dot{\mathbf{q}}]$, considering a test set of new episodes, unseen during training.

We adopt two fidelity levels that differ in the resolution of the frame. In particular, the LF level is composed of a number of RGB images of size $l_{LF} \times l_{LF} \times 3$, while the HF level collects RGB images of high resolution size $l_{HF} \times l_{HF} \times 3$, where $l_{HF} > l_{LF}$.

Each dataset is composed of a number N^{level} of episodes, each composed of 500 consecutive frames, with $N^{LF} > N^{HF}$. The initial conditions are randomly initialised at the beginning of each episode.

Figure 3.9 shows two frames from the LF and HF datasets, respectively. Table 3.2 lists the configuration parameters used for generating the dataset.

Parameters	LF	HF
N	150	50
l	32	84
$portion$	1	1
N_{test}	3	3

Table 3.2: List of configuration parameters for the acrobot dataset.

3.2.1. ID and latent variables

Also in the acrobot case, our model is able to produce an efficient low-dimensional surrogate of the system state. The Levina-Bickel algorithm applied on the LF latent representation estimates $ID = 4$, which is coherent with our theoretical knowledge of the problem.

Figure 3.10 shows the four latent variables $\theta_1^2(t)$, $\theta_2^2(t)$, $\theta_3^2(t)$ and $\theta_4^2(t)$ as functions of time, for each test episode. All of them exhibit regular and periodic behaviour, and no uncertainty, with the $\pm 2\sigma$ bands barely visible. However, some accuracy issues described in the following sections may suggest that this latent space is too restrictive for a complete learning of the system dynamics.

3.2.2. Reconstruction and one-step forward prediction

In this subsection we illustrate the effectiveness of the model in reconstructing the frames and predicting one step forward in time, on new and unseen measurements on the acrobot system, generated using a different seed.

Figure 3.11 shows the reconstruction of the frame $\mathbf{x}_t^{HF}$, produced by the SVDKL autoencoder, and the one-step forward prediction $\hat{\mathbf{x}}_{t+dt}^{HF}$, generated by the SVDKL dynamical

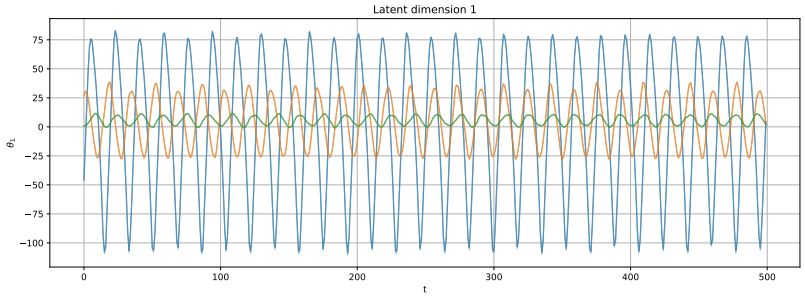

(a) $\theta_1^{HF}(t)$

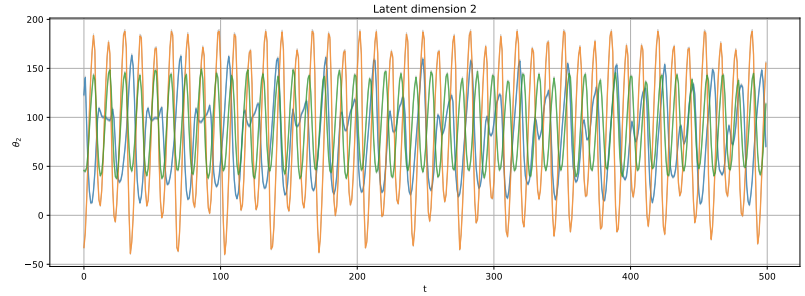

(b) $\theta_2^{HF}(t)$

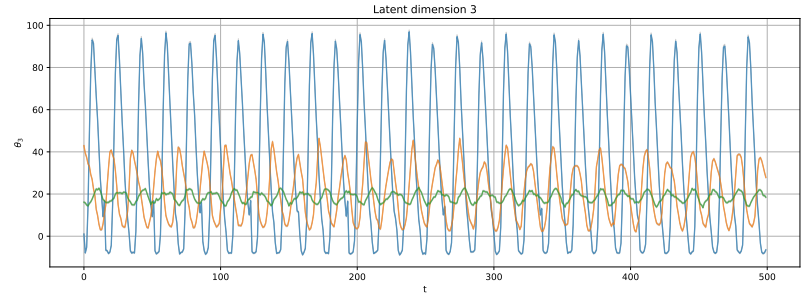

(c) $\theta_3^{HF}(t)$

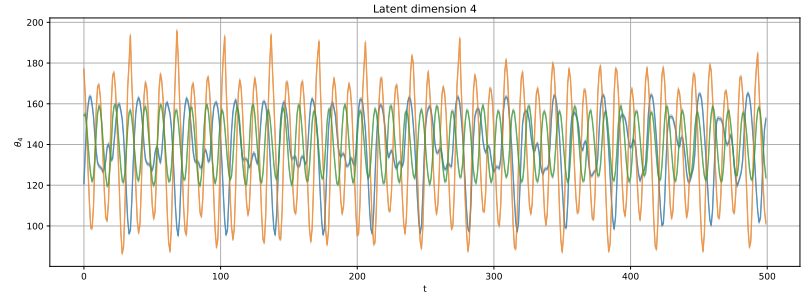

(d) $\theta_4^{HF}(t)$

Figure 3.10: Latent variables of the HF fidelity level autoencoder for each test episodes, for the acrobot case. The uncertainty bands are given by $\pm$ two standard deviation in the predictive distribution, but are barely visible. The variables all display regular and periodic behaviour.

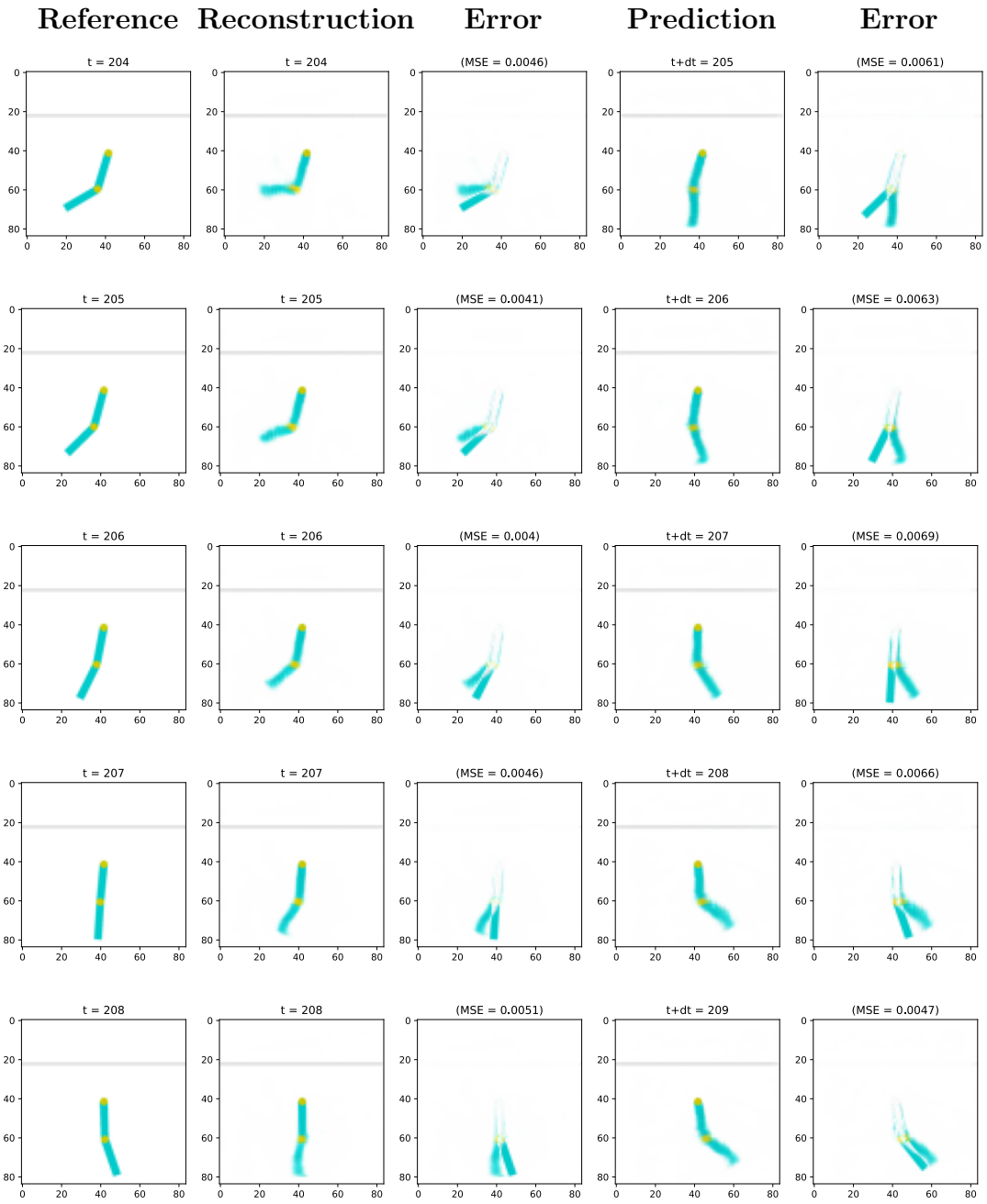

Figure 3.11: Reconstructions and predictions one-step forward in time, with respective absolute errors, of the first test episode, for the acrobot case. The predictions on the first arm are always accurate, while the trajectory of second arm is consistent, but degraded and delayed.

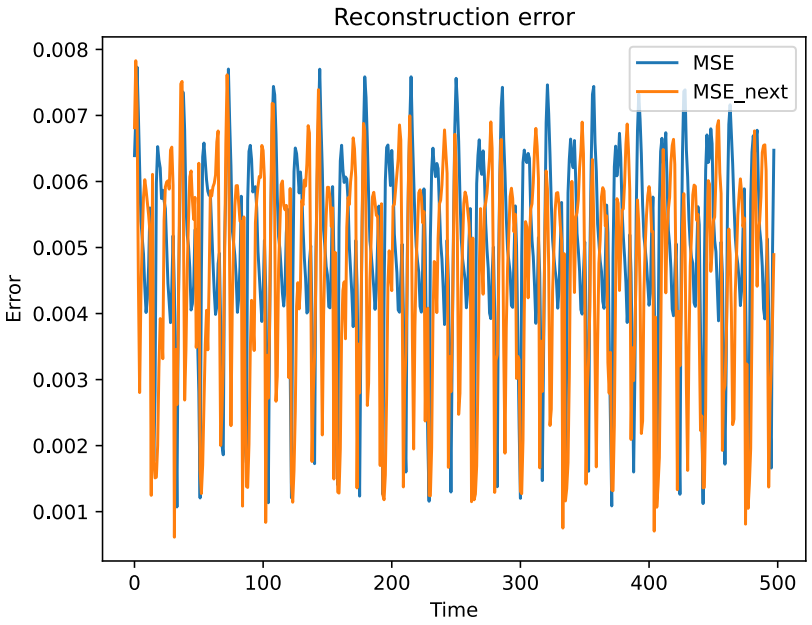

Figure 3.12: MSEs of the reconstruction and forward prediction of the first test episode, for the acrobot case, with respect to the relative true measurements, as function of time. Both MSEs display fluctuations, alternating good predictions to slightly inaccurate ones ($MSE \approx 0.008$).

model, with their respective absolute errors. In particular, it considers some frames from the first testing episode.

Differently from the simple pendulum case, in Figure 3.11 we notice some evident inaccuracies with respect to the trajectory of the second arm. While the first arm is accurately reconstructed and its dynamics is learnt reasonably well by the model, the second one displays slightly degraded and blurred reconstructions, and the dynamics seems delayed, tracking behind the measured one.

The absolute errors show an almost absent discrepancy between the true trajectory of the first arm and the predicted ones, both in the sense of sole reconstruction and one-step forward prediction. On the other hand, the second arm reconstructed trajectory follows behind its true counterpart by a small angle, and it closely precedes it when forward predicting.

Figure 3.12 displays the behaviour in time of the reconstruction and forward prediction MSE. They both exhibit strong and quasi-periodic fluctuations, up to maxima $MSE \approx 0.008$. Most of the error is related to the poor prediction capabilities of the second arm trajectories, which is still predicted accurately when the true and predicted dynamics

occasionally sync (usually, when the angular velocity are near zero).

Overall, the model is able to capture some of the system dynamics and we may suppose that considering a slightly larger latent state space dimension, namely overestimating ID, would improve its predictive capabilities.

3.2.3. Extrapolation in time

If we iterate the one-step forward prediction, by feeding the predicted latent representation to the next iteration, we can extrapolate in time. Figure 3.13 shows some frames, obtained extrapolating in time from the first frame at $t = 0$.

Qualitatively speaking, the prediction remains consistent only for a few iterations, to degrade for the rest of the considered time interval. Degraded frames present a full, slightly blurred, shape of the acrobot, but stuck at a previous state of the evolution.

Figure 3.13 shows the first five moderately consistent predictions, that capture the essence of the system dynamics with a full oscillation. While the first frame is reasonably accurate, with the exception of a small shifting of the second arm angle, the second frame is already heavily degraded. The next few iterations are able to capture the essence of the system dynamics, with the angle at the elbow reducing over time, but the overall system state is not satisfying

The MSE shown in Figure 3.14 displays some fluctuations, with local minima that associate with occasional moderately accurate prediction. However, the system dynamics does not seem to be captured by the model in its entirety.

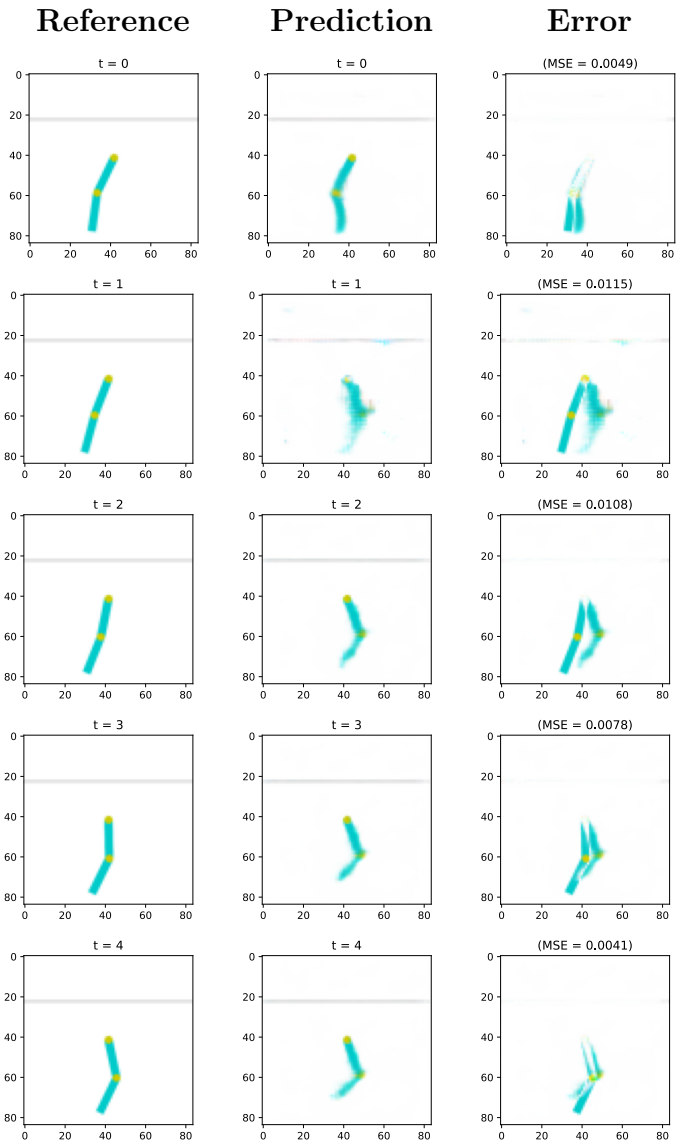

Figure 3.13: Extrapolation in time, for the pendulum case, for a few iterations, with the respective absolute error. The essence of the dynamics is present, but its not accurately predicted.

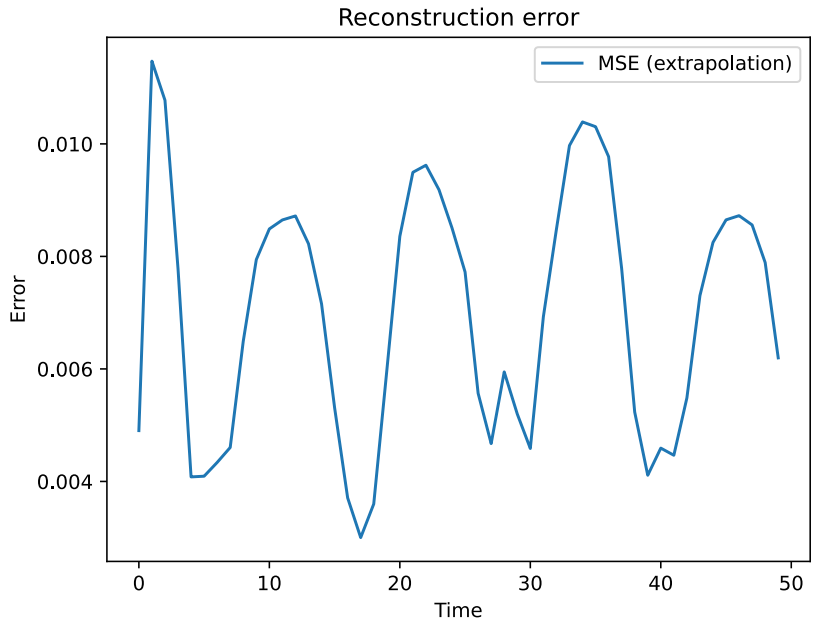

Figure 3.14: MSE of the extrapolation in time, for the acrobot case. The large fluctuations associate with a defective learning of the system dynamics.

3.3. Some considerations

Our framework proves very effective in learning the dynamics of low dimensional dynamical systems, as the pendulum and the acrobot, from high-dimensional measurements. Additionally, the Levina-Bickel algorithm produces an efficient but relatively exhaustive representation of the system state space. The efficiency of the model is also highlighted by the significantly low uncertainty exhibited when predicting the latent state.

The model is able to leverage a variety of data sources of different fidelity to capture and predict trajectories of the system, unseen during the training stage. However, for this particular class of problems, the task of extrapolation in time remains open, with the model still lacking accuracy.

From a qualitative standpoint, the MF framework allows to deal with a reduced amount of HF measurements, with respect to the work by Botteghi et al. [4] (we used $\frac{2}{3}$ of the observations originally used, in the pendulum case). Moreover, the results achieved by Chen et al. in [9] considered around an order of magnitude more observations. An additional benefit from the MF framework is to learn ID and to include it directly inside the model, taking a step forward in the direction of improving the interpretability of the latent state variables.

Quantitatively speaking, Table 3.3 collects the mean in time of the MSEs in the simple pendulum case, for both reconstruction and forward prediction, comparing the results of our MF model with a SF model that considers only level 0 LF data. We can notice a slight improvement in accuracy for all the tested episodes, which is notable, especially considering that the latent space dimension of the SF model is not bounded by ID.

	Reconstruction $\overline{\text{MSE}}(t)$		**Forward prediction** $\overline{\text{MSE}}(t)$	
Episode	**MF**	**SF**	**MF**	**SF**
Episode 1	$4.2048 \cdot 10^{-4}$	$9.9681 \cdot 10^{-4}$	$2.2964 \cdot 10^{-3}$	$3.2726 \cdot 10^{-3}$
Episode 2	$8.9107 \cdot 10^{-4}$	$1.0004 \cdot 10^{-3}$	$4.3134 \cdot 10^{-3}$	$4.8076 \cdot 10^{-3}$
Episode 3	$3.9761 \cdot 10^{-4}$	$9.8603 \cdot 10^{-4}$	$2.4977 \cdot 10^{-3}$	$3.3353 \cdot 10^{-3}$

Table 3.3: Comparison of the mean in time of the MSEs, in the pendulum case, for both reconstruction and forward prediction, between the MF model and a SF model that considers only LF data.

From a computational standpoint, on the hardware at our disposal, the training phase required a few days of work, considering the dataset sizes reported in Tables 3.1 and 3.2.

Overall, we expected this to be a computationally taxing task, since the model follows an unsupervised data-driven approach and requires large datasets.

4 | High-dimensional dynamical systems from PDE discretisation

In this chapter we assess the model performance on data from high-dimensional dynamical systems from PDE discretisation, considering, in particular, the reaction-diffusion and the diffusion-advection problems. In this case, input data are high-dimensional RGB images, that represent the heatmap of the numerical solution, obtained through a numerical solver for a variety of parameters. In this context, with respect to more accurate measurements, LF datasets are characterised by coarser meshes, but longer periods of observation and larger parameter sets.

In the next sections, the theoretical details of the PDE problems are introduced, along with the specifics of the datasets and the configuration of the model. The Levina-Bickel estimate of the intrinsic dimension is discussed and the behaviour of the latent variables is presented.

The model performances are measured in terms of accuracy of the frame reconstruction and one-step forward prediction in time of the dynamics. Additionally, we study the model ability to extrapolate the system evolution in time. In particular, we examine a variety of parameter values, both seen and unseen during the training stage.

4.1. Reaction-diffusion problem

We consider a lambda-omega reaction-diffusion system defined by the following equations

$$\dot{u} = \left(1 - \left(u^2 + v^2\right)\right) u + \mu \left(u^2 + v^2\right) v + d \left(u_{xx} + u_{yy}\right), \tag{4.1a}$$

$$\dot{v} = -\mu \left(u^2 + v^2\right) u + \left(1 - \left(u^2 + v^2\right)\right) v + d \left(v_{xx} + v_{yy}\right) \tag{4.1b}$$

defined over a spatial domain $(x, y) \in [-L, L]^2$ and a time span $t \in [0, T]$, where μ and d

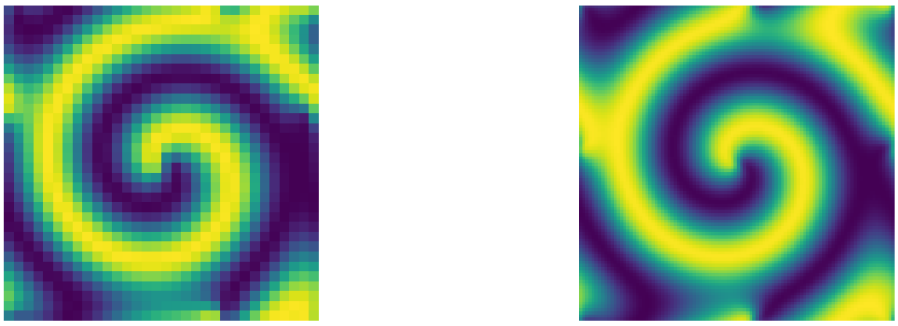

(a) Low fidelity sample (b) High fidelity sample

Figure 4.1: Samples from the reaction-diffusion dataset: (a) and (b) show two frames from the LF and HF data, respectively, at the same time instant t.

are the reaction and diffusion parameters, respectively. The initial condition is defined as

$$u(x, y, 0) = v(x, y, 0) = \tanh\left(\sqrt{x^2 + y^2}\cos\left((x + iy) - \sqrt{x^2 + y^2}\right)\right). \tag{4.2}$$

We are interested in approximating the solution components u and v as functions of the varying reaction parameter $\mu \in \mathcal{P} = [0.5, 1.5]$, with a fixed diffusion coefficient d.

We train the model on a small amount of HF data, with respect to both the time length of observation and the number of considered parameter μ values, and on a larger amount of cheaper LF data. In particular, LF data are associated with a coarser grid of discretisation ($n^{LF} < n^{HF}$), but are observed for a longer time window, $T^{LF}_{train} > T^{HF}_{train}$.

After the training stage, the model is tested on new measurements of the system for the time window $[T^{HF}_{train}, T^{HF}_{train} + T_{test}]$, for values of the parameter μ seen by the HF sub-model during training, but also extrapolating over $\mathcal{P}$.

Table 4.1 lists the configuration parameters used for generating the dataset. Figure 4.1 shows two frames from the LF and HF datasets, respectively.

4.1.1. ID and latent variables

Our workflow exploits the Levina-Bickel algorithm (cf. Chapter 1) to compute an estimate of the ID of the dynamical system and produce an efficient and reliable low-dimensional surrogate model. In the case of the reaction-diffusion system, the algorithm estimates $ID = 2$, hence restricting the latent state space for the HF model to a two-dimensional

Parameters	LF	HF
n	32	100
d	0.05	0.05
μ_{train}	{0.5, 0.75, 1, 0.6, 1.15, 1.375}	{0.5, 0.75, 1}
T_{train}	80	40
L	10	
dt	0.01	
μ_{test}	{0.5, 1, 0.6, 1.15}	
T_{test}	10	

Table 4.1: List of configuration parameters for the reaction-diffusion dataset.

space, which is consistent with our prior theoretical knowledge.

Figure 4.2 shows the latent variables $\theta_1^{HF}(t)$ and $\theta_2^{HF}(t)$ as functions of time, for each value of $\mu \in \mathcal{P}_{test}$. While it is challenging to interpret the latent variables highly irregular behavior, we can assess their significance from the accuracy of the reconstructions and forward predictions the model produces (reported in the following subsections).

4.1.2. Results for parameter value $\mu = 0.5$

In this subsection, we illustrate the effectiveness of the model, in reconstructing the frames and predicting forward in time, for the testing parameter value $\mu = 0.5$, $t \in [40, 50]$. While this specific value of the parameter μ is seen by both the portions of the model during the training stage, the evolution of the system beyond $T = 40$ is unknown by the HF sub-model.

Figure 4.3 shows the reconstruction of the frame $\mathbf{x}_t^{HF}$, produced by the SVDKL autoencoder, and the one-step forward prediction of $\mathbf{x}_{t+dt}^{HF}$, generated by the SVDKL dynamical model, with their respective absolute errors. From a qualitative point of view, both the reconstructions and the predictions are consistent with the actual evolution of the system across the testing time window.

The MSEs of both reconstructions and forward predictions show some fluctuations, with a maximum of $MSE \approx 0.025$ reached around the first few iterations. Overall, they assume similar values decrease over time, with a minimum of $MSE \approx 5 \cdot 10^{-3}$, as shown by Figure 4.4.

If we iterate the one-step forward prediction, by feeding the predicted latent representa-

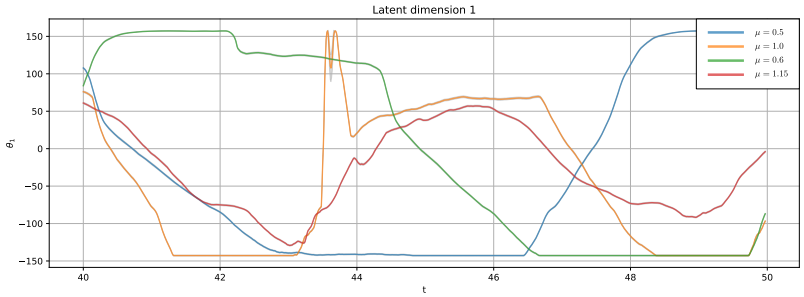

(a) $\theta_1^{HF}(t)$

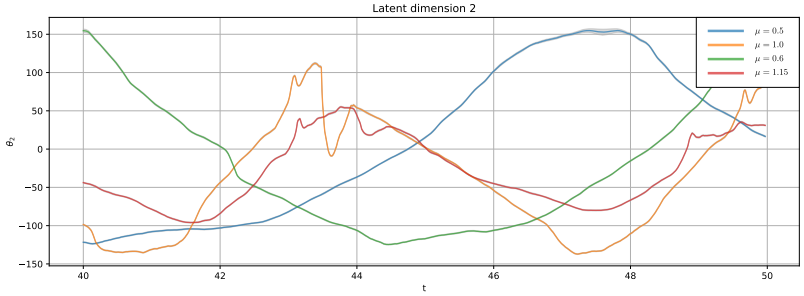

(b) $\theta_2^{HF}(t)$

Figure 4.2: Latent variables of the HF autoencoder during the test time window, for each value of the parameter μ, for the reaction-diffusion case. The uncertainty bands are given by $\pm$ two standard deviation in the predictive distribution.

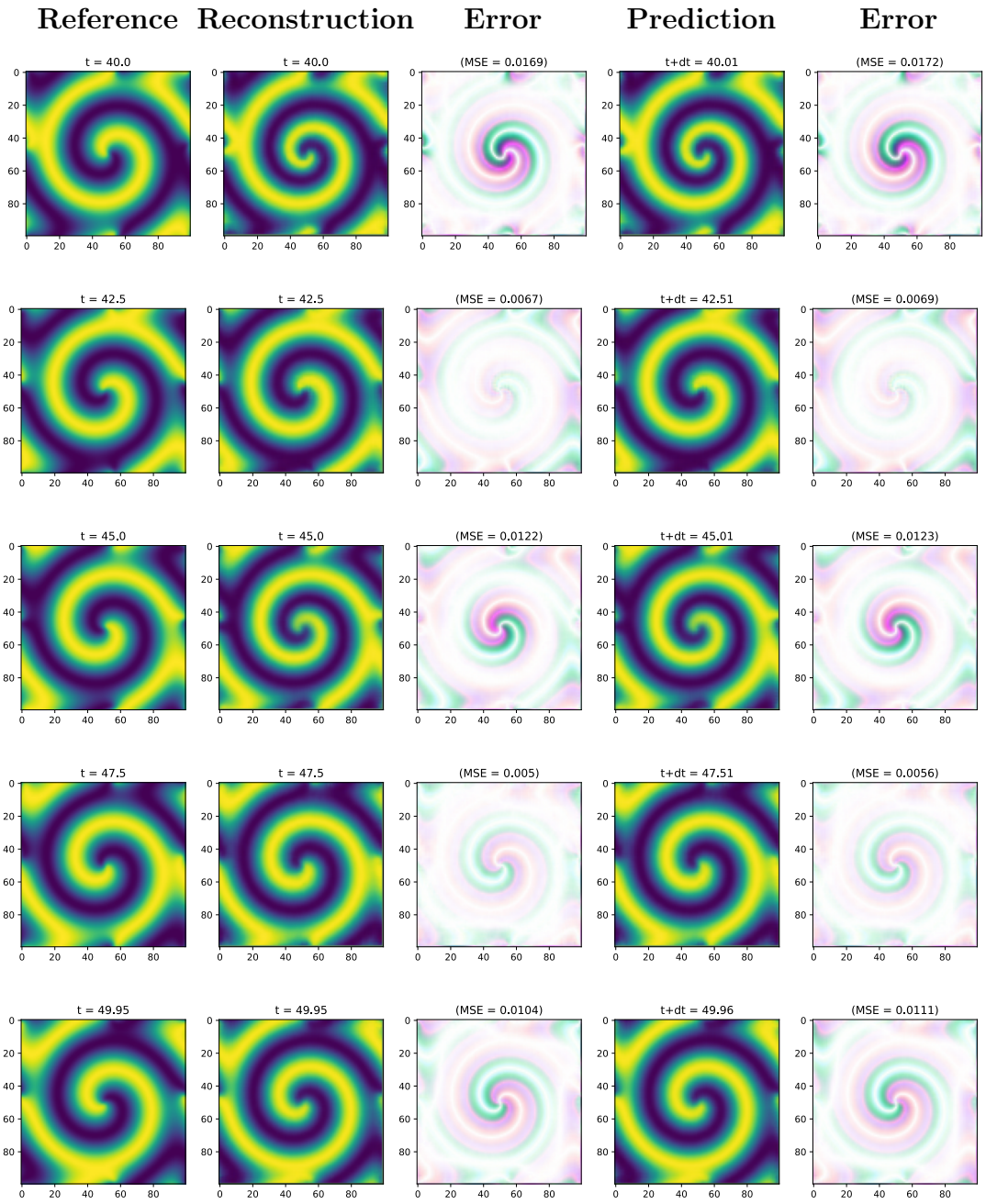

Figure 4.3: Reconstructions and predictions one-step forward in time, with respective absolute errors, for $\mu = 0.5$, reaction-diffusion test case. Both reconstructions and forward predictions are always consistent, with an absolute error that is sometimes more evident where the gradient is higher.

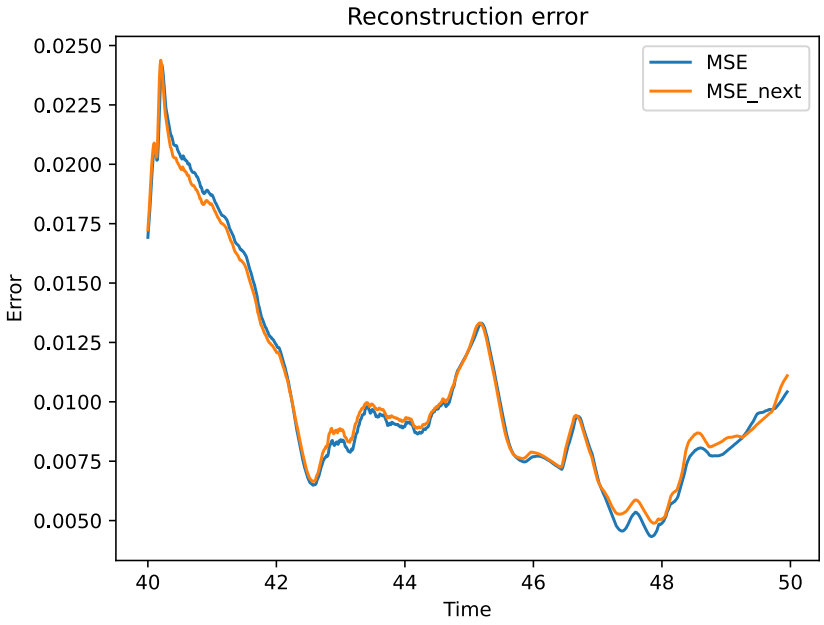

Figure 4.4: MSEs of the reconstruction and forward prediction for $\mu = 0.5$, reaction-diffusion test case, with respect to the relative true measurements, as function of time. The MSEs of both reconstructions and forward predictions assume similar values over the testing time window and decrease in time, overall, reaching a minimum of $MSE \approx 5 \cdot 10^{-3}$.

tion to the next iteration, we can extrapolate in time. Figure 4.5 shows some extrapolated frames, starting from the observation at time $t = 40$. Qualitatively speaking, the prediction remains consistent across the entire testing time window, namely, for 50 consecutive iterations. The absolute error is visually satisfying, highlighting only a slight departure from the actual frame around the most internal part of the spiral.

Figure 4.6 shows the MSE error of the extrapolation with respect to the actual measurements: it stays almost constant for the first 10 iterations around a value of $MSE \approx 0.017$, and then it linearly increases in time.

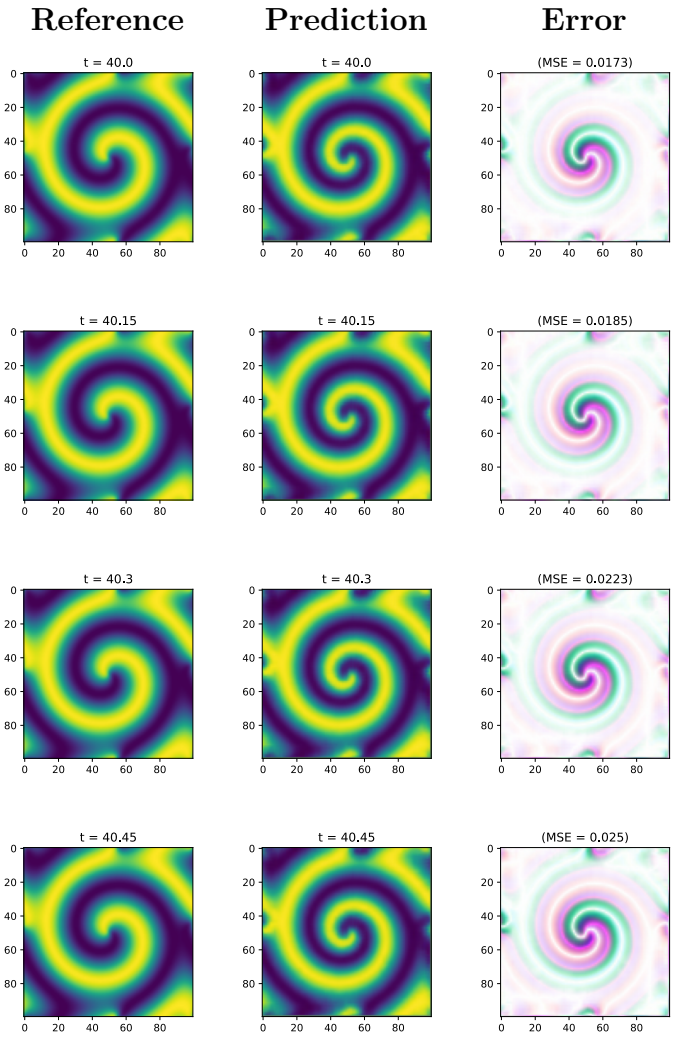

Figure 4.5: Extrapolation in time for $\mu = 0.5$, reaction-diffusion test case, for a few consecutive iterations, with the respective absolute error. The extrapolation in time is always consistent, with an absolute error observable only around the most internal spiral.

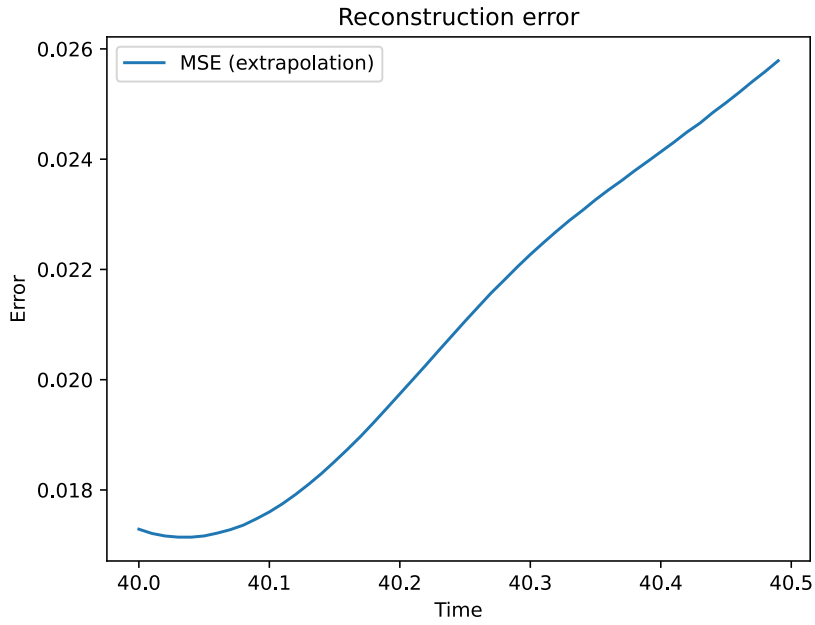

Figure 4.6: MSE of the extrapolation in time, for $\mu = 0.5$, reaction-diffusion test case. The error stays mostly constant for the first 10 iterations, and then it grows linearly.

4.1.3. Results for parameter value $\mu = 1.0$

We now present the results for the parameter value $\mu = 1.0$, for $t \in [40, 50]$. Both the LF and HF sub-models were trained on measurements from the system for $\mu = 1.0$, but the latter only until time $t \leq 40$.

Figure 4.7 shows the reconstruction of the frame $\mathbf{x}_t^{HF}$ and its one-step forward prediction $\hat{\mathbf{x}}_{t+dt}^{HF}$, with their respective absolute errors. Also in this case, both the reconstruction and the one-step prediction remain consistent across the tested time window. They seem paired in accuracy, showing very similar absolute errors. In particular, the absolute error of both is more noticeable during the second half of the time window and where the gradient is higher.

The MSEs shown in Figure 4.8, display a very similar behavior, overlapping on most of the domain. They show some minor fluctuations around a median value of about $MSE \approx 0.02$, with a curious spike around time $t = 44$.

As in the previous case, the extrapolation in time shows satisfactory results for 50 consecutive iterations. Figure 4.9 displays predictions visually consistent with the expected state of the system and the respective absolute errors that slightly worsen in time, while keeping moderate.

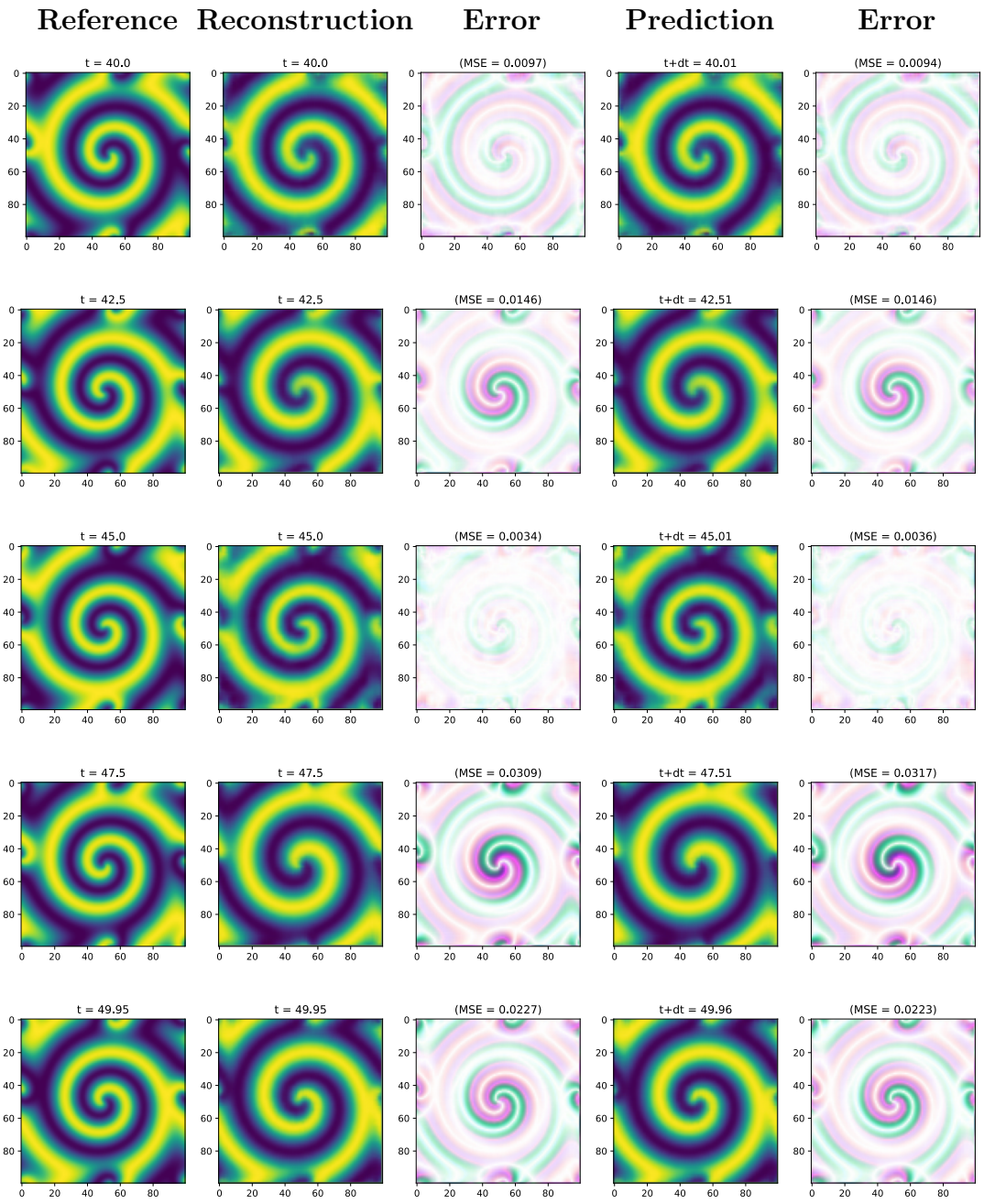

Figure 4.7: Reconstructions and predictions one-step forward in time, with respective absolute errors, for $\mu = 1.0$, reaction-diffusion test case. Both reconstructions and forward predictions are visually consistent. The plots of absolute error show a slight departure from the measurements during the second half of the time window, especially where the gradient is higher.

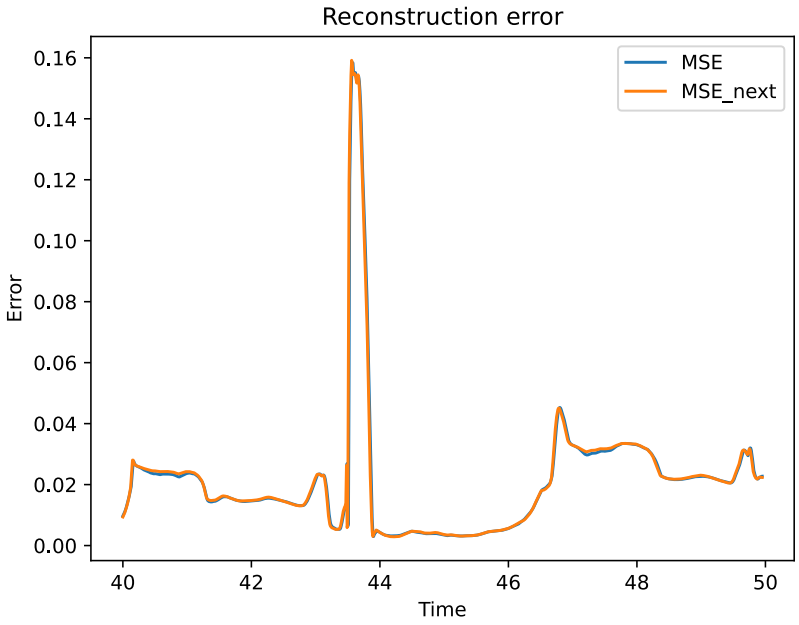

Figure 4.8: MSEs of the reconstruction and forward prediction for $\mu = 1.0$, reaction-diffusion test case, with respect to the relative true measurements, as function of time. The two error mostly overlaps across the time window and they show some fluctuations around a value of $MSE \approx 0.02$, with a spike after 4 seconds.

Indeed, the MSE with respect to the actual measurements (Figure 4.10) grows exponentially for 2/3 of the time window, from a value of $MSE \approx 0.01$, up to $MSE \approx 0.03$, and then shows a slow linear decrease.

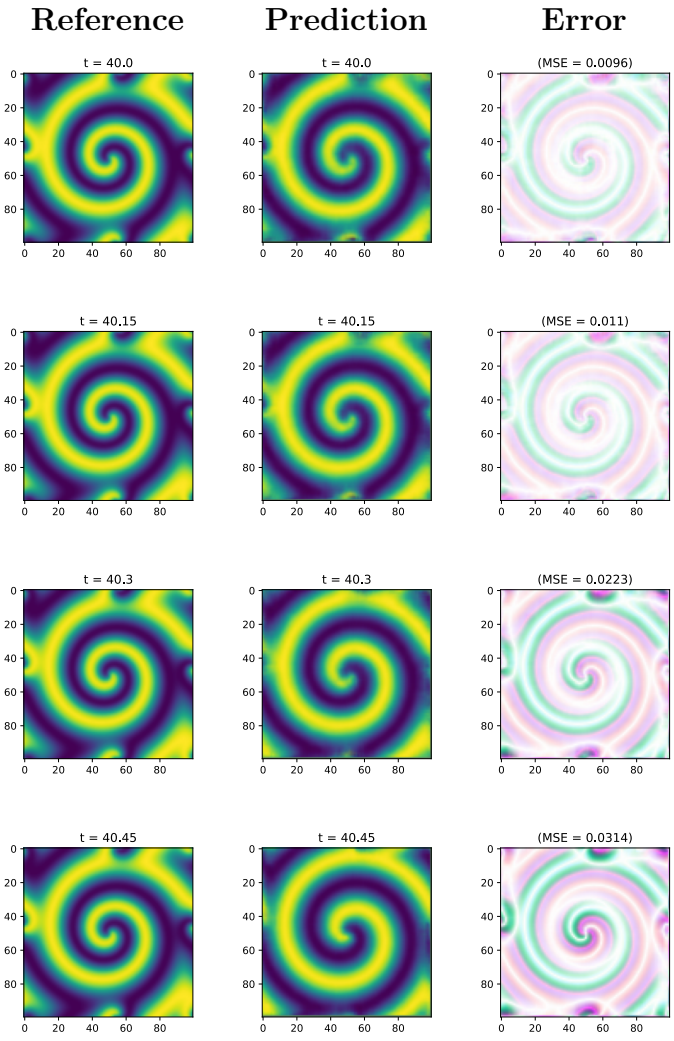

Figure 4.9: Extrapolation in time for $\mu = 1.0$, reaction-diffusion test case, for a few iterations, with the respective absolute error. The predictions are visually consistent for the entire time window.

4.1.4. Results for parameter value $\mu = 0.6$

The following results refer to the testing set for the parameter value $\mu = 0.6$, for $t \in [40, 50]$. Differently from the previous cases, here the HF sub-model has no specific knowledge on this configuration of the PDE system, since it was not trained for this value of the parameter μ, not even on the time window $[0, 40]$. On the other hand, the LF training

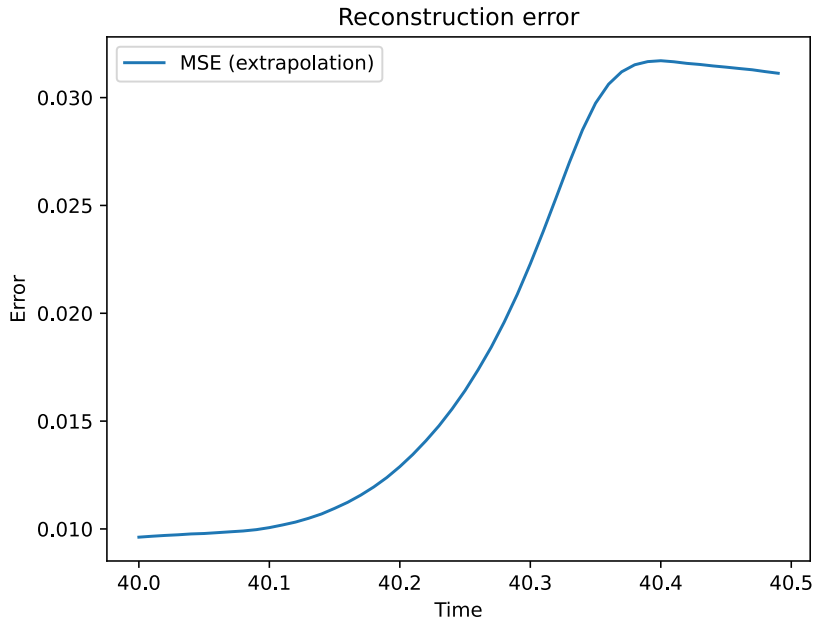

Figure 4.10: MSE of the extrapolation in time, for $\mu = 1.0$, reaction-diffusion test case. The error grows exponentially in the first part, and then follows a slow linear decrease.

test includes observations for $\mu = 0.6$, for $t \in [0, 80]$.

Figure 4.11 shows the reconstructed frame $\hat{\mathbf{x}}_t^{HF}$ and the one-step forward prediction of $\mathbf{x}_{t+dt}^{HF}$, with their respective absolute errors, for a number of iterations. We observe a general consistence of the predictions with respect to the true behavior of the system, and an high accuracy to the actual measurements. Indeed, the plots of the absolute errors show no significant discrepancies, with the exception of some slightly observable departures near the inner spiral where the gradient is higher.

The plot of the MSEs in Figure 4.12 shows very similar behaviors in time of the two errors. In particular, they both increase over the first half of the domain, up to a value of $MSE \approx 0.025$, only to decrease in the second half of the testing time window and fluctuate around a value $MSE \approx 7 \cdot 10^{-3}$. Overall, the error committed is modest, especially considering that this particular configuration of the system was not part of the training dataset.

If we extrapolate also over time, the forward predictions remain consistent for all the 50 iterations, as shows in Figure 4.13. The plots of the absolute error show a modest discrepancy with the actual measurements that accentuate in time ($MSE \approx 0.015$), especially near the boundary.

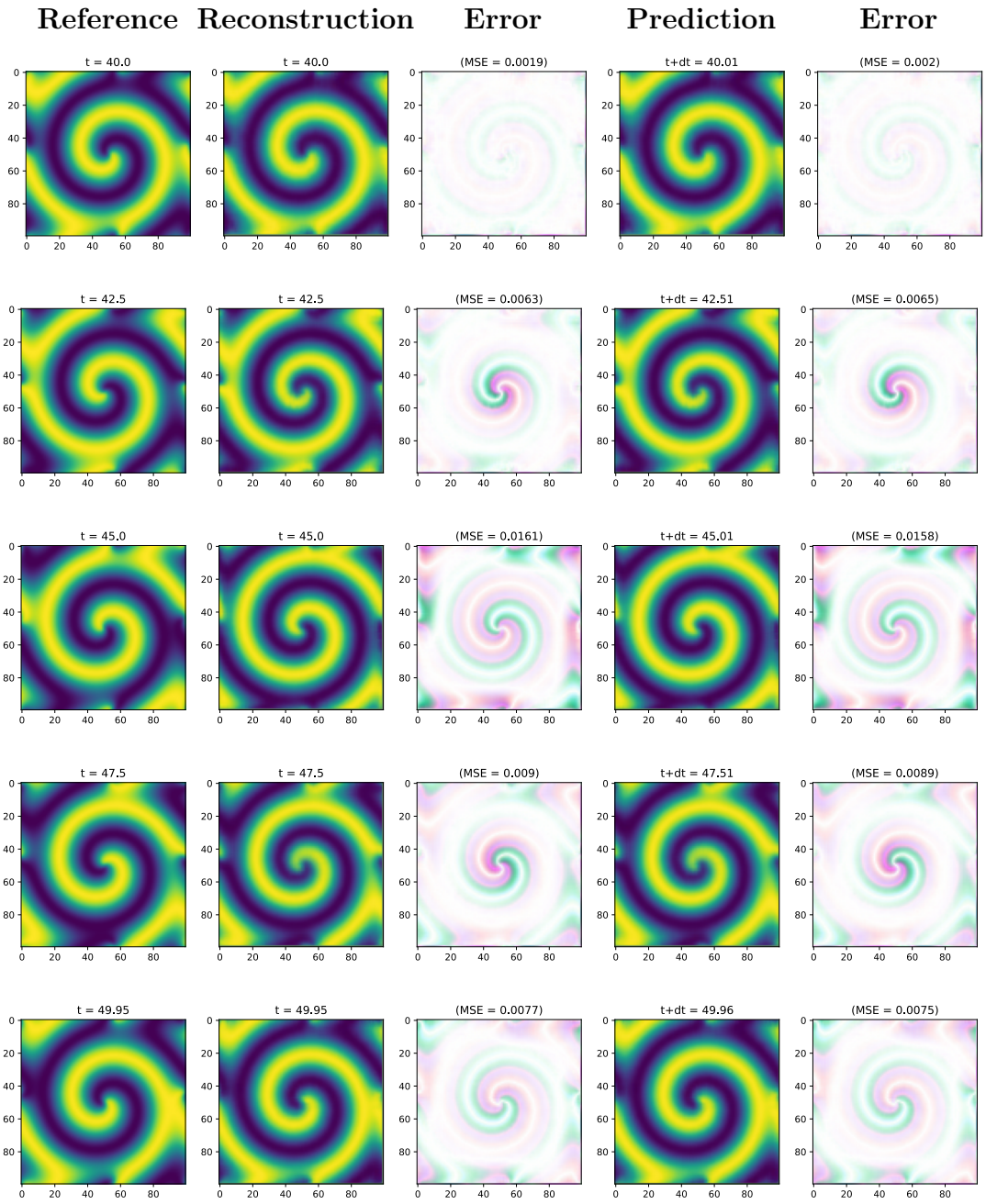

Figure 4.11: Reconstructions and predictions one-step forward in time, with respective absolute errors, for $\mu = 0.6$, reaction-diffusion test case. Both reconstructions and forward predictions are visually consistent. The plots of the absolute error show a small departure in accuracy near the central spiral, for both reconstructions and forward predictions.

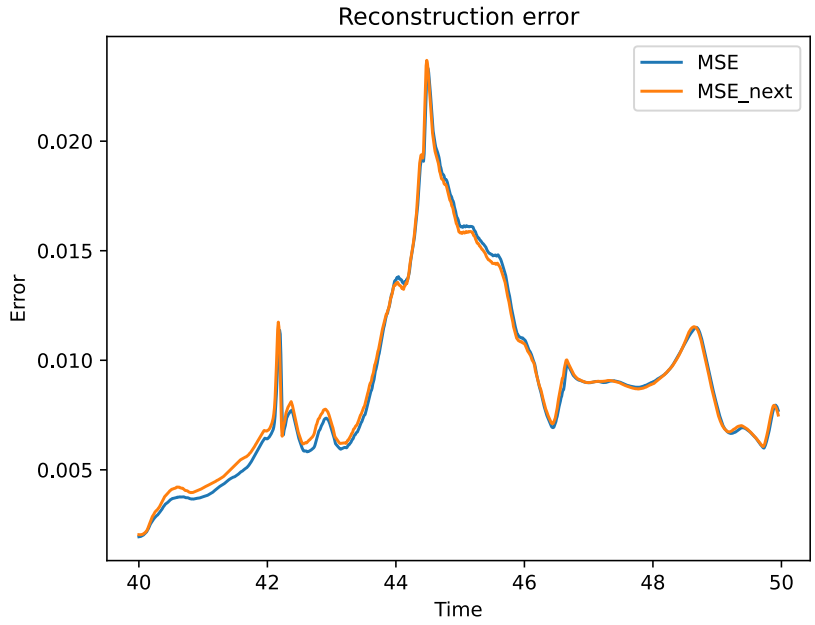

Figure 4.12: MSEs of the reconstruction and forward prediction for $\mu = 0.6$, reaction-diffusion test case, with respect to the relative true measurements, as function of time. The two errors show similar behaviors, growing during the first half of the time window, and decreasing over the second half.

Figure 4.14 shows the MSE relative to the extrapolation, which, once again, grows rapidly for the first few iterations, up to $MSE \approx 0.02$), and then slightly decreases in time. Also in this case, the error committed is modest, overall.

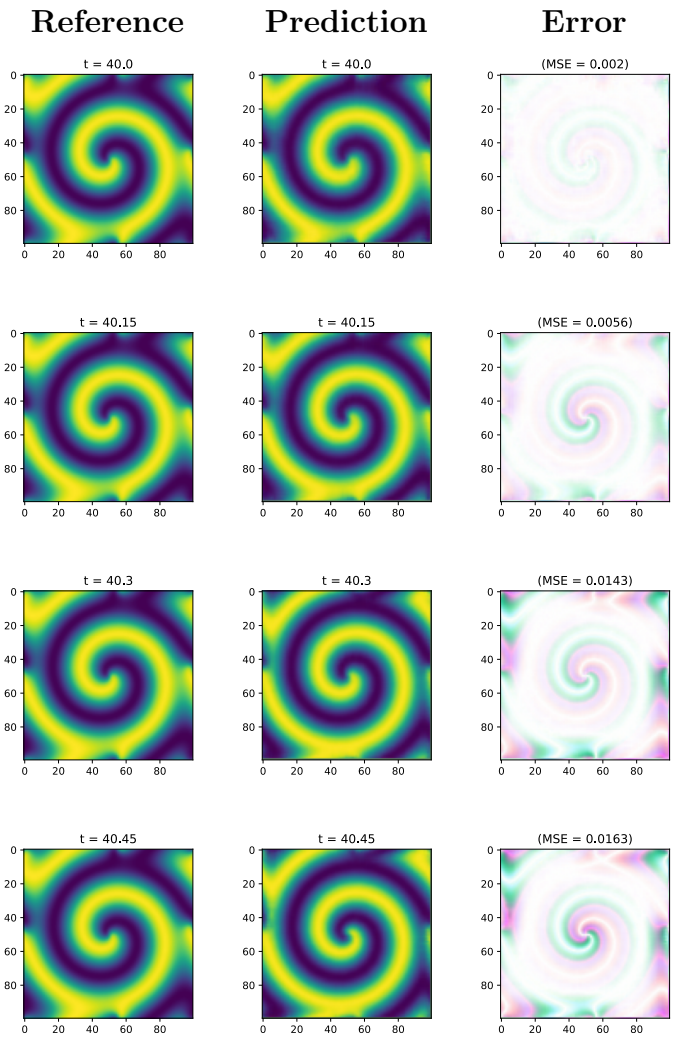

Figure 4.13: Extrapolation in time for $\mu = 0.6$, for a few iterations, with the respective absolute error. The extrapolated frames are always consistent with the true evolution and the absolute error is noticeable only near the boundary.

4.1.5. Results for parameter value $\mu = 1.15$

The last test case we present is for the parameter value $\mu = 1.15$, for $t \in [40, 50]$. As in the previous section, the HF sub-model has no specific knowledge on this configuration of the PDE system, since it was not trained for this specific value of the parameter μ, not even on the time window $[0, 40]$. More importantly, the HF has not seen any configuration

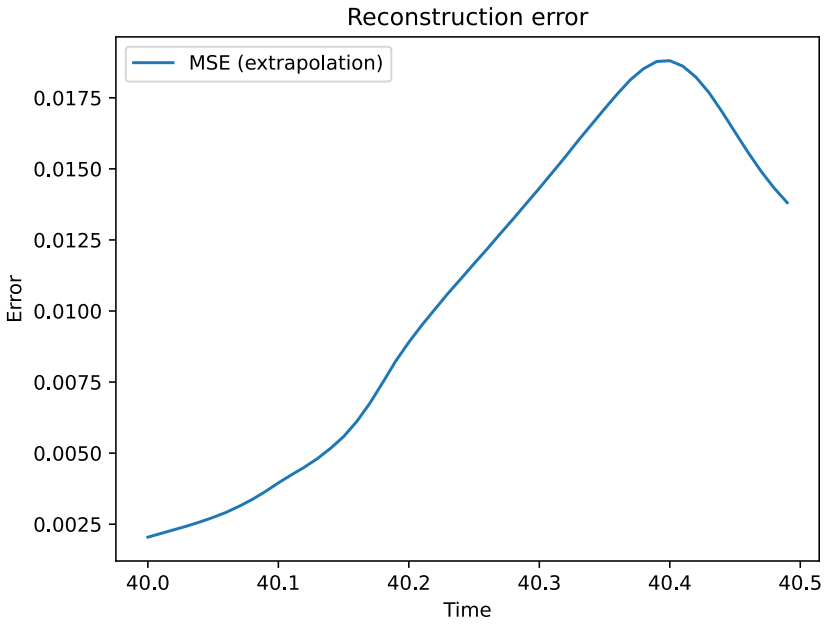

Figure 4.14: MSE of the extrapolation in time, for $\mu = 0.6$. Once again, the error grows rapidly at the beginning, and then it slightly decreases.

of the system with a reaction coefficient higher than $\mu > 1$. On the other hand, the LF training test includes observations for $\mu = 1.15$, for $t \in [0, 80]$.

Figure 4.15 shows some reconstructed frames $\hat{\mathbf{x}}_t^{HF}$ and the one-step forward predictions of $\mathbf{x}_{t+dt}^{HF}$, with their respective absolute errors. We observe a general consistence of the predictions with respect to the actual behavior of the system, with the exception of some sporadic degraded predictions. However, the plots of the absolute errors show a modest discrepancy with respect to the actual measurements, that appears less marked for the degraded frames.

Indeed, the plot of the MSEs in Figure 4.16 shows acceptable (and, once again, overlapping) reconstruction and forward prediction errors, that roughly grow in time. However, their local minima are reached approximately in occasion of the more degraded predictions.

This behavior of the model could suggest that less degraded frames are also less accurate for this particular configuration of the system, because more close to the evolution of a system with a smaller reaction coefficient. On the contrary, when the model gives up a little consistency, the prediction is more blurred but also closer to the actual measurement, and the MSE improves.

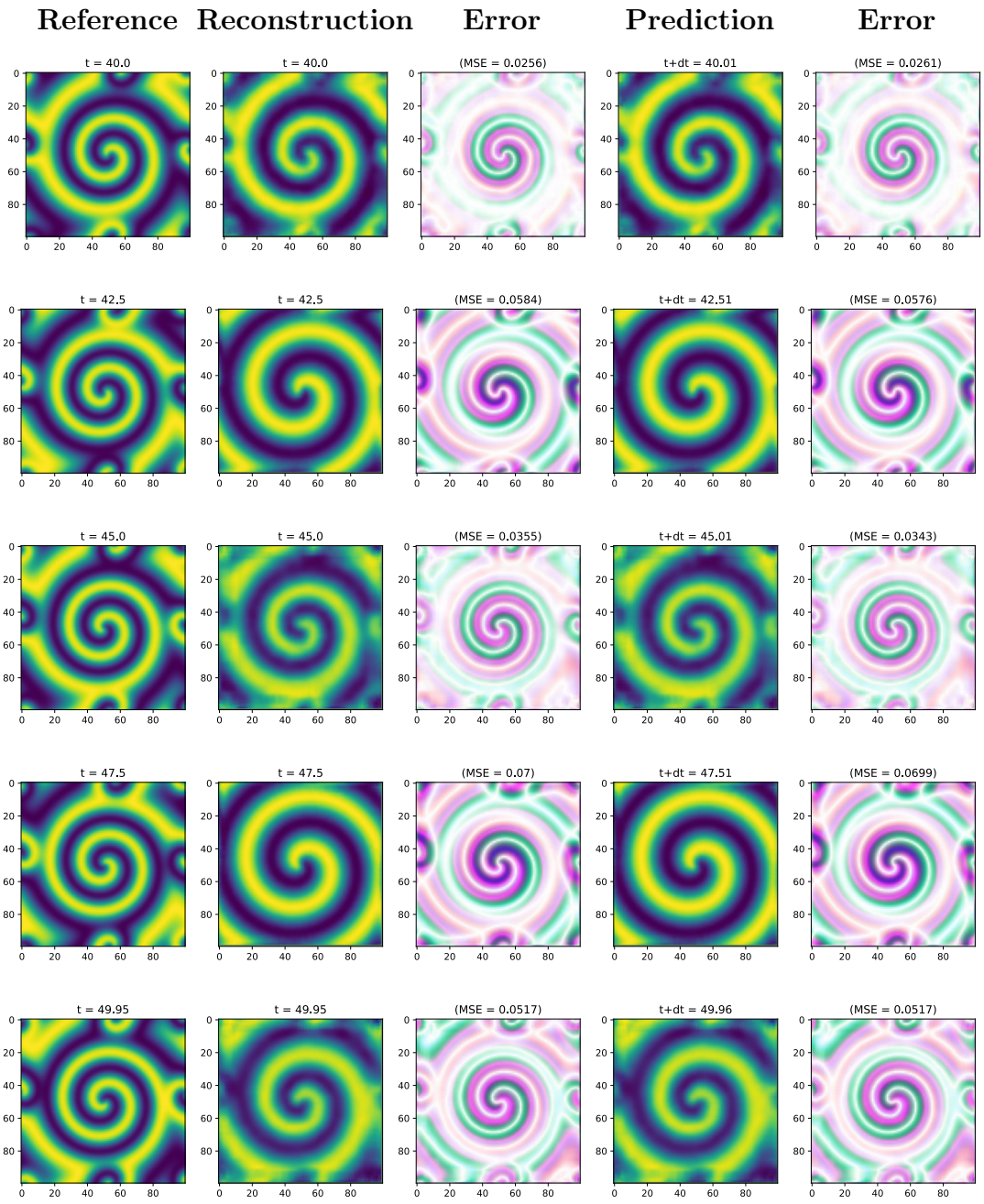

Figure 4.15: Reconstructions and predictions one-step forward in time, with respective absolute errors, for $\mu = 1.15$, reaction-diffusion test case. Both reconstructions and forward predictions are visually consistent, overall. However, we notice a small degradation around times $t = 45$ and $t = 50$. The absolute error of both reconstructions and forward predictions is modest but evident, especially where the gradient is higher.

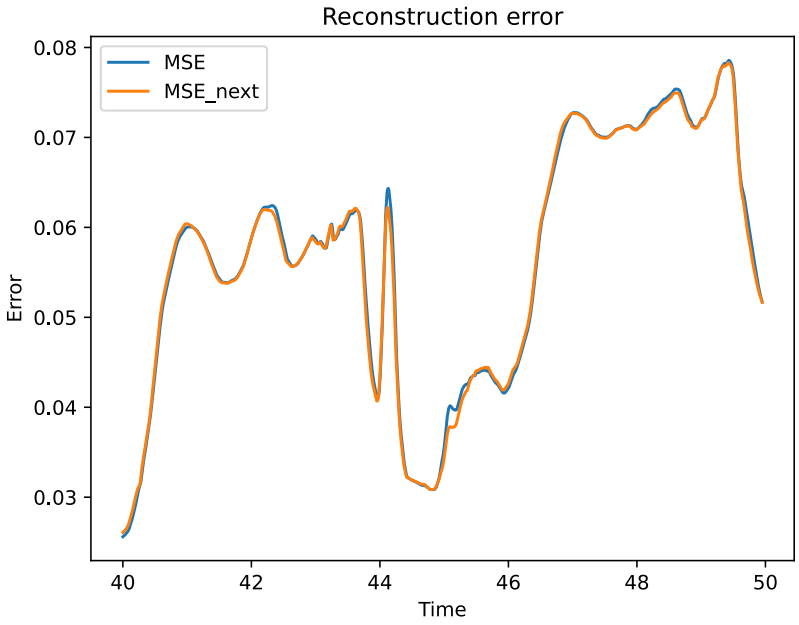

Figure 4.16: MSEs of the reconstruction and forward prediction for $\mu = 1.15$, reaction-diffusion test case, with respect to the relative true measurements, as function of time. The two errors have similar behaviors and they roughly increase in time, up to $MSE \approx 0.08$. However, they reach local minima when the predicted frame is more degraded.

If we extrapolate also over time, the forward predictions seem consistent, overall, as shown in Figure 4.17, but sligthly degraded where the gradient is higher. The plot of the absolute errors show a moderate discrepancy with the actual measurements ($MSE < 0.05$), more evident near the smaller spirals. This behavior suggests that the model has not learned the full dynamics of the system for this specific configuration of the reaction coefficient, but it is still able to produce a meaningful prediction on the basis of its global knowledge of the reaction-diffusion system.

Figure 4.18 shows the MSE relative to the extrapolation, which grows approximately linearly in time, starting from $MSE \approx 0.025$ and reaching $MSE \approx 0.05$ at the end of our extrapolation time window.

Overall, the model seems capable to learn the evolution of the reaction-diffusion system, showing a satisfying accuracy both for the reconstruction and the forward prediction stages, also when extrapolating over the parameter space. Surprisingly, the extrapolation in time is still very accurate despite the challenge, highlighting the model capability to learn the system dynamics.

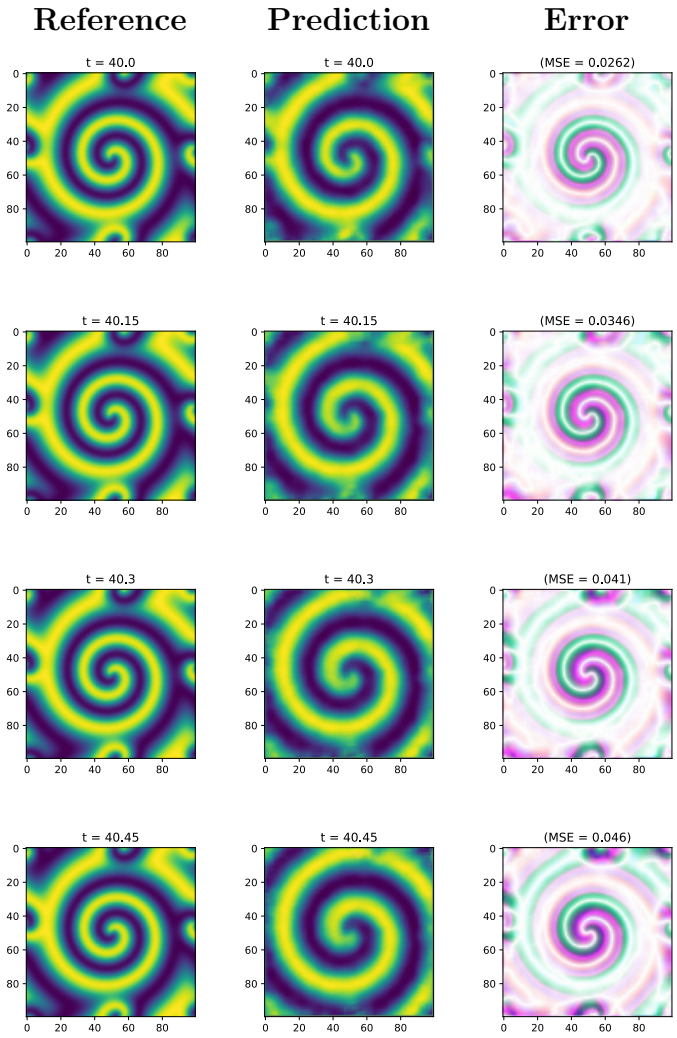

Figure 4.17: Extrapolation in time for $\mu = 1.15$, for a few iterations, with the respective absolute error. The predictions are consistent, but slightly degraded where the gradient is higher. Indeed, the absolute error is more evident near the smaller spirals.

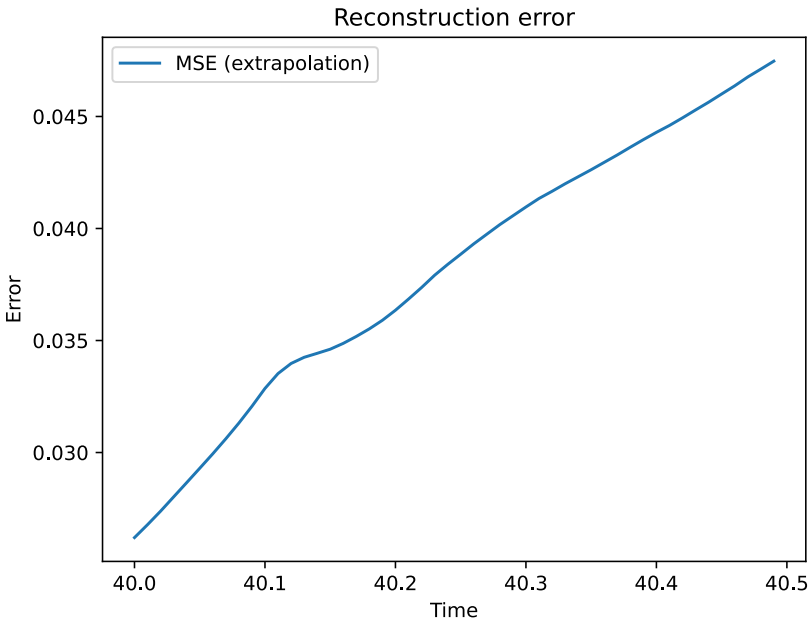

Figure 4.18: MSE of the extrapolation in time, for $\mu = 1.15$. The error show a linear behavior, displaying a global satisfying accuracy.

4.2. Diffusion-advection problem

(a) Low fidelity sample (b) High fidelity sample

Figure 4.19: Samples from the diffusion-advection dataset: (a) and (b) show two frames from the LF and HF data, respectively, at the same time instant t.

We consider a diffusion-advection problem describing a fluid motion in the shallow water limit given by

$$\frac{\partial \omega}{\partial t} + \mu \left(\frac{\partial \psi}{\partial x}\frac{\partial \omega}{\partial y} - \frac{\partial \psi}{\partial y}\frac{\partial \omega}{\partial x} \right) = d\nabla^2 \omega, \tag{4.3a}$$

$$\nabla^2 \psi = \omega \,, \tag{4.3b}$$

defined over a spatial domain $(x, y) \in [-L, L]^2$ and a time span $t \in [0, T]$. Here $\omega(x, y, t)$ and $\psi(x, y, t)$ represent the vorticity and stream function, respectively, $\nabla^2 = \partial x^2 + \partial y^2$ is the two-dimensional Laplacian, and d is the diffusion coefficient. We consider the following initial condition of vorticity:

$$\omega(x, y, 0) = \exp\left(-2x^2 - \frac{y^2}{20} \right), \quad (x, y) \in [-L, L]^2. \tag{4.4}$$

Our goal is to approximate the time-dependent vorticity field ω as the parameter μ varies over $\mathcal{P} = [1, 5]$.

We adopt two fidelity levels that differ in the spacial resolution of discretization and in length of the time window, with $n^{LF} < n^{HF}$ and $T^{LF}_{train} > T^{HF}_{train}$. The system is measured for an additional time window $[T^{HF}_{train}, T^{HF}_{train} + T_{test}]$, for both fidelity levels: the HF testing measurements are therefore unseen by the model until the testing stage.

Moreover, the HF observations span over a smaller set of μ values, with respect to the LF ones, and the model is tested on parameter values μ unseen by the HF sub-model.

Table 4.2 lists the configuration parameters used for generating the dataset. Figure 4.19 shows two frames from the LF and HF datasets, respectively.

Parameters	LF	HF
n	32	100
d	0.001	0.001
μ_{train}	$\{1.5, 2.5, 3.5, 4.5\}$	$\{1.5, 2.5\}$
T_{train}	30	10
L	5	
dt	0.01	
μ_{test}	$\{1.5, 2.5, 3.5\}$	
T_{test}	5	

Table 4.2: List of configuration parameters for the diffusion-advection dataset.

4.2.1. ID and latent variables

Our framework is able to produce an efficient and reliable low-dimensional surrogate of the diffusion-advection system. Indeed, the Levina-Bickel algorithm applied on the LF latent representation estimates $ID = 2$, which is compatible with our theoretical knowledge of problem and allow us to obtain a 2-dimensional latent state space for the HF model.

Figure 4.20 shows the latent variables $\theta_1^{HF}(t)$ and $\theta_2^{HF}(t)$ as functions of time, for each value of $\mu \in \mathcal{P}_{test}$. While it is challenging to interpret their behavior, we can assess their significance from the accuracy of the reconstructions and forward predictions the model produces (reported in the following subsections).

4.2.2. Results for parameter value $\mu = 1.5$

In this subsection we illustrate the effectiveness of the model in reconstructing the frames and predicting forward in time, for the testing parameter value $\mu = 1.5$, $t \in [10, 15]$. While this specific value of the parameter μ is seen by both the portions of the model during the training stage, the evolution of the system beyond $T = 10$ is unknown by the HF sub-model.

Figure 4.21 shows the reconstruction of the frame $\mathbf{x}_t^{HF}$, produced by the SVDKL autoencoder, and the one-step forward prediction of $\mathbf{x}_{t+dt}^{HF}$, generated by the SVDKL dynamical model, with their respective absolute errors. From a qualitative point of view, both the

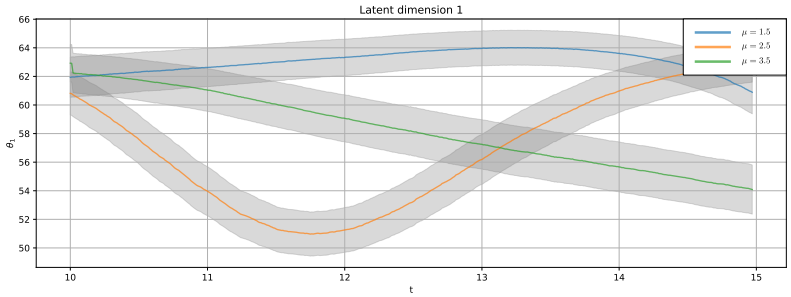

(a) $\theta_1^{HF}(t)$

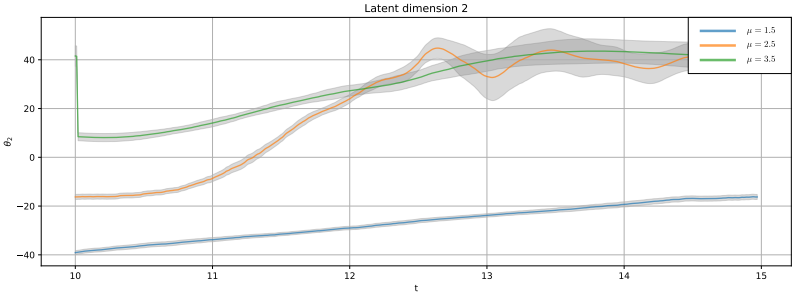

(b) $\theta_2^{HF}(t)$

Figure 4.20: Latent variables of the HF autoencoder during the test time window, for each value of the parameter μ, for the diffusion-advection case. The uncertainty bands are given by $\pm$ two standard deviation in the predictive distribution.

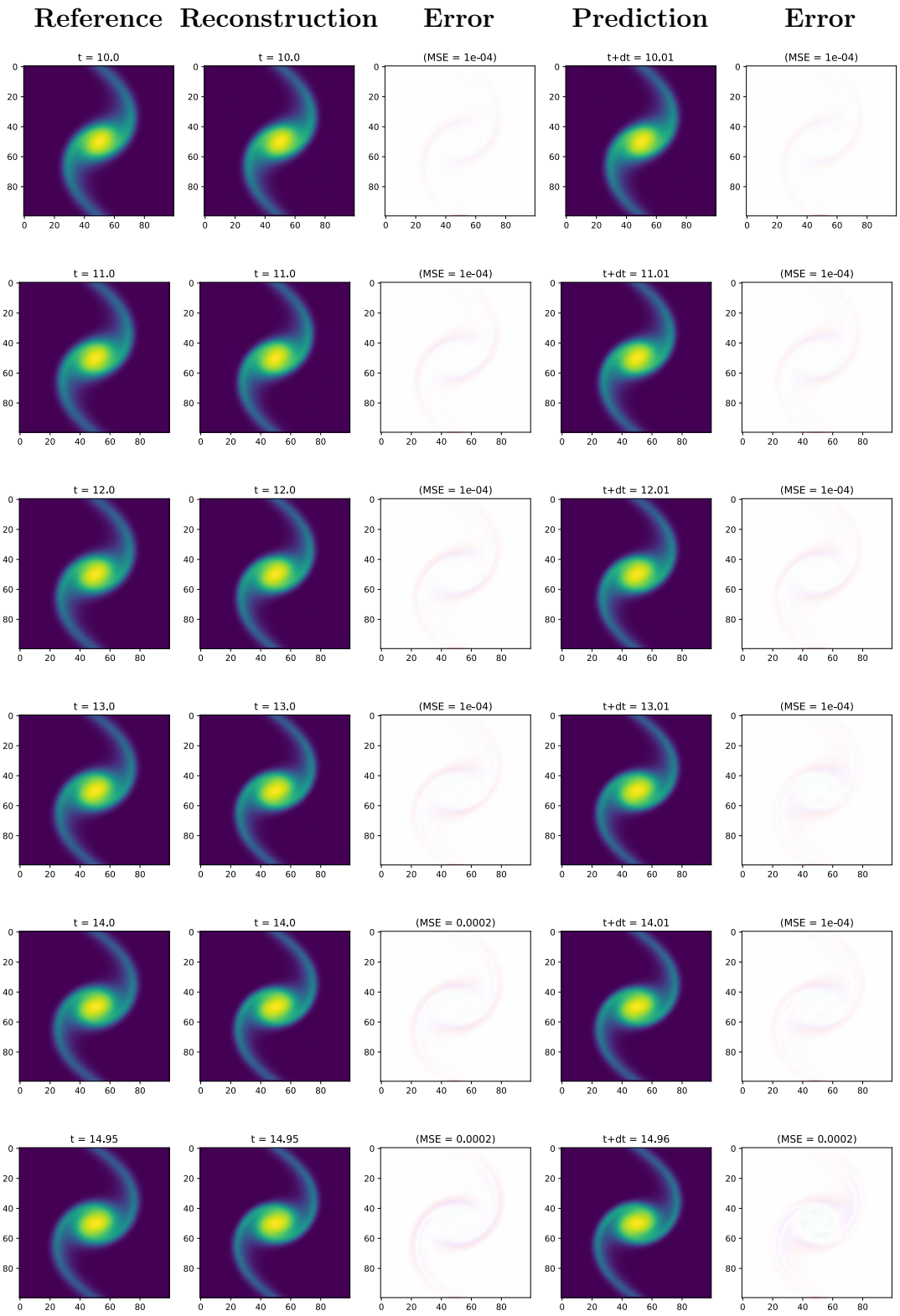

Figure 4.21: Reconstructions and predictions one-step forward in time, with respective absolute errors, for $\mu = 1.5$, for the diffusion-advection case. We notice that the MSE is always very small ($< 1 \cdot 10^{-3}$).

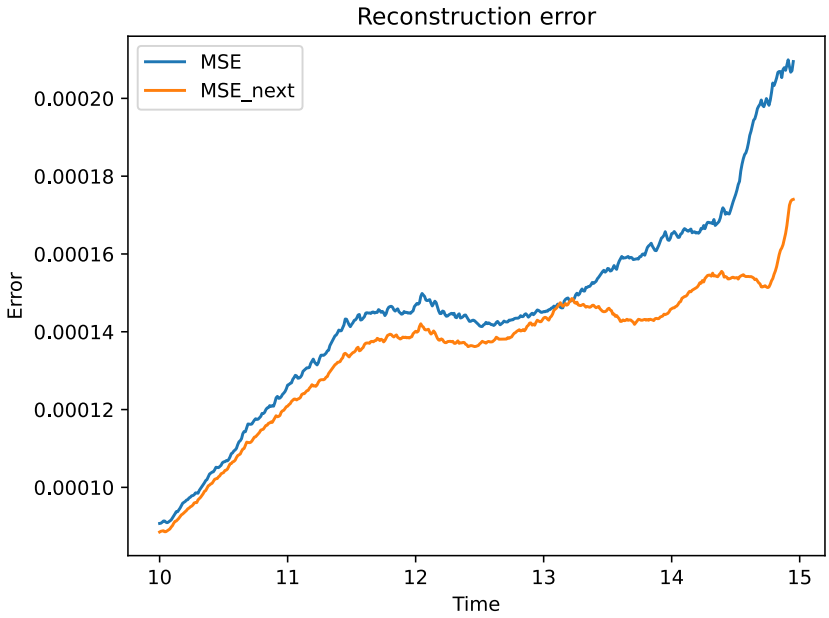

Figure 4.22: MSEs of the reconstruction and forward prediction for $\mu = 1.5$, for the diffusion-advection case, with respect to the relative true measurements, as function of time. The error grows in time, but stays $< 2 \cdot 10^{-4}$.

reconstructions and the predictions are consistently accurate across the entire testing time window. Indeed, the MSE is consistently small, $< 2 \cdot 10^{-4}$, as shown in Figure 4.22, quantitatively corroborating the first visual impression.

If we iterate the one-step forward prediction, by feeding the predicted latent representation to the next iteration, we can extrapolate in time. Figure 4.23 shows some extrapolated frames, starting from the observation at time $t = 10$. Qualitatively speaking, the prediction remains consistent for the entire time window of 2 seconds (200 iterations), while gradually decreasing its accuracy. Figure 4.24 shows the MSE error of the extrapolation with respect to the actual measurements: it increases exponentially for the first few iterations, and then linearly until the end, but still staying below the $5 \cdot 10^{-3}$ threshold.

4.2.3. Results for parameter value $\mu = 2.5$

The following results refer to the testing set for the parameter value $\mu = 2.5$, for $t \in [10, 15]$. Both the LF and HF sub-models were trained on measurements from the system for $\mu = 2.5$, but the latter only until time $t \leq 10$.

Figure 4.25 shows the reconstruction of the frame $\mathbf{x}_t^{HF}$ and the one-step forward prediction of $\mathbf{x}_{t+dt}^{HF}$, with their respective absolute errors. Also in this case, both the reconstruction

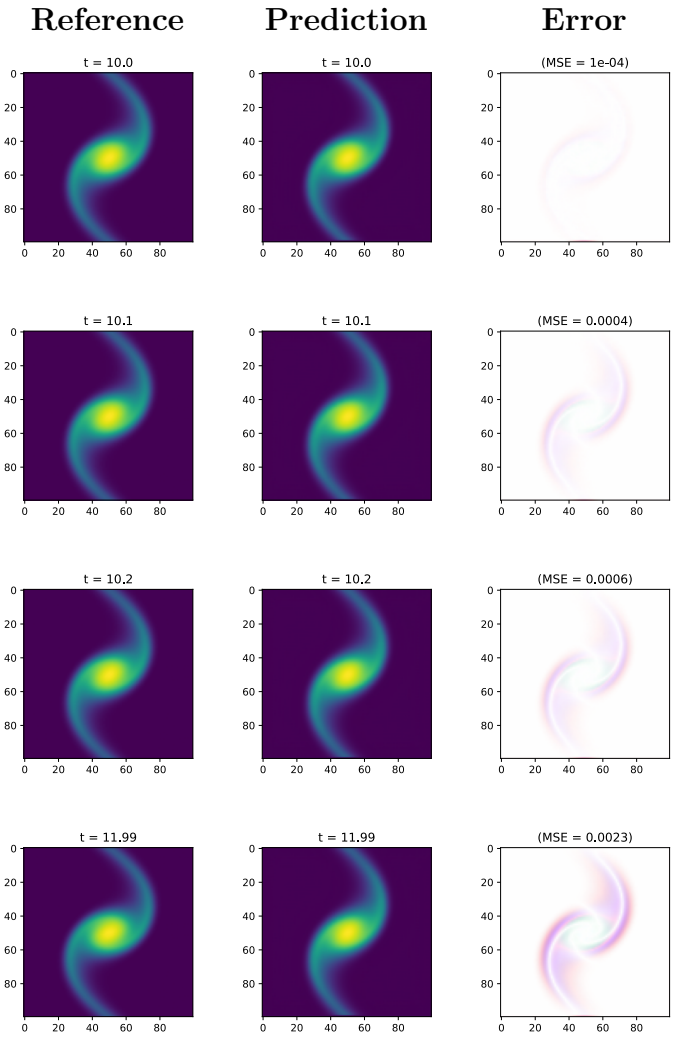

Figure 4.23: Extrapolation in time for $\mu = 1.5$, for the diffusion-advection case, for 200 iterations, with the respective absolute error. The predictions are consistent, while gradually less accurate forward in time.

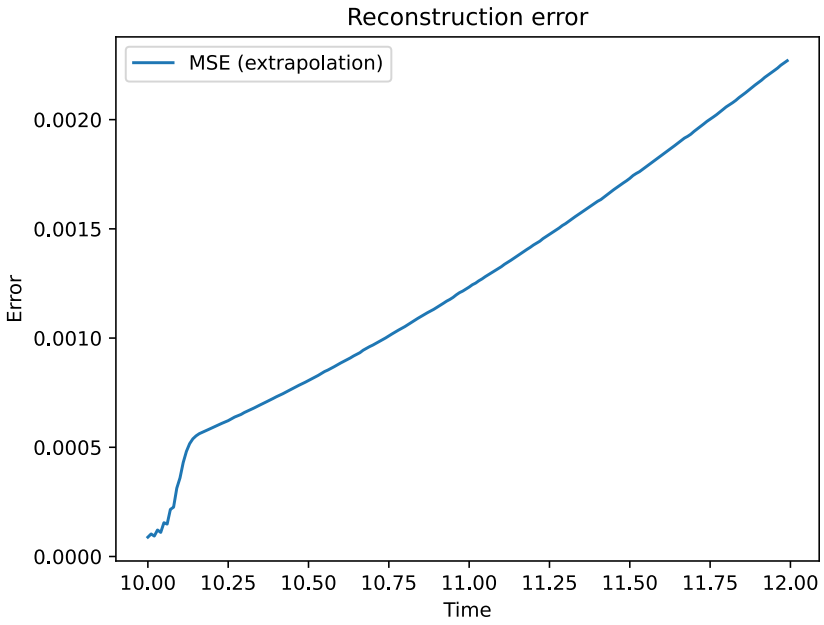

Figure 4.24: MSE of the extrapolation in time, for $\mu = 1.5$, for the diffusion-advection case. It grows exponentially at the beginning, and then linearly until the end, but always $< 5 \cdot 10^{-3}$.

and the one-step prediction remain consistent across the tested time window. However, we observe a more evident absolute error, from a visual point of view, that grows gradually in time.

Indeed, the MSEs shown in Figure 4.26, both for the reconstruction and the prediction, are relatively small ($< 2 \cdot 10^{-3}$) for the first second of observation, only to rapidly increase for $t \in [12, 13]$.

However, the model still seems capable of capturing the evolution of the system with reasonable accuracy, with the $MSE < 1 \cdot 10^{-2}, \forall t \in [10, 15]$.

The extrapolation in time shows equally satisfactory results, with predictions visually consistent for all the tested 200 iterations, as we can see in Figure 4.27. Indeed, the MSE with respect to the actual measurements (Figure 4.28) grows exponentially for the first quarter of a second, and then shows a slower linear behavior, while still keeping around the $5 \cdot 10^{-3}$ threshold.

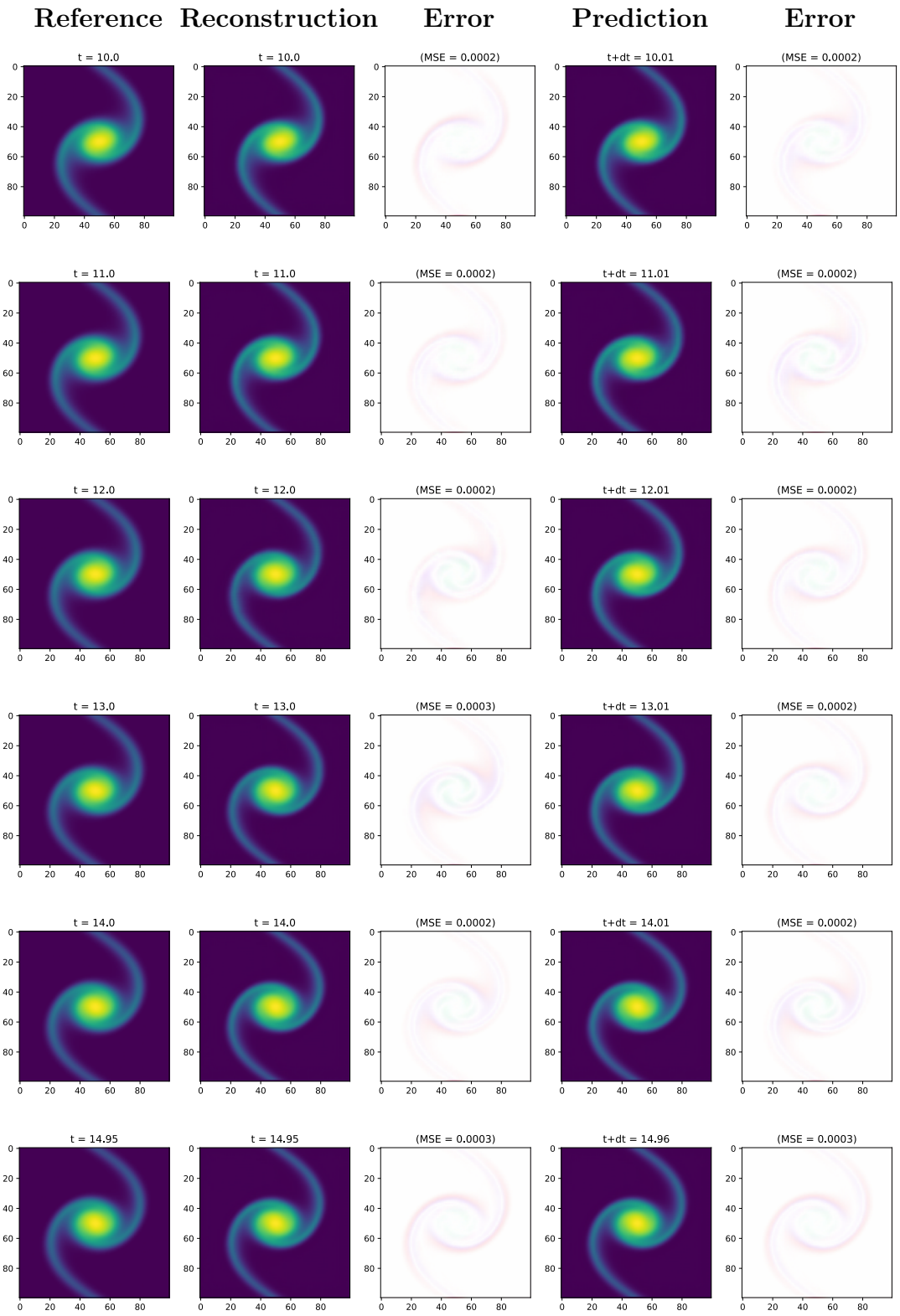

Figure 4.25: Reconstructions and predictions one-step forward in time, for the diffusion-advection case, with respective absolute errors, for $\mu = 2.5$. They are consistent over time, but the error grows gradually.

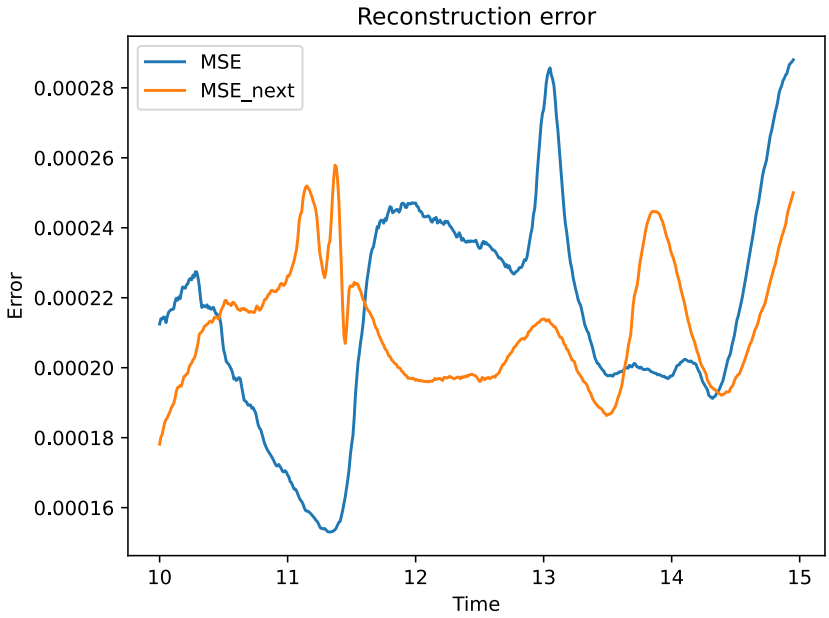

Figure 4.26: MSEs of the reconstruction and forward prediction for $\mu = 2.5$, for the diffusion-advection case, with respect to the relative true measurements, as function of time. It is stable for the first second, only to rapidly increase around $t \in [12, 13]$.

4.2.4. Results for parameter value $\mu = 3.5$

The last test case we present is for the parameter value $\mu = 3.5$, for $t \in [10, 15]$. Now, the HF sub-model has no specific knowledge on this configuration of the PDE system, since it was not trained for this specific value of the parameter μ, not even on the time window $[0, 10]$. On the other hand, the LF training test includes observations for $\mu = 3.5$, for $t \in [0, 30]$.

Figure 4.29 shows the reconstructed frame $\hat{\mathbf{x}}_t^{HF}$ and the one-step forward prediction of $\mathbf{x}_{t+dt}^{HF}$, with their respective absolute errors, for a number of iterations. We observe a general consistence of the predictions with respect to the actual behavior of the system. However, the plots of the absolute errors show a stable but significant discrepancy with respect to the actual measurements.

The plot of the MSEs in Figure 4.30 shows a decreasing behavior, that suggests that possibly the system has almost completed its evolution, and therefore it is easier to predict. Quantitatively, the MSE for both reconstruction and forward prediction assumes value around $1 \cdot 10^{-2}$, which is significant but still acceptable considering that we are extrapolating over the parameter space.

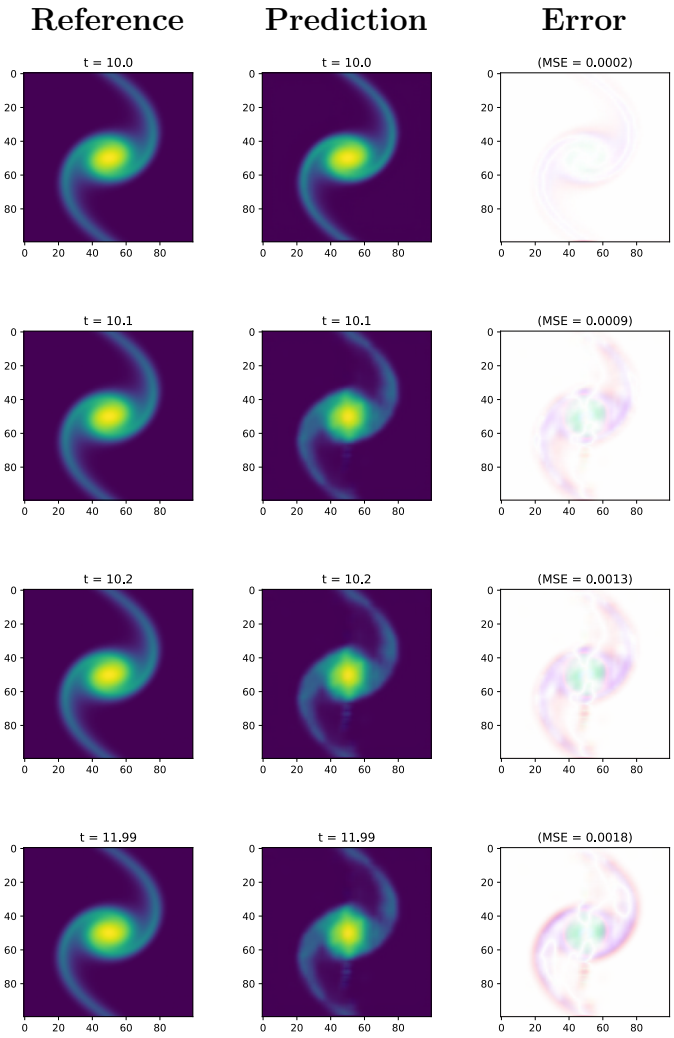

Figure 4.27: Extrapolation in time for $\mu = 2.5$, for 200 iterations, for the diffusion-advection case, with the respective absolute error. The predictions are always visually consistent, but the absolute error gradually grows in time.

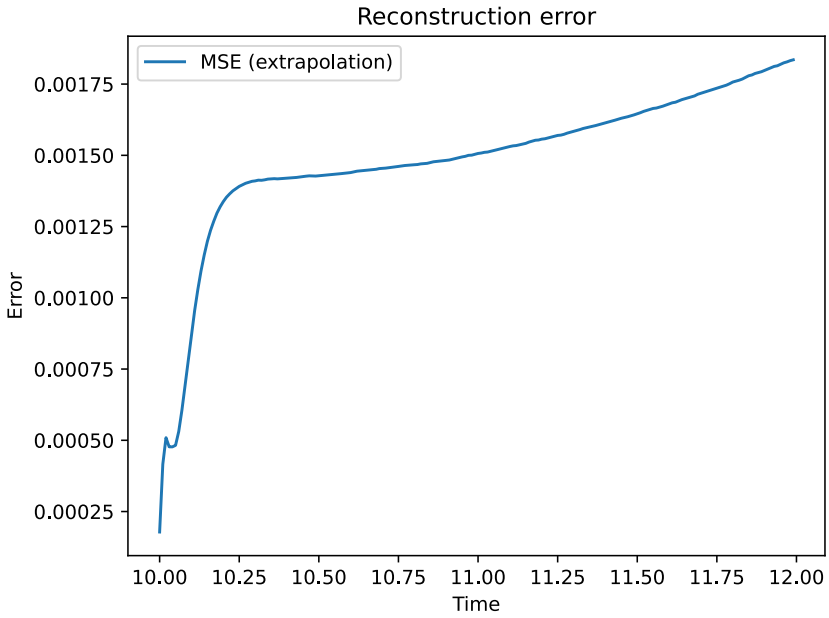

Figure 4.28: MSE of the extrapolation in time, for $\mu = 2.5$, for the diffusion-advection case. It increases exponentially at the beginning, and then it shows a linear behavior.

If we extrapolate also over time, the forward predictions degrade after a number of iterations, as shows in Figure 4.31, with the model predicting a mean state of the system to minimize the error. This behavior suggests that the model has not learned the full dynamics of the system, but it is still able to produce a moderately meaningful prediction.

Figure 4.32 shows the MSE relative to the extrapolation, which decreases in time also in this case. The first rapid descent may be associated to the gradual departure of the model from trying to extrapolate the actual evolution to preferring the "safer" mean state of the system, resulting in the slightly blurred frames in 4.31.

Overall, the model seems capable to learn the evolution of the diffusion-advection system, showing a remarkable accuracy also when extrapolating in time and over the parameter space.

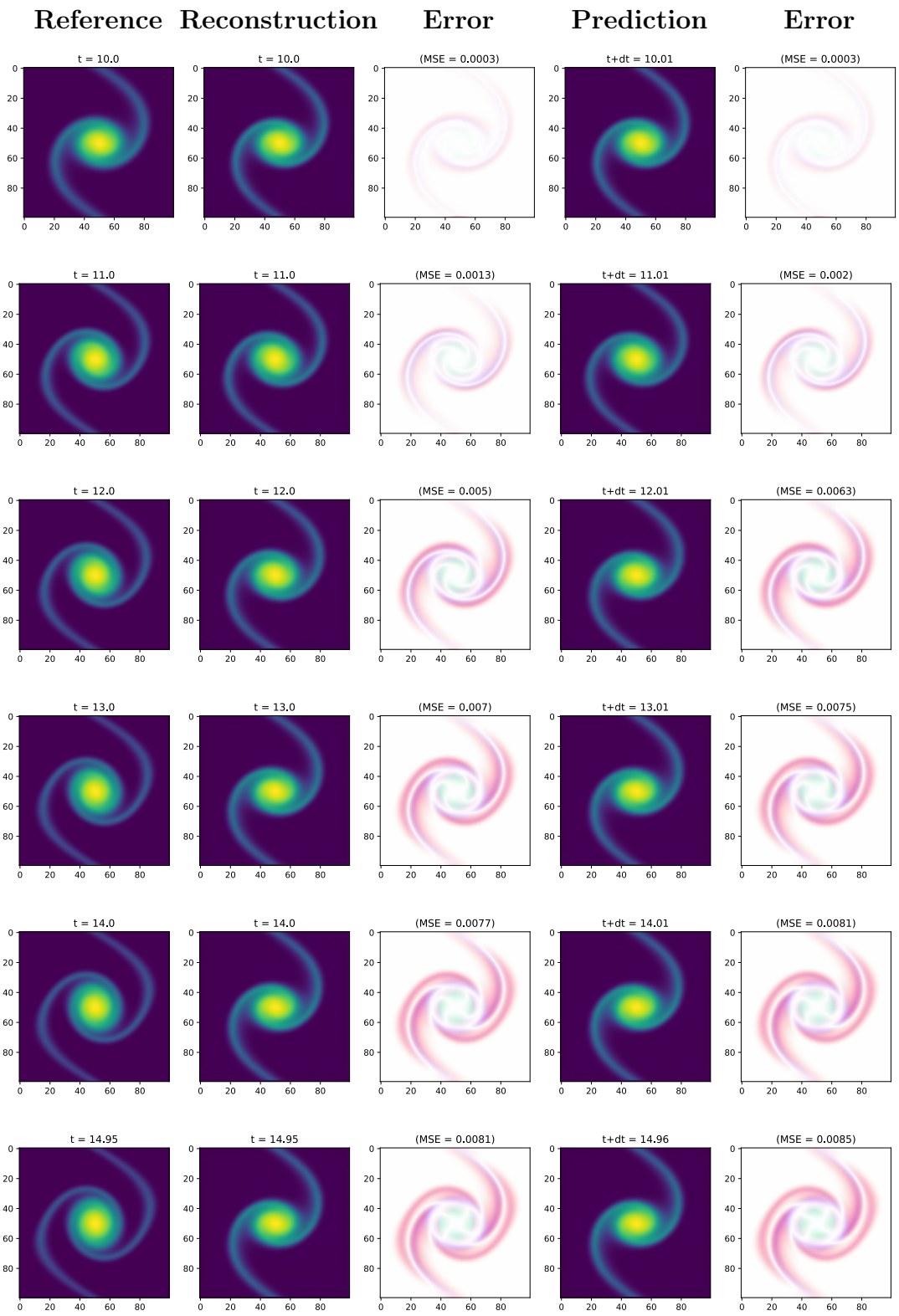

Figure 4.29: Reconstructions and predictions one-step forward in time, with respective absolute errors, for $\mu = 3.5$, for the diffusion-advection case. Both reconstructions and predictions seem visually consistent with the evolution of the system, but the error is significant.

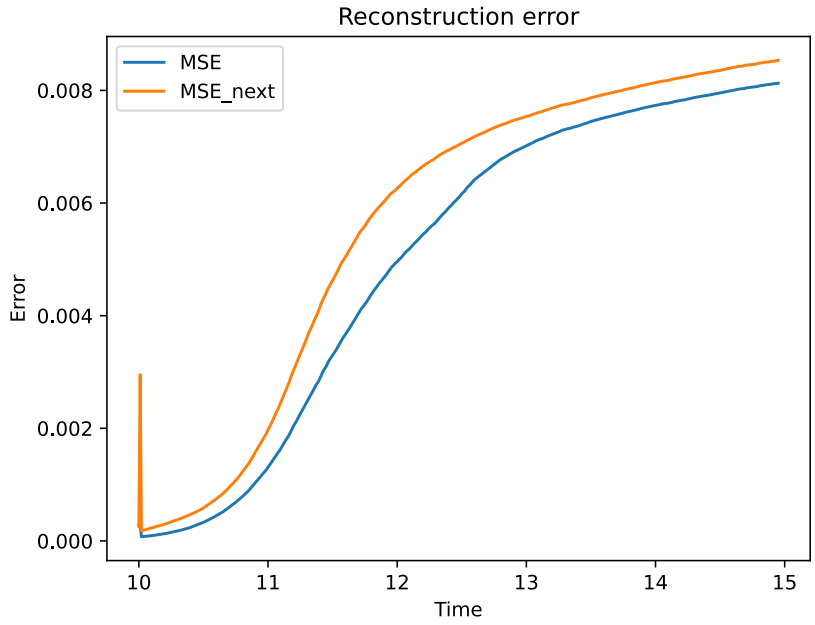

Figure 4.30: MSEs of the reconstruction and forward prediction for $\mu = 3.5$, for the diffusion-advection case, with respect to the relative true measurements, as function of time. Curiously, the MSEs decrease in time, possibly because the system has almost completed its evolution and it is easier to predict.

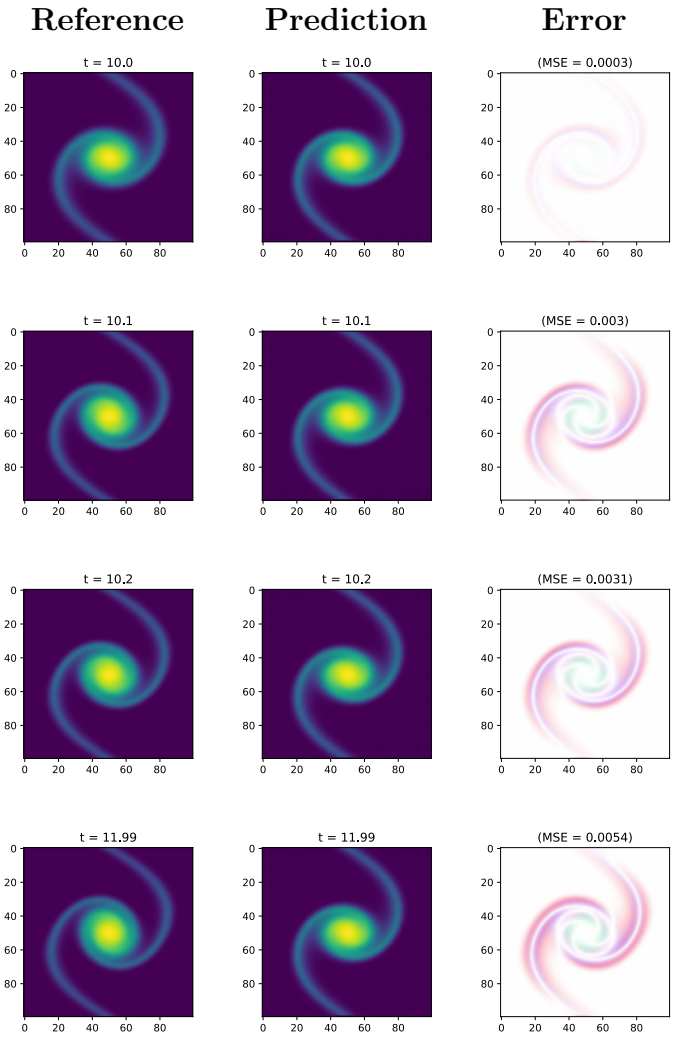

Figure 4.31: Extrapolation in time for $\mu = 3.5$, for the diffusion-advection case, for 200 iterations, with the respective absolute error. Visually, the extrapolated predictions degrade after a few iterations.

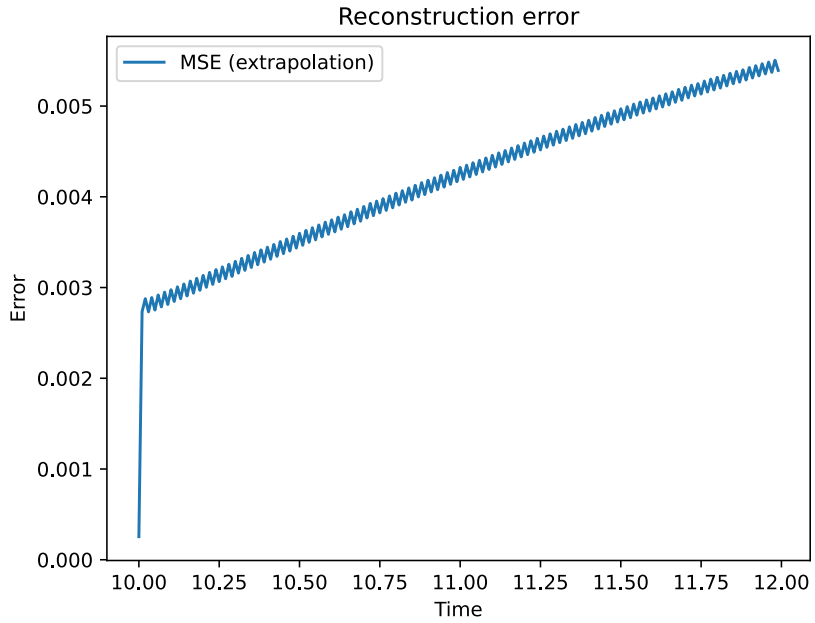

Figure 4.32: MSE of the extrapolation in time, for $\mu = 3.5$, for the diffusion-advection case. The MSE decreases over time, possibly suggesting a regression towards the mean to retain a moderate accuracy.

4.3. Some considerations

When considering data from PDEs, our model proves to be remarkably effective. The results presented in this chapter exhibit notable consistence and accuracy both when reconstructing the frame and predicting the dynamics one-step forward in time, highlighting the efficiency of both the comprehensive architecture and the Levina-Bickel estimator. The efficiency of the model is also highlighted by the significantly low uncertainty exhibited when predicting the latent state.

At the cost of some foreseeable and minor defects where the gradient is larger, our framework still performs reasonably well when extrapolating over the parameter space. In general, the MSEs is bounded within acceptable values.

The more challenging task of extrapolation in time is also tackled with distinctive results, especially considering how efficient the dimensionality reduction proves to be.

Being a completely unsupervised data-driven approach, the model requires large datasets, that for this class of problems translates in a small step of time discretisation. The more evident consequence is that two successive frames often show only a slight evolution, possibly alleviating part of the challenge of the inference on the dynamics. Moreover, the training stage is computationally taxing and it required a few days to complete with the HPC hardware at our disposal.

From a qualitative standpoint, the MF framework allows to consider a smaller HF dataset, generated through a numerical solver for the PDE problem that is computationally expensive. Indeed, we consider around an order of magnitude less observations than in the work [9], for the reaction-diffusion test case. Moreover, the MF framework enables a few added benefits: the model can automatically learn and directly implement the ID estimate, and LF data aids the extrapolation over the parameter space, when specific detailed HF simulations are not available.

Quantitatively speaking, Table 4.3 collects the mean in time of the MSEs in the reaction-diffusion test case, for both reconstruction and forward prediction, comparing the results of our MF model with a SF model that considers only LF data. We can notice an improvement in accuracy for all the tested values of the parameter μ, with the exception of the case $\mu = 1.15$, for which we extrapolate over the parameter space.

In conclusion, the proposed framework proves very effective at learning the unknown state and dynamics of PDE systems, exhibiting notable levels of accuracy for all the tested configurations.

Episode	Reconstruction $\overline{\mathrm{MSE}}(t)$		Forward prediction $\overline{\mathrm{MSE}}(t)$	
	MF	**SF**	**MF**	**SF**
$\mu = 0.5$	$1.0436 \cdot 10^{-2}$	$1.8990 \cdot 10^{-2}$	$1.0396 \cdot 10^{-2}$	$1.8747 \cdot 10^{-2}$
$\mu = 1.0$	$2.1082 \cdot 10^{-2}$	$3.2734 \cdot 10^{-2}$	$2.1275 \cdot 10^{-2}$	$3.2628 \cdot 10^{-2}$
$\mu = 0.6$	$0.9110 \cdot 10^{-2}$	$1.9871 \cdot 10^{-2}$	$0.8927 \cdot 10^{-2}$	$1.9587 \cdot 10^{-2}$
$\mu = 1.15$	$5.6527 \cdot 10^{-2}$	$5.3440 \cdot 10^{-2}$	$5.6545 \cdot 10^{-2}$	$5.3560 \cdot 10^{-2}$

Table 4.3: Comparison of the mean in time of the MSEs, in the reaction-diffusion case, for both reconstruction and forward prediction, between the MF model and a SF model that considers only LF data.

5 | Conclusions and future developments

With this work, we proposed a comprehensive framework for unsupervised data-driven discovery of low dimensional dynamical systems. By conjugating the expressive capability and flexibility of SVDKL with MF schemes, the model is able to exploit large datasets of high-dimensional measurements coming from a variety of data sources, exhibiting different degrees of fidelity to the true system.

The model proved to be effective at most of its goals, including dimensionality reduction, uncertainty quantification and latent dynamics learning, showing good capabilities of generating interpretable latent representations of a large class of problems. In particular, the introduction of the Levina-Bickel algorithm in the workflow proposed by Botteghi et al. [4] enables the estimation of an efficient and compact latent state representation, close to the true state space.

Additionally, our framework allows accurate data-driven unsupervised learning from ordinary RGB videos, to the best of our knowledge for the first time in a MF context. Indeed, the results discussed in the previous chapter show that the model is able to effectively replace a considerable amount of HF data with the less expensive counterpart, while maintaining notable accuracy and reducing the overall cost of measurements.

Further developments should consider a wider range of data sources, and leverage both high and low-dimensional measurements to further generalise the supported class of sensing devices and test cases. The model may also consider different time steps of discretisation among the fidelity levels, to exploit a larger group of LF data. Overall, any generalisation of this framework should consider the goal of reducing the training cost and improving the model capability of extrapolating in time. Future studies may further investigate the gain in accuracy of the MF framework, with respect to traditional SF strategies, and take a step forward towards the interpretability of latent variables and a full identification of the system state space.

Bibliography

[1] M. A. Alvarez, L. Rosasco, and N. D. Lawrence. Kernels for Vector-Valued Functions: a Review, Apr. 2012. URL http://arxiv.org/abs/1106.6251. arXiv:1106.6251 [cs, math, stat].

[2] A. C. Antoulas, D. C. Sorensen, and S. Gugercin. A survey of model reduction methods for large-scale systems. In V. Olshevsky, editor, *A survey of model reduction methods for large-scale systems*, volume 280, pages 193–219, Providence, Rhode Island, 2001. American Mathematical Society. ISBN 9780821819210 9780821878705. doi: 10.1090/conm/280/04630. URL http://www.ams.org/conm/280/.

[3] J.-A. M. Assael, N. Wahlström, T. B. Schön, and M. P. Deisenroth. Data-Efficient Learning of Feedback Policies from Image Pixels using Deep Dynamical Models, Oct. 2015. URL http://arxiv.org/abs/1510.02173. arXiv:1510.02173 [cs, stat].

[4] N. Botteghi, M. Guo, and C. Brune. Deep Kernel Learning of Dynamical Models from High-Dimensional Noisy Data. *Scientific Reports*, 12(1):21530, Dec. 2022. ISSN 2045-2322. doi: 10.1038/s41598-022-25362-4. URL http://arxiv.org/abs/2208.12975. arXiv:2208.12975 [cs, stat].

[5] S. L. Brunton and J. N. Kutz. *Data-Driven Science and Engineering: Machine Learning, Dynamical Systems, and Control*. Cambridge University Press, Cambridge, 2019. doi: 10.1017/9781108380690. URL https://www.cambridge.org/core/books/datadriven-science-and-engineering/77D52B171B60A496EAFE4DB662ADC36E.

[6] S. L. Brunton, J. L. Proctor, and J. N. Kutz. Discovering governing equations from data by sparse identification of nonlinear dynamical systems. *Proceedings of the National Academy of Sciences*, 113(15):3932–3937, Apr. 2016. ISSN 0027-8424, 1091-6490. doi: 10.1073/pnas.1517384113. URL https://pnas.org/doi/full/10.1073/pnas.1517384113.

[7] T. Bui-Thanh, K. Willcox, and O. Ghattas. Parametric Reduced-Order Models for Probabilistic Analysis of Unsteady Aerodynamic Applications. *AIAA Journal*, 46

(10):2520–2529, Oct. 2008. ISSN 0001-1452, 1533-385X. doi: 10.2514/1.35850. URL https://arc.aiaa.org/doi/10.2514/1.35850.

[8] K. Champion, B. Lusch, J. N. Kutz, and S. L. Brunton. Data-driven discovery of coordinates and governing equations. *Proceedings of the National Academy of Sciences*, 116(45):22445–22451, Nov. 2019. ISSN 0027-8424, 1091-6490. doi: 10.1073/pnas.1906995116. URL https://pnas.org/doi/full/10.1073/pnas.1906995116.

[9] B. Chen, K. Huang, S. Raghupathi, I. Chandratreya, Q. Du, and H. Lipson. Discovering State Variables Hidden in Experimental Data, Dec. 2021. URL http://arxiv.org/abs/2112.10755. arXiv:2112.10755 [physics].

[10] P. Conti, M. Guo, A. Manzoni, A. Frangi, S. L. Brunton, and J. N. Kutz. Multi-fidelity reduced-order surrogate modeling, Sept. 2023. URL http://arxiv.org/abs/2309.00325. arXiv:2309.00325 [cs, math].

[11] A. Doerr, C. Daniel, M. Schiegg, N.-T. Duy, S. Schaal, M. Toussaint, and T. Sebastian. Probabilistic Recurrent State-Space Models. In *Proceedings of the 35th International Conference on Machine Learning*, pages 1280–1289. PMLR, July 2018. URL https://proceedings.mlr.press/v80/doerr18a.html.

[12] M. Frangos, Y. Marzouk, K. Willcox, and B. van Bloemen Waanders. Surrogate and reduced-order modeling: a comparison of approaches for large-scale statistical inverse problems [Chapter 7]. *Prof. Willcox via Barbara Williams*, Jan. 2010. URL https://dspace.mit.edu/handle/1721.1/105500.

[13] I. Goodfellow, Y. Bengio, and A. Courville. *Deep Learning*. MIT Press, 2016. http://www.deeplearningbook.org.

[14] GPyTorch Developers. *GPyTorch Documentation*, 2024. URL https://docs.gpytorch.ai/en/stable/. Accessed: 2024-06-19.

[15] M. Guo and J. S. Hesthaven. Data-driven reduced order modeling for time-dependent problems. *Computer Methods in Applied Mechanics and Engineering*, 345:75–99, Mar. 2019. ISSN 0045-7825. doi: 10.1016/j.cma.2018.10.029. URL https://www.sciencedirect.com/science/article/pii/S0045782518305334.

[16] M. Guo, A. Manzoni, M. Amendt, P. Conti, and J. S. Hesthaven. Multi-fidelity regression using artificial neural networks: efficient approximation of parameter-dependent output quantities. *Computer Methods in Applied Mechanics and Engineering*, 389:114378, Feb. 2022. ISSN 00457825. doi: 10.1016/j.cma.2021.114378. URL http://arxiv.org/abs/2102.13403. arXiv:2102.13403 [cs, math].

[17] Gymnasium Developers. *Gymnasium Documentation*, 2024. URL `https://gymnasium.farama.org`. Accessed: 2024-06-24.

[18] Imageio Developers. *Imageio Documentation*, 2024. URL `https://imageio.readthedocs.io/en/stable/`. Accessed: 2024-06-22.

[19] A. G. Journel. *Fundamentals of Geostatistics in Five Lessons*, volume 8 of *Short Courses in Geology*. American Geophysical Union (AGU), 1989.

[20] M. Kast, M. Guo, and J. S. Hesthaven. A non-intrusive multifidelity method for the reduced order modeling of nonlinear problems. *Computational Methods in Applied Mechanics and Engineering*, 364, 2020.

[21] M. C. Kennedy and A. O'Hagan. Predicting the Output from a Complex Computer Code When Fast Approximations Are Available. *Biometrika*, 87(1):1–13, 2000. ISSN 0006-3444. URL `https://www.jstor.org/stable/2673557`.

[22] D. P. Kingma and M. Welling. Auto-Encoding Variational Bayes, Dec. 2022. URL `http://arxiv.org/abs/1312.6114`. arXiv:1312.6114 [cs, stat].

[23] I. Kononenko. Bayesian neural networks. *Biological Cybernetics*, 61(5):361–370, Sept. 1989. ISSN 0340-1200, 1432-0770. doi: 10.1007/BF00200801. URL `http://link.springer.com/10.1007/BF00200801`.

[24] F. Lancellotti. Multi-fidelity deep kernel learning, 2024. URL `https://github.com/federico-lancellotti/multi-fidelity-deep-kernel-learning`. Accessed: 2024-06-17.

[25] K. Lee and K. Carlberg. Model reduction of dynamical systems on nonlinear manifolds using deep convolutional autoencoders, June 2019. URL `http://arxiv.org/abs/1812.08373`. arXiv:1812.08373 [cs].

[26] E. Levina and P. Bickel. Maximum Likelihood Estimation of Intrinsic Dimension. In *Advances in Neural Information Processing Systems*, volume 17. MIT Press, 2004. URL `https://papers.nips.cc/paper_files/paper/2004/hash/74934548253bcab8490ebd74afed7031-Abstract.html`.

[27] A. Manzoni. *Computational Statistics class notes*. 2023.

[28] Matplotlib Developers. *Matplotlib Documentation*, 2024. URL `https://matplotlib.org`. Accessed: 2024-06-22.

[29] R. M. Murray and J. Hauser. A case study in approximate linearization: The ac-

robot example. Memorandum UCB/ERL M91/28, University of California, Berkeley, Electronics Research Laboratory, April 1991.

[30] F. Negri, G. Rozza, A. Manzoni, and A. Quarteroni. Reduced Basis Method for Parametrized Elliptic Optimal Control Problems. *SIAM Journal on Scientific Computing*, 35(5):A2316–A2340, Jan. 2013. ISSN 1064-8275, 1095-7197. doi: 10.1137/120894737. URL `http://epubs.siam.org/doi/10.1137/120894737`.

[31] NumPy Developers. *NumPy Documentation*, 2024. URL `https://numpy.org/doc/stable/index.html`. Accessed: 2024-06-20.

[32] S. W. Ober, C. E. Rasmussen, and M. van der Wilk. The Promises and Pitfalls of Deep Kernel Learning, July 2021. URL `http://arxiv.org/abs/2102.12108`. arXiv:2102.12108 [cs, stat].

[33] B. Peherstorfer, K. Willcox, and M. Gunzburger. Survey of multifidelity methods in uncertainty propagation, inference, and optimization. *SIAM Review*, 60(3):550–591, 2018.

[34] J. L. Proctor, S. L. Brunton, and J. N. Kutz. Dynamic Mode Decomposition with Control. *SIAM Journal on Applied Dynamical Systems*, 15(1):142–161, Jan. 2016. ISSN 1536-0040. doi: 10.1137/15M1013857. URL `http://epubs.siam.org/doi/10.1137/15M1013857`.

[35] Python Software Foundation. *ABC - Abstract Base Classes*, 2024. URL `https://docs.python.org/3/library/abc.html`. Accessed: 2024-06-19.

[36] Python Software Foundation. *pickle — Python object serialization*, 2024. URL `https://docs.python.org/3/library/pickle.html`. Accessed: 2024-06-20.

[37] PyTorch Developers. *PyTorch Documentation*, 2024. URL `https://pytorch.org/docs/stable/index.html`. Accessed: 2024-06-19.

[38] A. Quarteroni and G. Rozza, editors. *Reduced Order Methods for Modeling and Computational Reduction*. Springer International Publishing, Cham, 2014. ISBN 9783319020891 9783319020907. doi: 10.1007/978-3-319-02090-7. URL `http://link.springer.com/10.1007/978-3-319-02090-7`.

[39] A. Quarteroni, A. Manzoni, and F. Negri. *Reduced Basis Methods for Partial Differential Equations*, volume 92 of *UNITEXT*. Springer International Publishing, Cham, 2016. ISBN 9783319154305 9783319154312. doi: 10.1007/978-3-319-15431-2. URL `http://link.springer.com/10.1007/978-3-319-15431-2`.

[40] M. Raissi, P. Perdikaris, and G. E. Karniadakis. Inferring solutions of differential equations using noisy multi-fidelity data. *Journal of Computational Physics*, 335: 736–746, 2017.

[41] C. E. Rasmussen and C. K. I. Williams. *Gaussian Processes for Machine Learning*. The MIT Press, 2005. ISBN 9780262256834. doi: 10.7551/mitpress/3206.001.0001. URL https://direct.mit.edu/books/book/2320/gaussian-processes-for-machine-learning.

[42] P. J. Schmid. Dynamic mode decomposition of numerical and experimental data. *Journal of Fluid Mechanics*, 656:5–28, Aug. 2010. ISSN 1469-7645, 0022-1120. doi: 10.1017/S0022112010001217. URL https://www.cambridge.org/core/journals/journal-of-fluid-mechanics/article/abs/dynamic-mode-decomposition-of-numerical-and-experimental-data/AA4C763B525515AD4521A6CC5E10DBD4.

[43] SciPy Developers. *SciPy Documentation*, 2024. URL https://docs.scipy.org/doc/scipy/. Accessed: 2024-06-19.

[44] C. Sinigaglia, D. E. Quadrelli, A. Manzoni, and F. Braghin. Fast active thermal cloaking through PDE-constrained optimization and reduced-order modeling. *Proceedings of the Royal Society A: Mathematical, Physical and Engineering Sciences*, 478(2258): 20210813, Feb. 2022. ISSN 1364-5021, 1471-2946. doi: 10.1098/rspa.2021.0813. URL http://arxiv.org/abs/2110.10845. arXiv:2110.10845 [math].

[45] R. Tedrake. *Underactuated Robotics*. 2023. URL https://underactuated.csail.mit.edu.

[46] N. Wahlström, T. B. Schön, and M. P. Deisenroth. From Pixels to Torques: Policy Learning with Deep Dynamical Models, June 2015. URL http://arxiv.org/abs/1502.02251. arXiv:1502.02251 [cs, stat].

[47] A. G. Wilson, Z. Hu, R. Salakhutdinov, and E. P. Xing. Deep Kernel Learning. In *Proceedings of the 19th International Conference on Artificial Intelligence and Statistics*, pages 370–378. PMLR, May 2016. URL https://proceedings.mlr.press/v51/wilson16.html.

[48] A. G. Wilson, Z. Hu, R. Salakhutdinov, and E. P. Xing. Stochastic Variational Deep Kernel Learning, Nov. 2016. URL http://arxiv.org/abs/1611.00336. arXiv:1611.00336 [cs, stat].

A | Implementation details

In this chapter, we introduce the Python implementation of the MF DKL model. This module extends the code provided by Botteghi et al. in [4] to the MF framework, considering additional test cases and introducing a new user interface.

The module is composed of three main parts, each thought to be accessed through a dedicated Python script:

1. the dataset generating part, to produce the data for the training and testing of the model;
2. the training of the model, to fit the model exploiting a dedicated training dataset;
3. the testing of the model, to test the goodness of fit of the trained model and produce some reconstructions from the dedicated testing dataset.

Warning: this implementation, and in particular the training section, is computationally intensive. The use of a GPU is recommended.

The code can be accessed through GitHub [24].

A.1. Folder structure

The Git repository contains the following files and folders:

- `README.md`, with complete instructions on how to run the code;
- `config.yaml`, to set the test case environment, the hyperparameters of the model and some test related settings;
- `generate_dataset.py`, to produce the train and test data, according to the specified test case;
- `main-gym.py`, `main-pde.py`, to initialize and train the model on the generated train dataset;

- `test-gym.py`, `test-pde.py`, `test_utils.py`, to load the weights and test the model on the test dataset, producing some plots and reconstructions;
- `requirements.txt`, that lists the required libraries to run the module;
- `/src` (folder), containing the implementation of the Python module;
- `/Data` (folder), to store the train and test datasets;
- `/Results` (folder), to store the weights of the trained model and the plots produced during the testing phase.

A.2. Generate the dataset

The `GenerateDataset` class provides an interface to produce the training and testing datasets, at multiple levels of fidelity and considering the desired test case. A separate pickle file containing pairs of consecutive RGB frames is produced for each dataset and it is stored in the `/Data/env_name/` folder. The user can set the test case through the `env_name` parameter in the `config.yaml` file; two major dataset environments are available: Gym and PDE.

Gym The Gym environment leverages on the Gymnasium library to produce one of the following datasets: Pendulum, Acrobot, MountainCarContinuous. A number of independent episodes are simulated, with the dynamical system evolving from random initial conditions. The episodes are produced in a nested fashion, with some available at all the fidelity levels and some only at lower fidelities: LF datasets are larger but less accurate.

PDE The PDE environment solves either the reaction-diffusion or the diffusion-advection problem, producing pairs of consecutive RGB frames representing the solution matrix at times t and $t + 1$ plotted as heatmaps. For LF datasets, the solution is observed over a longer timeframe, but on a coarser mesh, and possibly on a larger set of parameters.

A.2.1. GenerateDataset

The `GenerateDataset` class is implemented as an abstract class [35], with `GenerateGym` and `GeneratePDE` inheriting from it and implementing the abstract method `generate_dataset()`. The parameters can be read from the `config.yaml` file and passed to the `GenerateDataset` object as the `args` dictionary argument.

GenerateGym

The `GenerateGym` class allows to produce a dataset from one of the available environments of the Gymnasium library [17]: Pendulum, Acrobot and MountainCarContinuous.

The following parameters can be set in the `config.yaml` file:

- `num_episodes`: a dictionary with the number of training episodes for each level of fidelity (an episodes consists of 200 frames, 500 frames and 400 frames, respectively, for the three aforementioned test cases);
- `num_episodes_test`: a dictionary with the number of testing episodes for each level of fidelity;
- `crop`: a list of dictionaries, each associated with a fidelity level and containing:
  - `portion`: the portion of the image to retain (from 0 to 1, 0: none, 1: the entire image);
  - `pos`: the quadrant to crop (1, 2, 3 or 4);
- `occlusion`: a list of dictionaries, each associated with a fidelity level and containing:
  - `portion`: the portion of the image to cover (from 0 to 1, 0: none, 1: the entire image);
  - `pos`: the quadrant to cover (1, 2, 3 or 4);
- `obs_dim_1`: a dictionary with the length of the images, for each fidelity level;
- `obs_dim_2`: a dictionary with the height of the images, for each fidelity level.

The method `generate_dataset()` runs episodes in the chosen Gymnasium environment, adopting random initials conditions and the null action, and it produces a pickle file for each fidelity level, containing a list of dictionaries with keys:

- `obs`: a stack of the observations at times $t-1$ and t, as RGB images;
- `next_obs`: a stack of the observations at times t and $t+1$, as RGB images;
- `terminated`: whether the episode is terminated;
- `state`: the state of the system at time t;
- `next_state`: the state of the system at time $t+1$.

It leverages on a number of auxiliary private methods, namely, `_new_obs()` to stack to consecutive frames and optionally add occlusion or crop the image, `_log_obs()` to build

the dictionary with two consecutive observations and auxiliary data, `_save_log()` to save the dataset as a pickle file. The Gymnasium environment is initialized by the method `_set_environment()`, called inside the constructor. Optionally, it is possible to save the dataset as png images by passing the argument `png=True` and leveraging on the method `_save_png()`

GeneratePDE

The GeneratePDE class produces a dataset from either the reaction-diffusion or the diffusion-advection problem.

The following parameters can be set in the `config.yaml` file:

- `d`: a dictionary with the diffusion coefficient for each fidelity level;
- `mu`: a dictionary of lists, each containing the reaction or transport coefficients to use in the training set for each fidelity level;
- `mu_test`: a dictionary of lists, each containing the reaction or transport coefficients to use in the training set for each fidelity level;
- `T`: a dictionary with the training time horizon for each fidelity level;
- `T_test`: the time horizon for testing;
- `dt`: the time step;
- `n`: a dictionary with the number of grid points for each fidelity level.

Once the PDE problem is chosen, the method `generate_dataset` employs a dedicated solver from the class `PDESolver` to solve the equation at each level of fidelity and for each parameter `mu`. Since the testing set chronologically follows the training set, we consider the complete time horizon `T[level] + T_test` when solving the equation.

Solutions related to different values of mu but to the same fidelity level are stacked. Once computed, they are logged leveraging on the auxiliary private methods `_log_level()` and `_log_obs()`. Finally they are saved as pickle files containing a list of dictionaries with keys:

- `obs`: a stack of the observations at times t and $t+1$, as RGB images;
- `next_obs`: a stack of the observations at times $t+1$ and $t+2$, as RGB images;
- `t`: the time t;
- `terminated`: whether the episode is terminated.

In this case, the RGB images are heatmaps of the numerical solution.

A.2.2. PDESolver

The abstract class `PDESolver` has two implemented child classes: `ReactionDiffusionSolver` and `DiffusionAdvectionSolver`.

ReactionDiffusionSolver

The `ReactionDiffusionSolver` class solves the lambda-omega reaction-diffusion system governed by the following equations

$$\dot{u} = \left(1 - \left(u^2 + v^2\right)\right) u + \mu \left(u^2 + v^2\right) v + d \left(u_{xx} + u_{yy}\right), \tag{A.1}$$

$$\dot{v} = -\mu \left(u^2 + v^2\right) u + \left(1 - \left(u^2 + v^2\right)\right) v + d \left(v_{xx} + v_{yy}\right) \tag{A.2}$$

defined over a spatial domain $(x, y) \in [-L, L]^2$ and a time span $t \in [0, T]$, where μ and d are the reaction and diffusion parameters, respectively. The initial condition is defined as

$$u(x, y, 0) = v(x, y, 0) = \tanh\left(\sqrt{x^2 + y^2} \cos\left((x + iy) - \sqrt{x^2 + y^2}\right)\right). \tag{A.3}$$

The class leverages on the `solve_ivp()` function from the SciPy library [43], using the explicit Runge-Kutta method of order 5 to solve the system, and the `fft2()` and `ifft2()` functions to compute the laplacians. The parameters n and dt define the number of grid points for the spatial mesh and the time step for the evaluation in time of the evolution of the system. The method `_rhs()` computes the discretized right hand side of the equation.

DiffusionAdvectionSolver

The `DiffusionAdvectionSolver` class solves an advection-diffusion problem describing a fluid motion in the shallow water limit given by

$$\frac{\partial \omega}{\partial t} + \mu \left(\frac{\partial \psi}{\partial x}\frac{\partial \omega}{\partial y} - \frac{\partial \psi}{\partial y}\frac{\partial \omega}{\partial x}\right) = d\nabla^2 \omega, \tag{A.4}$$

$$\nabla^2 \psi = \omega, \tag{A.5}$$

defined over a spatial domain $(x, y) \in [-L, L]^2$ and a time span $t \in [0, T]$. Here $\omega(x, y, t)$ and $\psi(x, y, t)$ represent the vorticity and stream function, respectively, $\nabla^2 = \partial x^2 + \partial y^2$ is

the two-dimensional Laplacian, and we consider the following initial condition of vorticity:

$$\omega(x, y, 0) = \exp\left(-2x^2 - \frac{y^2}{20}\right), \quad (x, y) \in [-L, L]^2. \tag{A.6}$$

The class leverages on the Numpy [31] functions `fft2()` and `ifft2()` for the gradient and the laplacian, and on the SciPy [43] function `odeint()` to solve the system. The parameters n and dt define the number of grid points for the spatial mesh and the time step for the evaluation in time of the evolution of the system. The method `_rhs()` computes the discretized right hand side of the equation.

A.2.3. Logger

The `Logger` class logs the generated data and saves it to a pickle [36] file. In particular, the filename and the logging directory are defined inside the constructor, while the method `obslog()` appends the new observation and the method `save_obslog()` saves the logged data to a file.

A.2.4. utils

`save_pickle()` This function saves the input data as a pickle file, with filename as defined by the passed parameter.

`stack_frames()` This function stacks two frames together along the channel dimension and performs optional cropping and occlusion.

`crop_frame()` This function crops a frame based on the specified portion and position. The portion is a float taking values in $[0, 1]$ (if `portion=1`, the entire frame is retained), while the position is the number of the quadrant to consider (1: top-right, 2: top-left, 3: bottom-left, 4: bottom-right), cropping from the relative vertex of the original image.

`add_occlusion()` This function adds a black occlusion to the frame, of size defined by the portion $\in [0, 1]$ parameter (if `portion=1`, the entire frame is occluded). The occlusion is generated from the center of the image towards one of the four vertices, relative to the desired quadrant position (1: top-right, 2: top-left, 3: bottom-left, 4: bottom-right).

`len_of_episode()` This function returns the length of an episode in number of frames, for each of the supported Gym test cases. In particular, 200 for the Pendulum, 500 for the Acrobot, 400 for the MountainCarContinuous.

`heatmap_to_image()` This function converts a matrix into its heatmap, returned as RGB image.

A.3. Train the model

The training of the model is performed for each fidelity level sequentially. Each stage is composed of the construction of the l-th sub-model, its training and, possibly, the estimation of the intrinsic dimension. The class `BuildModel` handles each of these steps and an example of its usage can be found in the `main-gym.py` and `main-pde.py` scripts.

Some configuration parameters and model hyperparameters can be set in the `config.yaml` file and passed to the `BuildModel` object as the `args` dictionary argument.

A.3.1. `BuildModel`

The `BuildModel` class initializes, trains and tests the model. Its constructor accepts the following arguments:

- `args`: a dictionary with the parameters read from the `config.yaml` file;
- `use_gpu`: a bool to set whether to use the GPU;
- `test`: a bool to set the model in testing mode and select the correct input dataset;
- `flush`: a bool to optionally flush the print statements.

The following parameters can be set in the `config.yaml` file:

- `seed`: the seed, to make the results reproducible;
- `batch_size`: the size of the batch during the training;
- `max_epoch`: the maximum number of epochs for the training;
- `rho`: the weight of the LF term;
- `training`: whether to activate the training;
- `lr`, `lr_gp`, `lr_gp_lik`, `lr_gp_var`: the learning rates;
- `reg_coef`: the weight decay coefficient for the Adam optimizer;
- `k1`, `k2`: the weights of the loss function;
- `grid_size`: the grid size for the variational strategy;

- `obs_dim_1`, `obs_dim_2`, `obs_dim_3`: the dimension of each observation (typically $84 \times 84 \times 6$);
- `h_dim`: the hidden dimension size;
- `env_name`: the name of the testing case (as defined when the dataset is generated);
- `training_dataset`: the name of the data files;
- `log_interval`: the frequency of saving the partially trained model weights;
- `jitter`: the jitter value to compensate for possible numerical instabilities.

The `BuildModel` constructor also handles the instantiation of the correct DataLoader object, according to the defined testing case.

add_level()

The `add_level()` method initializes the l-th sub-model, instantiating the likelihood for both the stochastic variational DKL autoencoder and the dynamical model, as GPyTorch [14] `MultitaskGaussianLikelihood`, and the sub-model itself.

train_level()

The `train_level()` method trains the previously initialized sub-model passed as argument. In particular, it initializes the variational losses for both parts of the sub-model, as `VariationaKL` defined in `variational_inference.py`, and the optimizers. For the non variational parameters, the PyTorch [37] Adam optimizer is adopted, while the Stochastic Gradient Descent optimizer is used for the variational parameters. Schedulers to reduce the learning rate are implemented after half and three quarters of the epochs.

The training part leverages on the train function implemented in the `trainer.py` file, run for a defined number of epochs, and it is performed with the GPyTorch `cholesky_jitter` setting to cure possible numerical instabilities. The weights of the model are saved in a dedicated `.pth` file.

get_latent_representations()

This method evaluates the trained sub-model and returns the latent representation computed from the training dataset. The evaluation is performed in chunks, to avoid memory saturation when the dataset is large, and the dimension of each chunk can be set as argument of the method. The latent representations `z` (of the observation at time t), `z_next` (of the observation at time $t+1$) and `z_fwd` (the one-step forward prediction) are

returned.

eval_level()

This methods evaluates the trained sub-model and return both the latent representations `z`, `z_next`, `z_fwd` and the relative reconstructions `mu` and `mu_fwd`. The evaluation is performed on the data imported when the object is instantiated (training set if `test=False`, testing set if `test=True`), therefore it is recommended to use this method only on small datasets to avoid memory saturation.

A.3.2. DataLoader

The `DataLoader` is implemented as one parent `BaseDataLoader` class and two specialized classes, `GymDataLoader` and `PDEDataLoader`. Their role is to load and manipulate the dataset, including sampling batches for the training.

The common attributes, such as the observations and the latent representations, are handled by the parent classes, from which `GymDataLoader` and `PDEDataLoader` inherit and complete the methods addressing the specifics of the test case they aim to cover.

The constructor reads the data passed as argument, converting it to a PyTorch Tensor and normalizing it. Three additional methods are implemented:

- `sample_batch()`: to randomly sample a batch of desired size;
- `sample_batch_with_idx()`: to sample a batch from a given list of indices;
- `get_all_samples()`: to get all the samples (useful when evaluating the model).

The batches are returned as dictionaries with keys: `obs`, `next_obs`, `z_LF`, `z_next_LF`, `z_fwd_LF`. Both `obs` and `next_obs` are composed of two RGB images concatenated along the color channel. The child class `GymDataLoader` returns also the states of the system at time t and $t+1$ as keys `state` and `next_state`; the child class `PDEDataLoader` returns also the current time instant t as key `t`.

A.3.3. trainer

The `train()` function loops over a number of random batches: at each iteration, the gradients are initialized, a forward pass of the model is performed and the loss components are updated. Once the loss is computed, the gradients are backward propagated and the parameters are updated.

Since the autoencoder and the forward model are jointly trained, the gradients of the dynamical model flow through the autoencoder as well.

A.3.4. `models`

The final model is implemented by the `SVDKL_AE_latent_dyn()` class, contained inside the `models.py` file, along with the various layers it is composed of. The implementation is an expansion of the model used in [4] that supports the multi-fidelity case, accepting as argument also the low-fidelity latent representations of the input observations. The latent space dimension is either 20, for the sub-model 0, or ID, for the following sub-models, as estimated from the previously learnt $(l-1)$-th latent representation.

`SVDKL_AE_latent_dyn` As introduced in the previous chapter, this model is composed of two main layers: a stochastic variational deep kernel learning autoencoder and a forward dynamical deep kernel learning model. The forward pass evaluates the SVDKL AE on both the current and the next observation, and the forward model on the latent representation of the current observation. Finally, the forward latent representation is decoded to an image reconstruction, later used by the loss function.

Two additional methods are implemented to predict the dynamics and the mean dynamics of the system. In particular, the forward model is evaluated and the output forward latent representation is decoded to an image reconstruction.

`SVDKL_AE` The stochastic variational deep kernel learning autoencoder is composed of an encoder, a decoder and a gaussian process layer. The forward pass encodes the input and corrects the resulting latent representation with the corresponding low fidelity one. The features are then passed through the gaussian process layer, which produces a predictive latent state distribution $p(\mathbf{z}_t|\mathbf{x}_t)$. Finally, the latent state vector $\mathbf{z}_t$ is sampled and decoded.

`Encoder` The encoder is composed of four convolutional layers, with 32 filters per layer. The convolutional filters are of size (3×3) and shifted across the images with stride 1. Batch normalization is also used after the 2nd and 4th convolutional layers. The output features of the last convolutional layer are flattened and fed to two final fully connected layers. Each layer has ELU activations, except the last fully-connected layer with a linear activation.

`Decoder` The decoder is composed of a linear fully-connected layer and four transpose convolutional layers with 32 filters each. The convolutional filters are of size (3×3) and shifted across the images with stride 1. Batch normalization is used after the 2nd and 4th convolutional layers, and ELU activations are employed for all the layers except the last one.

`GaussianProcessLayer` The gaussian process layer class inherits from the GPyTorch [14] `ApproximateGP` to implement a GP with constant mean and ARD-SE kernel, which produces a latent state distribution $p(\mathbf{z}_t|\mathbf{x}_t, \mathbf{z}_t^{LF})$. The class leverages on the GPyTorch `GridInterpolationVariationalStrategy`, with the Cholesky variational distribution implemented by the same library.

`Forward_DKLModel` The forward deep kernel learning dynamical model is composed of a neural network and a gaussian process layer. Analogously to the SVDKL encoder, the output features of the neural network are fed to independent GPs to produce a next state distribution $p(\mathbf{z}_{t+1}|\mathbf{z}_t, \mathbf{z}_{t+1}^{LF})$. Again, we sample the next latent states $\mathbf{z}_{t+1}$.

`ForwardModel` The forward model is a traditional neural network composed of 3 fully-connected layers of size 512, 512, and ID (or 20, for the lowest fidelity level), respectively, with ELU activations except the final layer with a linear activation.

`losses`

The binary cross entropy and the Kullback-Leibler divergence are implemented as components of the loss function, exploited during the training stage, leveraging on the PyTorch [37] functionals and distributions. The BCE is used to compute the loss between an input and a target tensor, in particular between the observation at time t and its reconstruction, to train the autoencoder, and between the next observation and the decoded forward prediction, to train the dynamical model. The KL divergence is used to compute the loss between two distributions, in particular between the likelihood from the autoencoder trained on the next observation and the likelihood of the dynamical model, to train the latter. We employ the KL balancing, for balancing how much the prior is pulled towards the posterior and vice versa. The implementation is basically the same as the original code in [4].

variational_inference

As variational terms of the loss, for both the autoencoder and the dynamical model, we use the `VariationalKL` class implemented in `variational_inference.py`, inherited from the original code by Botteghi et al. in [4]. These two terms are initialized by the `BuildModel` class and updated by the train function during the training stage.

The `VariationalKL` class inherits from the `_ApproximateMarginalLogLikelihood` class, which expands the GPyTorch [14] `MarginalLogLikelihood` class by approximating the marginal log-likelihood. In particular, it gets the KL divergence from the model and return the difference between that and the prior.

intrinsic_dimension

A function `eval_id()` to estimate the intrinsic dimension of a dataset is implemented in the `intrinsic_dimension.py` file. It leverages on the Levina-Bickel method, separately implemented in the `Levina_Bickel()` function, along with the k-nearest neighbors algorithm. The function `estimate_ID()` computes the rounded mean of the three estimates of ID from $\mathbf{z}$, $\mathbf{z}_{next}$ and $\mathbf{z}_{fwd}$.

A.3.5. utils

`load_pickle()` This function loads the input data from a pickle file, with filename as defined by the passed parameter.

`align_pde()` This function computes indices to align in time two PDE datasets of different levels of fidelity. Indeed, we usually assume that the LF simulations are run for a longer time, but the relative latent representations used to train the HF model should be aligned with the HF data.

`check_indices()` This function checks with an assert if the indices passed as argument are inside the bounds of the input tensor.

A.4. Test the model

Once the model is trained, we can test it on an unseen dataset to measure its accuracy in reconstructing and predicting the dynamics of the model. A typical workflow involves instantiating the model as a `BuildModel` object, passing the argument `test=True`, and reconstructing its levels as done during the training stage. The methods `add_level()`,

`test_level()` and `eval_level()` are used in this case.

In a typical setup, we would want to evaluate the level of highest fidelity; to do so, we should use its image reconstructions and the respective LF latent representations, outputs of the previous sub-model(s).

The scripts `test-gym.py` and `test-pde.py` provide a possible workflow to test the results, on the Gym and PDE cases respectively. In particular, it plots the latent variables as functions of time, using the function `plot_latent_dims()`, and the reconstructions at times t and $t+1$ (by the autoencoder and the forward model, respectively), with the relative MSE with respect to the true measurement. A gif is also generated, to better show the evolution in time of the system and the behavior of the model. This testing stage leverages on the Matplotlib library [28] for the plots and exploits the `predict_dynamics_mean()` of the model to compute the forward reconstructions.

By iterating on this method, it is possible to extrapolate in time in an autoregressive fashion, and study the predictive capabilities of the model further away from the seen measurements.

The scripts `test-gym.py` and `test-pde.py` store the results inside the same directory of the trained weights, in a `/plots` subfolder. The following parameters can be set in the `config.yaml` file and passed as `args` to the `BuildModel` object, in addition to the same used for training:

- `testing_dataset`: the name of the data files;
- `results_folder`: the path where to save the model weights;
- `weights_filename`: the name of the file where to store the model weights.

Moreover, the testing script makes use of both the initial latent space dimension and the ID estimate, which should be stored during the training stage and loaded in the testing stage.

A.4.1. `BuildModel`

`test_level()` This method loads both the (testing) dataset and the trained weights of the sub-model. If the LF latent representations are not passed as arguments, dummy ones are defined instead. Finally, the data loader is instantiated. Both the data loader and the sub-model are returned, ready to be evaluated with the `eval_level()` method. This method assumes an already instantiated sub-model, using the `add_level()` method.

A.4.2. utils

`plot_frame()` This function plots a given frame of the dataset, optionally displaying to the screen and/or storing as a `.png` file. The plots are generated using the Matplotlib library [28].

`plot_latent_dims()` This function receives as input the latent representations of the dataset as a matrix $N \times D$, where N is the number of samples and D is the number of dimensions. The first `dims` dimensions are plotted as functions of time, with a curve for each episode. The length of the episodes and how many to be plotted are specified as arguments. The plots are generated using the Matplotlib library [28]. The function can optionally display the plots to screen and/or save them as `.png` images.

`get_length()` This function return the length of a variable. In particular, it returns 1 if the variable is an int or a float; if the variable is a list, it returns its length.

`generate_gif()` This function loads a number of `.png` images from a given local path and renders them as a `.gif` file, using the Imageio library [18]. The function assumes that the images have progressive integers as filenames.

`plot_error()` This function plots the errors, passed as list, as functions of time, and saves the plot as `.png` image to the desired filepath.